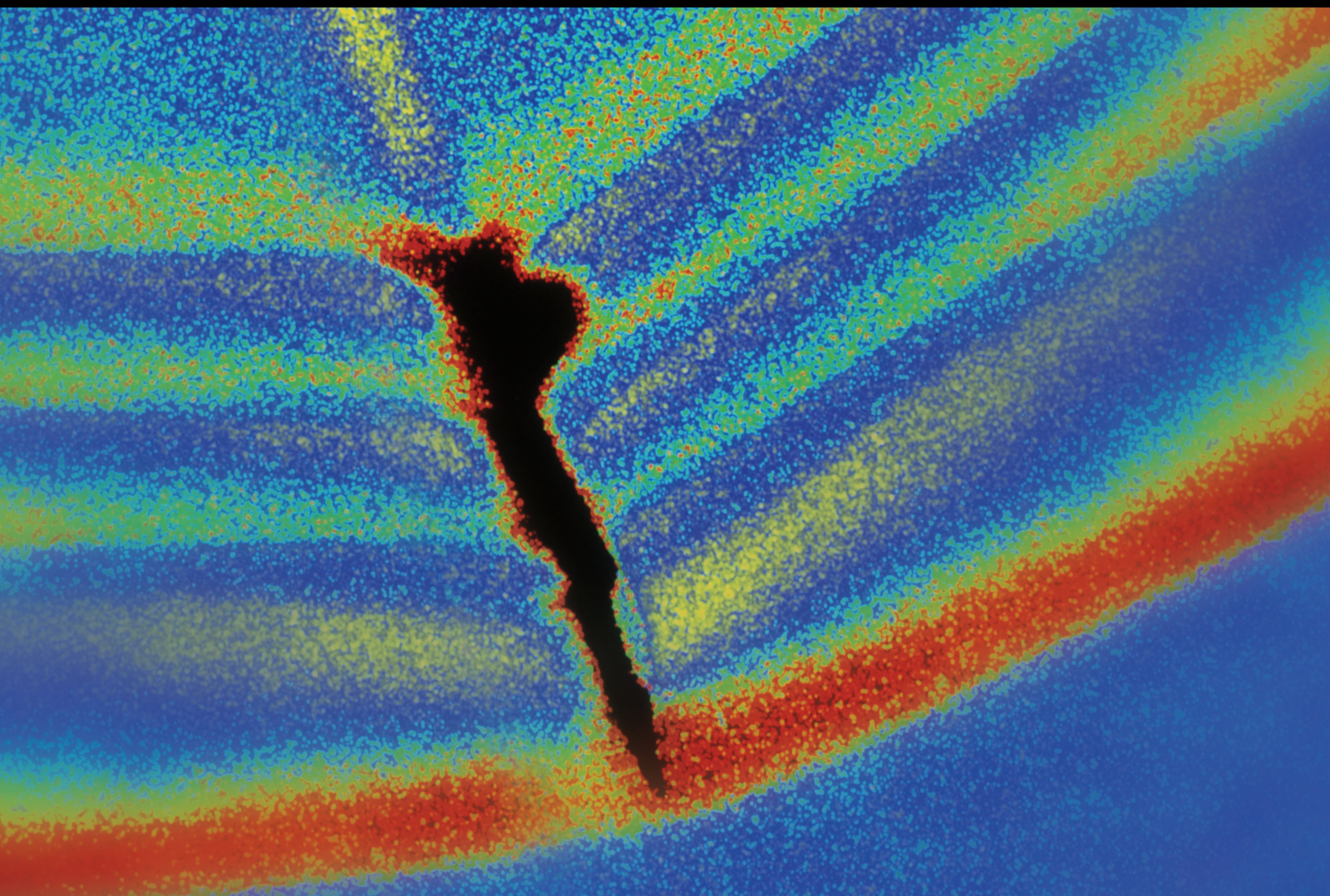


Energy Dissipation Systems for Seismic Vibration-Induced Damage Mitigation in Building Structures: Development, Modeling, Analysis, and Design

Lead Guest Editor: Giada Gasparini

Guest Editors: Michele Palermo, Felice Ponzio, Stefano Sorace, and Oren Lavan





**Energy Dissipation Systems for Seismic
Vibration-Induced Damage Mitigation
in Building Structures: Development, Modeling,
Analysis, and Design**

Shock and Vibration

**Energy Dissipation Systems for Seismic
Vibration-Induced Damage Mitigation
in Building Structures: Development, Modeling,
Analysis, and Design**

Lead Guest Editor: Giada Gasparini

Guest Editors: Michele Palermo, Felice Ponzo, Stefano Sorace,
and Oren Lavan



Copyright © 2018 Hindawi. All rights reserved.

This is a special issue published in "Shock and Vibration." All articles are open access articles distributed under the Creative Commons Attribution License, which permits unrestricted use, distribution, and reproduction in any medium, provided the original work is properly cited.

Editorial Board

- Brij N. Agrawal, USA
Felix Albu, Romania
Marco Alfano, Italy
Sumeet S. Aphale, UK
Hassan Askari, Canada
Lutz Auersch, Germany
Matteo Aureli, USA
Mahmoud Bayat, Iran
Marco Belloli, Italy
Giosuè Boscato, Italy
Francesco Braghin, Italy
Rafał Burdzik, Poland
Salvatore Caddemi, Italy
Ivo Caliò, Italy
Antonio Carcaterra, Italy
Dumitru I. Caruntu, USA
Cristina Castejón, Spain
Nicola Caterino, Italy
Gabriele Cazzulani, Italy
Noel Challamel, France
Athanasios Chasalevris, UK
Xavier Chimentin, France
Nawawi Chouw, New Zealand
Simone Cinquemani, Italy
Pedro A. Costa, Portugal
Giorgio Dalpiaz, Italy
Farhang Daneshmand, Canada
Sergio De Rosa, Italy
Silvio L.T. de Souza, Brazil
Dario Di Maio, UK
Luigi Di Sarno, Italy
Longjun Dong, China
Lorenzo Dozio, Italy
Mohamed El Badaoui, France
Mohammad Elahinia, USA
Fiorenzo A. Fazzolari, UK
Matteo Filippi, Italy
Paola Forte, Italy
Francesco Franco, Italy
Juan C. G. Prada, Spain
Pedro Galvín, Spain
Gianluca Gatti, Italy
- Marco Gherlone, Italy
Anindya Ghoshal, USA
Nere Gil-Negrete, Spain
Itzhak Green, USA
Hassan Haddadpour, Iran
M.I. Herreros, Spain
Hamid Hosseini, Japan
Reza Jazar, Australia
Sakdirat Kaewunruen, UK
Yuri S. Karinski, Israel
Jeong-Hoi Koo, USA
Georges Kouroussis, Belgium
Mickaël Lallart, France
Luca Landi, Italy
Marco Lepidi, Italy
Manuel Lopez Aenlle, Spain
Nuno M. Maia, Portugal
Giuseppe Carlo Marano, Italy
Stefano Marchesiello, Italy
Francesco S. Marulo, Italy
Jean-Mathieu Mencik, France
Laurent Mevel, France
Fabio Minghini, Italy
Rui Moreirs, Portugal
Emiliano Mucchi, Italy
Sara Muggiasca, Italy
Tony Murmu, UK
Pedro Museros, Spain
Roberto Nascimbene, Italy
Sundararajan Natarajan, India
Toshiaki Natsuki, Japan
Miguel Neves, Portugal
Nicola Nisticò, Italy
Roberto Palma, Spain
A. Papageorgiou, Greece
Francesco Pellicano, Italy
Paolo Pennacchi, Italy
Evgeny Petrov, UK
Giuseppe Piccardo, Italy
Antonina Pirrotta, Italy
Franck Poisson, France
Luca Pugi, Italy
- Mohammad Rafiee, Canada
Carlo Rainieri, Italy
José J. Rangel-Magdaleno, Mexico
Didier Rémond, France
Francesco Ripamonti, Italy
Riccardo Rubini, Italy
Salvatore Russo, Italy
Giuseppe Ruta, Italy
Edoardo Sabbioni, Italy
Filippo Santucci de Magistris, Italy
Onome E. Scott-Emuakpor, USA
Roger Serra, France
Vadim V. Silberschmidt, UK
Kumar V. Singh, USA
Jean-Jacques Sinou, France
Isabelle Sochet, France
Alba Sofi, Italy
Jussi Sopanen, Finland
Stefano Sorace, Italy
Chao Tao, China
Marco Tarabini, Italy
Gloria Terenzi, Italy
Mario Terzo, Italy
Tai Thai, Australia
Marc Thomas, Canada
Hamid Toopchi-Nezhad, Iran
Carlo Trigona, Italy
Federica Tubino, Italy
Nerio Tullini, Italy
Ângelo M. Tusset, Brazil
Jens Twiefel, Germany
Filippo Ubertini, Italy
Marcello Vanali, Italy
F. Viadero, Spain
M. Ahmer Wadee, UK
Jörg Wallaschek, Germany
Matthew J. Whelan, USA
Agnieszka Wylomanska, Poland
Enrico Zappino, Italy
Radoslaw Zimroz, Poland

Contents

Energy Dissipation Systems for Seismic Vibration-Induced Damage Mitigation in Building Structures: Development, Modeling, Analysis, and Design

Giada Gasparini , Michele Palermo , Felice Ponzo , Stefano Sorace , and Oren Lavan

Volume 2018, Article ID 4791641, 2 pages

Experimental Assessment of a Skyhook Semiactive Strategy for Seismic Vibration Control of a Steel Structure

Nicola Caterino , Mariacristina Spizzuoco , Antonio Occhiuzzi , and Antonio Bonati

Volume 2018, Article ID 6460259, 12 pages

Mechanical Performance and Design Method of Improved Lead Shear Damper with Long Stroke

Baoshun Wang, Weiming Yan, and Haoxiang He 

Volume 2018, Article ID 1623103, 18 pages

Adaptive Gain Scheduled Semiactive Vibration Control Using a Neural Network

Kazuhiko Hiramoto , Taichi Matsuoka, and Katsuaki Sunakoda

Volume 2018, Article ID 3762784, 19 pages

Experimental Study on Variation Rules of Damping with Influential Factors of Tuned Liquid Column Damper

Yang Yu, Lixin Xu, and Liang Zhang

Volume 2017, Article ID 6209205, 17 pages

Research on Fluid Viscous Damper Parameters of Cable-Stayed Bridge in Northwest China

Xiongjun He, Yongchao Yang, Xiang Xiao, and Yulin Deng

Volume 2017, Article ID 4532325, 9 pages

Editorial

Energy Dissipation Systems for Seismic Vibration-Induced Damage Mitigation in Building Structures: Development, Modeling, Analysis, and Design

Giada Gasparini ¹, Michele Palermo ¹, Felice Ponzo ²,
Stefano Sorace ³, and Oren Lavan⁴

¹Department of Civil, Chemical, Environmental, and Materials Engineering, School of Engineering and Architecture, University of Bologna, 40110 Bologna, Italy

²School of Engineering, University of Basilicata, Potenza, Italy

³Polytechnic Department of Engineering and Architecture, University of Udine, 33100 Udine, Italy

⁴Faculty of Civil and Environmental Engineering, Technion-Israel Institute of Technology, 32000 Haifa, Israel

Correspondence should be addressed to Giada Gasparini; giada.gasparini4@unibo.it

Received 7 March 2018; Accepted 7 March 2018; Published 10 April 2018

Copyright © 2018 Giada Gasparini et al. This is an open access article distributed under the Creative Commons Attribution License, which permits unrestricted use, distribution, and reproduction in any medium, provided the original work is properly cited.

One of the main challenges in today's civil/earthquake engineering is the effective mitigation and control of damage due to earthquake-induced vibrations, with the aim of safer structures, thus satisfying society expectations. Since the mid XX century, passive, semiactive, and active controlled systems have been proposed, tested, studied, and optimized to mitigate earthquake-induced effects upon structures. Their effectiveness in reducing structural vibrations and damage is nowadays worldwide recognized. Nonetheless, despite the large amount of research effort, the practical implementation of innovative seismic protection devices in building structures is still limited to only few countries (such as USA, Japan, and Italy).

This Special Issue is thus devoted to energy dissipation systems, with particular emphasis to modeling issues, design aspects, numerical simulations, control strategies, and experimental studies.

The works published in this Special Issue introduce to the researchers community some remarkable novelty. The five valuable contributions have been selected to cover all the main themes of the topic, including the studies of various devices such as fluid viscous dampers (X. He et al., China), semiactive control devices (N. Caterino et al., Italy, K. Hiramoto et al., Japan), lead shear dampers (B. Wang et al., China), and tuned liquid column dampers (Y. Yu et al., China).

N. Caterino et al. in “Experimental Assessment of a Skyhook Semiactive Strategy for Seismic Vibration Control of a Steel Structure” investigated the benefits of semiactive (SA) sky hook (SH) dampers for seismic protection of a two-storey steel frame via shaking table tests. The control strategy is particularly effective for reducing the floor acceleration, thus achieving high seismic protection for nonstructural components and contents.

B. Wang et al. in “Mechanical Performance and Design Method of Improved Lead Shear Damper with Long Stroke” present an experimental study on an improved plate lead shear damper with long stroke (ILSD-LS) developed to meet the engineering requirements for high rise structures with long periods subjected to far-field earthquakes. The numerical results indicate that the devices can effectively control the deformation and reduce damage.

K. Hiramoto et al. in “Adaptive Gain Scheduled Semiactive Vibration Control Using a Neural Network” propose an adaptive gain scheduled semiactive control method using an artificial neural network for structural systems subject to earthquake disturbance. The proposed design method is applied to the semiactive control design of a base-isolated building with a semiactive damper. Compared to the passive control case and the conventional semiactive control method based on the clipped optimal control method, the proposed semiactive control method is shown to have better

control performance on vibration suppression and flexibility against earthquake disturbances whose time and frequency characteristics are unknown over the conventional semiactive control approach, aiming at the robust performance characteristics.

X. He et al. in “Research on Fluid Viscous Damper Parameters of Cable-stayed Bridge in Northwest China” investigate the seismic response of an existing bridge located in North West China, by means of numerical simulations. The results indicate that seismic response can be reduced by installing longitudinal nonlinear fluid viscos dampers (FVD) between the towers and the girders. The simulations have been performed to determine the optimal dampers parameters.

Y. Yu et al. in “Experimental Study on Variation Rules of Damping with Influential Factors of Tuned Liquid Column Damper” investigated the response of tuned liquid column damper (TLCD) through experimental tests. TLCD devices are used for the motion suppression of floating platforms. A specific vibration testing system on land was developed to satisfy the requirements of off-shore float platforms with low-frequency and large amplitude. In detail, based on the experimental method of uniform design, a series of experimental tests were conducted to determine the quantitative relationship between the head loss coefficient and other factors.

In summary, this Special Issue provides a snapshot of the up-to-date energy dissipation systems which could represent a valuable reference for both academic and technical readers.

Giada Gasparini
Michele Palermo
Felice Ponzo
Stefano Sorace
Oren Lavan

Research Article

Experimental Assessment of a Skyhook Semiactive Strategy for Seismic Vibration Control of a Steel Structure

Nicola Caterino ^{1,2}, Mariacristina Spizzuoco ³,
Antonio Occhiuzzi ^{1,2} and Antonio Bonati²

¹Department of Engineering, University of Naples “Parthenope”, Naples, Italy

²Construction Technologies Institute (ITC), National Research Council (CNR), San Giuliano Milanese, Milan, Italy

³Department of Structures for Engineering and Architecture, University of Naples Federico II, Naples, Italy

Correspondence should be addressed to Nicola Caterino; nicola.caterino@uniparthenope.it

Received 25 August 2017; Accepted 28 January 2018; Published 22 February 2018

Academic Editor: Giada Gasparini

Copyright © 2018 Nicola Caterino et al. This is an open access article distributed under the Creative Commons Attribution License, which permits unrestricted use, distribution, and reproduction in any medium, provided the original work is properly cited.

Sky-hook damping is one of the most promising techniques for feedback control of structural vibrations. It is based on the idea of connecting the structure to an ideal fixed point of the space through passive dissipative devices. Herein the benefit of semiactive (SA) sky-hook (SH) damping is investigated for seismic protection of a two-storey steel frame via shaking table tests. This kind of SA control is achieved implementing a continuous monitoring of selected structural response parameters and using variable dampers. The damping properties of the latter are changed in real-time so as to make the force provided by the damper match the desired SH damping force as closely as possible. To this aim, two prototype magnetorheological dampers have been installed at the first level of the frame and remotely driven by a SH controller. The effectiveness of the control strategy is measured as response to reduction in terms of floor accelerations and interstory drift in respect to the uncontrolled configuration. Two different calibrations of the SH controller have been tested. The experimental results are deeply discussed in order to identify the optimal one and understand the motivations of its better performance.

1. Introduction

Semiactive (SA) structural control systems rely on smart devices able to provide a rapid variation of their stiffness and/or damping properties. Although the probably first implementation of a SA structural control system is based on variable stiffness devices [1], today most of the research efforts are aimed at the adoption of variable damping schemes. The latter idea was first introduced in the early 1970s by Crosby and Karnopp [2], who showed the possibility of exploiting a variable-constant viscous damper in the context of automotive industry. The original work of Crosby and Karnopp envisioned a SA suspension driven by a two-state switching policy that makes the viscous damper behave pretty much like a sky-hook device. One of the advantages of such idea is the corresponding model-free control algorithm, whose implementation does not require a previous knowledge of the system parameters and/or of the external excitation [3].

Although these control algorithms are widely described in the scientific literature, their effectiveness is almost always shown by numerical applications. Notable exceptions are cited in the following. Li and Xu [4] performed shaking table tests on a three-storey one-bay frame model, controlled by a double-ended shear mode combined with valve mode MR fluid device placed between the ground and the first floor. The validity of the SA control system was verified by implementing three different control algorithms: the instantaneous optimal control algorithm, the classical linear optimal control algorithm, and the linear-quadratic Gaussian control algorithm. Lee et al. [5] adopted a full-scale five-storey testing structure to make an experimental comparison of different SA algorithms (Lyapunov algorithm, neurocontrol logic, and maximum energy dissipation algorithm) to control the behavior of the MR damper-based system, under the effect of four historical earthquakes and one artificial seismic input. Basili et al. [6] carried out shaking table tests to verify the effectiveness of a SA MR damper system in reducing seismic



FIGURE 2: The experimental mock-up structure.

electronic equipment for monitoring, and control). Then the SH controller is presented, as it has been designed for such particular application. With reference to a natural earthquake record, whose action is simulated through a shaking table facility, the response of the uncontrolled and of the SA controlled structure is compared in terms of displacements and accelerations, so as to evaluate the effectiveness of the SH controller in reducing the structural response of the frame.

2. Experimental Setup and Activity

The steel structure is a 2-storey one-bay steel frame with composite steel-reinforced concrete slabs (Figure 2). The mock-up structure is of plan size $3\text{ m} \times 4\text{ m}$ with a total height of about 4.5 m: four columns with HEB140 profile are placed at the corners with their flanges oriented parallel to the transverse (Y) axis. Four lateral beams IPE180, welded to the columns, comprise the first and second floors, while four lateral beams of HEB220 comprise the ground floor. Additionally, a horizontal bracing of HEA160 is provided on the horizontal plane at the ground floor. All structural elements are made of Fe360 steel. A concrete slab supported by coffer steel sections A55/P600 with 0.8 mm thickness is provided at the first and second floors. In order to make longer the vibration periods of the frame, a modified symmetrical configuration has been obtained by adding on each floor four concrete blocks with different masses of approximately 340 kg each (Figure 1). The frame is supported on special sliding 1D guides positioned under the base beams, close to the column location, which allow the frame to move in the longitudinal (X) direction only.

To allow the mounting of the semiactive devices, two chevron-type bracings made of steel profile HEA100 are mounted along the long edge (longitudinal) direction of the frame between ground and first floor and are connected to the lower floor beams at a certain distance from the columns.

The semiactive MR dampers have been provided by Maurer Söhne (Munich, Germany) and experimentally tested at the Laboratory of the Department of Structural Engineering

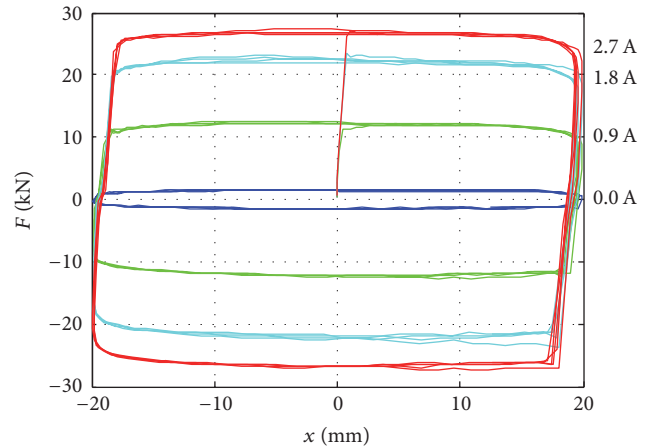


FIGURE 3: Cyclic force-displacement behaviour of the adopted prototype MR dampers [13].

of the University of Napoli Federico II, in order to evaluate the characteristics of their operations [13, 15]. They look pretty much like conventional fluid viscous damper, with the exception of some extra wiring needed to feed the coils inside the body. The absence of moving parts like electrically controlled valves or mechanisms make them very reliable with respect to other semiactive devices. Each prototype MR device has overall dimensions 675 mm (length) \times 100 mm (external diameter) and a mass, without connections, approximately equal to 16 kg; it can develop a maximum damping force of 30 kN along its longitudinal axis and the piston stroke is equal to ± 25 mm. The magnetic field produced in the device is generated by a magnetic circuit, and the current in the circuit, provided by a power supply commanded by a voltage input signal, is in the range $i = 0 \div 3$ A. Figure 3 shows the results of four “passive” tests performed during the experimental campaign described in [13, 15], carried out at the same displacement frequency (1.5 Hz) and amplitude (20 mm), supplying four different currents (0 A, 0.9 A, 1.8 A,

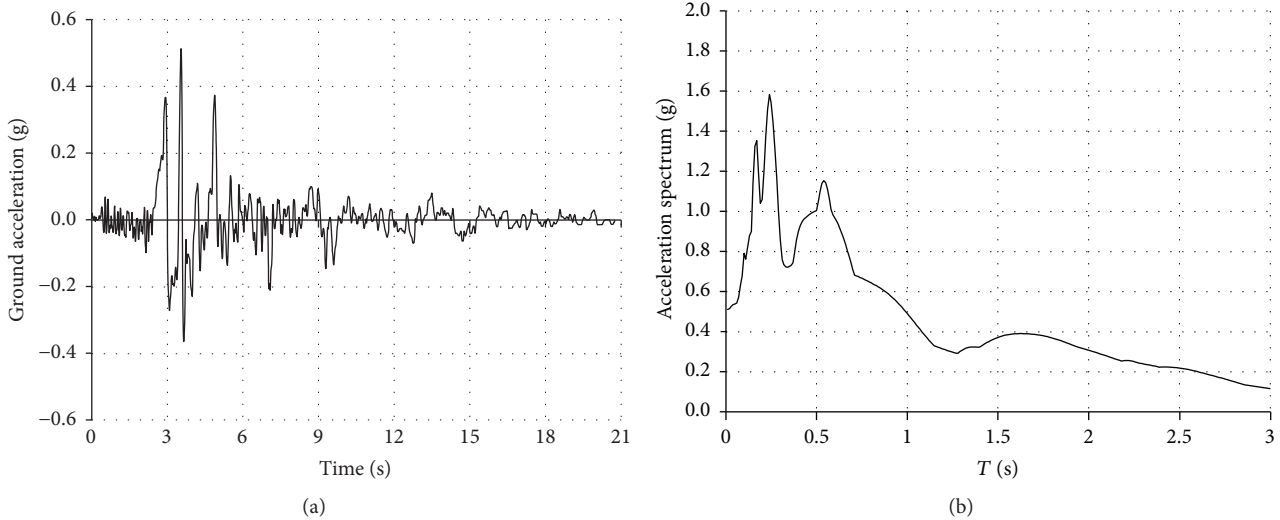


FIGURE 4: Erzincan earthquake: accelerogram (a) and 5% damped elastic acceleration spectra (b).

and 2.7 A). It shows how much the response behavior is variable according to the feeding current.

The registration of the Erzincan earthquake (code of the seismic record 000535y, direction N74E, magnitude 7.3, fault distance 8 km, date 13/03/1992, station Erzincan-Mudurlugu, Turkey) has been adopted for the experimental analyses (Figure 4).

The time scale of the accelerogram has been reduced by a factor $\sqrt{1.5}$ according to the scale of the model. Seismic input has been applied at increasing amplitudes for subsequent tests, up to the achievement of a safety limit value for the interstory drift (about 10 mm) or for the absolute floor acceleration (2 g). The said record 000535y has demonstrated to be particularly damaging for the structure; therefore, it has been applied scaled at a maximum 38% of its real intensity. In the following, this is the seismic load all the analyses and results will be referred to.

A total of 22 transducers were adopted to monitor the response of the structure during the SA tests [9, 16], placed as represented in Figure 5. The horizontal displacements of each floor were measured through four digital displacement transducers (D1 to D4) fixed to an external steel reference frame. The floor accelerations were recorded through four X-direction horizontal and four Y-direction horizontal (A5 to A12). The table-model base accelerations were recorded through two X-direction horizontal and two Y-direction accelerometers (A1 to A4), whereas the displacement by one digital transducer (D0) was fixed to the external steel reference frame. An additional accelerometer was adopted to measure acceleration of the actuator (A0) along its longitudinal axis. The remaining channels were used to measure the force of the dissipating devices, by means of piezoresistive load cells (F1 and F2) mounted at the end of each device and relative displacement, by means of four displacement transducers (D5 and D6). Table 1 gives detailed information about model and characteristics of the adopted sensors.

The special electronic equipment adopted to acquire the online measurement signals coming from the monitoring

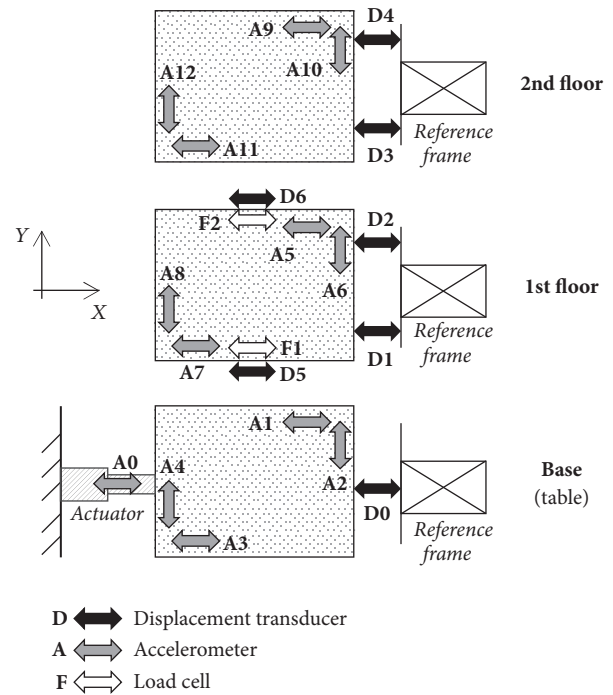


FIGURE 5: Plan view of base, 1st floor, and 2nd floor: position of sensors. D5 and D6 measured displacement demand in MR dampers. F1 and F2 measured the reaction's force of these devices.

activity and to drive MR dampers is depicted in Figure 6. The promptness of the whole system in acquiring and processing data and in commanding the dampers plays a crucial role for the effectiveness in controlling vibrations. Recent experimental studies [4, 17] highlighted the crucial role of the power supplies technology among the factors influencing the fast response of the SA control chain. Those referred to as “power source-power sink” allow to choose indifferently one of the two alternative schemes of control,

TABLE I: Sensors adopted to monitor the structural response during the tests.

Quantity	Transducer	Label in Figure 5
5	Temposonic digital transducers, ± 250 mm, $2 \mu\text{m}$ of resolution	D0 to D4
5	Columbia servo-accelerometers, model SA-107LN, ± 1 g	A0 to A4
2	Penny & Giles LP displacement transducers, type HLP190/SA, ± 50 mm	D5 to D6
8	FGP servoaccelerometers, model FA101-A2, ± 2 g	A5 to A12
2	AEP load cell, model TC4, ± 50 kN	F1 to F2

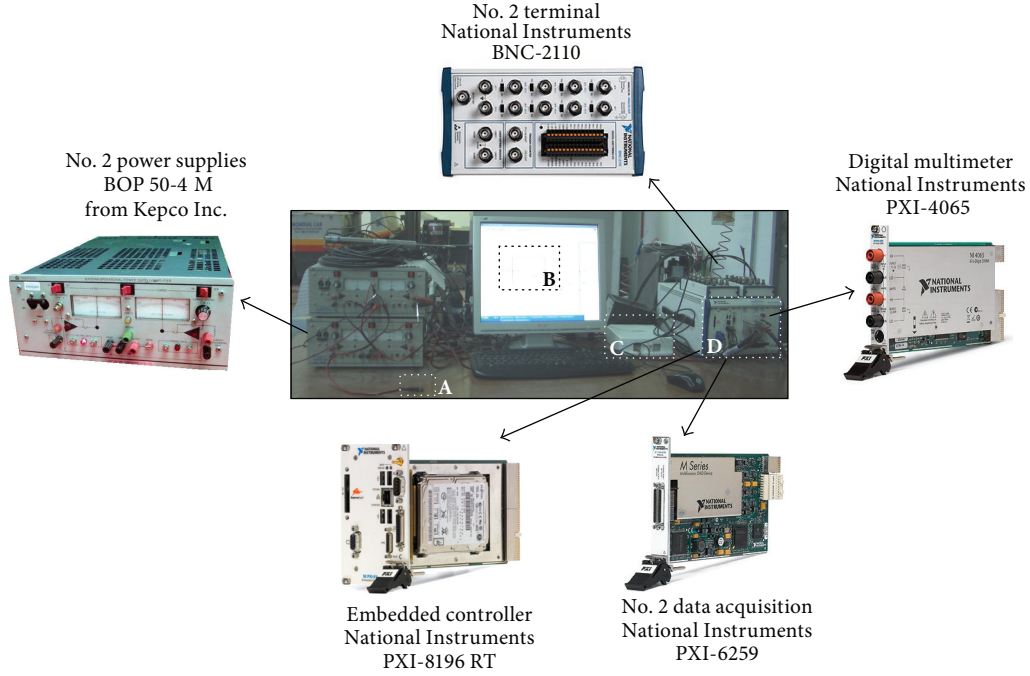


FIGURE 6: Electronic equipment for acquisition and control during the JET-PACS experimental tests.

that is, voltage-driven or control-driven. The voltage-driven scheme is demonstrated to lead to response delays more than an order of magnitude larger than those achievable with a current-driven approach. In the last case, the overall response time is comfortably bounded to 8~10 ms, so leading to negligible effects on the effectiveness of the control strategy.

In this case, operational power supplies BOP 50-4 M (Kepco Inc.) were adopted, with an output power of 200 W, a maximum input power of 450 W, and an output range of ± 50 V. Moreover, the tools they adopted to acquire signals, also usable for real applications, were a National Instruments (NI) PXI 6259 data acquisition board with 16 inputs and 4 outputs (± 10 V voltage signals, 16 bit resolution, and 2800 kHz maximum sampling rate), the NI Labview Professional Development System, release 8.5, digital multimeters to measure the intensity of current in the circuit of the MR dampers (Figure 6).

3. Design of a Semiactive Sky-Hook Damper

The control algorithm tested aimed to make the SA damper behave like a SH damper, that is, a damper constrained to the fixed space [2, 14, 18]. A conventional damper (Figure 7(a);

Figure 8, black lines) leads to resonance curves where for increasing values of damping the resonant response reduces, but this decrease is obtained only at the cost of an increased response for high frequencies. SH dampers (Figure 7(b); Figure 8, gray lines) guarantee an overall response reduction at all frequencies and tend to avoid resonance. Figure 8 is a rearrangement of what Karnopp et al. showed in [14]. A conventional and a SH damping scheme are compared showing the transmissibility of displacement from the base (x_0) to the vibrating mass (x , absolute) subjected to sinusoidal inputs with frequency ω . The natural frequency of the system is referred to as ω_n , while the damping ratio is ξ . For low input frequencies ($\omega < \omega_n$), small relative displacements occur for both systems. For values of ω close to ω_n the role of the damping becomes more evident and controls the resonance of the system. In this case, small values of damping ratio lead to high response of both dynamic systems. However, for higher values of ξ , it is worth noting that the resonance effect is highly mitigated, and the high frequency response decreases. A conventional damping scheme leads instead to resonance curves where increasing values of damping ratio still make the resonant response reduce, but this decrease is obtained only at the cost of an increased response against high frequencies.

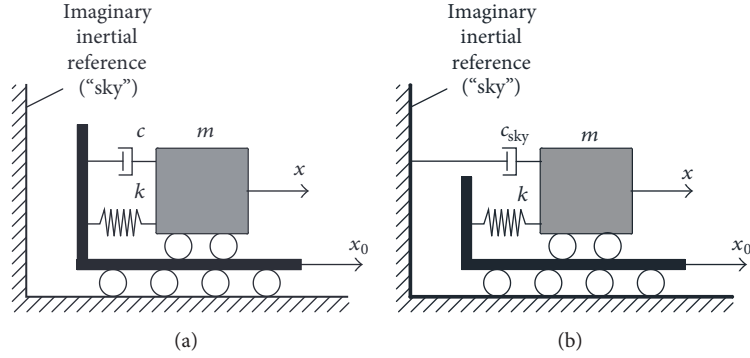


FIGURE 7: Conventional (a) and ideal sky-hook (b) damping schemes for a single degree of freedom system.

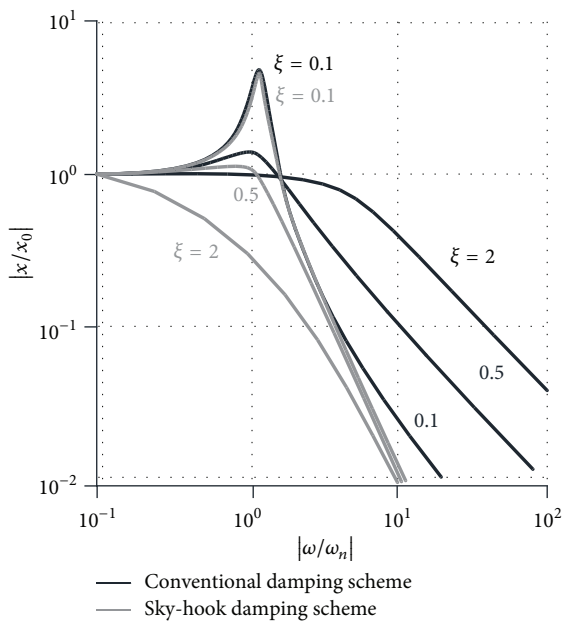


FIGURE 8: Conventional (black) and ideal sky-hook (grey) damping schemes: comparison of vibration transmissibility at three levels of damping ratio (rearranged from [14]).

The force exerted by the conventional viscous damper in Figure 7(a) is

$$F_v(t) = c \cdot [\dot{x}(t) - \dot{x}_0(t)], \quad (1)$$

whereas for a SH viscous damper (Figure 7(b)) it would be

$$F_{sky}(t) = c_{sky} \dot{x}(t), \quad (2)$$

where x and x_0 are, respectively, the absolute displacement of the mass and that of the base (ground).

Ideally, a conventional damper may behave like a SH device if its constant c could vary in real-time making, instant by instant, $F_v(t)$ equal to $F_{sky}(t)$. This could be actually realized by means of active control devices. Semiactive dampers cannot do exactly this; however, it can effectively mimic the behavior of a SH device if the SA control algorithm is based on a logic similar to that in (3), where $i(t)$ is the instantaneous

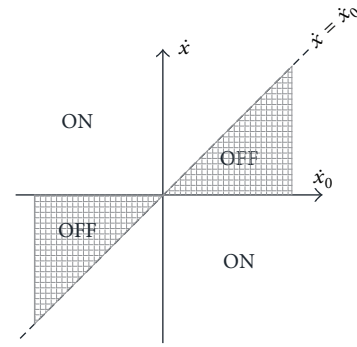


FIGURE 9: States of the MR dampers according to the velocity of the frame and of the ground, following the sky-hook control algorithm.

intensity of current given to the MR dampers. The same logic is also graphically depicted in Figure 9. In the instants of time when $F_v(t)$ have the same sign of the ideal SH force $F_{sky}(t)$, the SA damper is taken in the ON state (intensity of current set to the maximum value i_{min}). In the other cases, it is “turned” OFF (intensity of current set to the minimum value i_{min}) aiming to invert the undesired trend. This is because the damping constant cannot be set to a negative value. For the experimental study herein discussed, i_{min} has been set equal to 0 A. Two different configurations of the SH controller have been tested through the shaking table facility, once setting i_{max} equal to 1 A and once to A 2. As the reader can derive from Figure 3, the mechanical response of the MR dampers when fed with these two levels of current intensity is strongly different. Moreover, the current of 2 A almost leads to saturation of the magnetic field, as can be deduced again from Figure 3 where it can be observed that the response for current higher than 2 A is stronger, but not so much. Therefore, cases 1 A and 2 A can be considered representative of two opposite ways of calibrating the dampers.

$$\begin{aligned} \text{if } \dot{x}(\dot{x} - \dot{x}_0) \leq 0 & \text{ then } i(t) = i_{min} \text{ (OFF)} \\ \text{if } \dot{x}(\dot{x} - \dot{x}_0) > 0 & \text{ then } i(t) = i_{max} \text{ (ON)}. \end{aligned} \quad (3)$$

This controller has been adapted to the JETPACS steel structure as schematically represented in Figure 10 and preliminarily discussed in [19]. In more detail, on the left

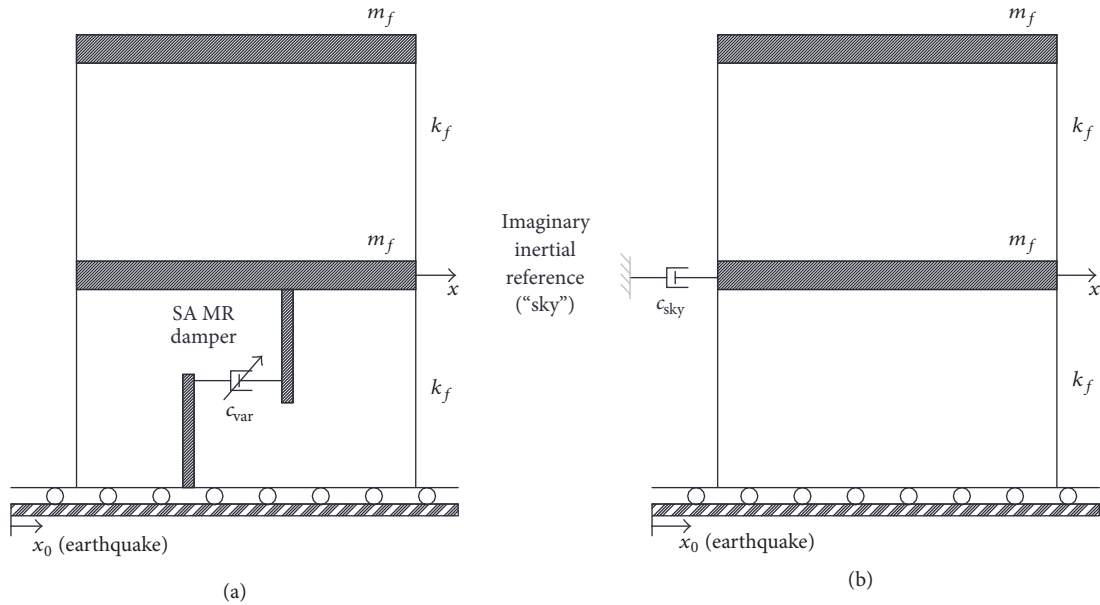


FIGURE 10: Sky-hook based semiactive control as designed for the case study structure (a). Sky-hook passive damping scheme taken as a reference to be emulated.

the meaning of x (1st floor absolute displacement) and x_0 (movement of the ground, i.e., of the shaking table) is described. It is worth noting that the idea of this study was that of controlling the vibrations of such multi-degree of freedom structure adding SA damping only at the first level. On the right, the passive structural scheme is taken as a reference to be emulated through SA control.

4. Experimental Results and Discussion

The main results of the experimental campaign have been reported and discussed in this section. The acronyms SH1A and SH2A are used to refer to the two tests done with SH SA control set with i_{max} equal to 1 A and 2 A, respectively. Figures 11(b) and 11(d) show the command voltage given to the MR dampers for tests SH1A and SH2A, respectively. It is worth noting that a 2 s long time window has been focused, in the most significant part of the motion, on a better readability of the charts. No evident difference is detected between the trends of the two graphs, except for the command voltage value corresponding to the ON state of the devices (about 2.5 V for SH1A, 5.0 V for SH2A). The SA control force exerted by the MR dampers during the two tests is shown in Figure 11(c). Peak values have been detected to be 10 kN and 18 kN for the two above SA tests, respectively.

The performance of the SA SH control strategy is evaluated comparing the response of the uncontrolled and controlled structure in terms of interstory drift demand, floor acceleration, and floor response spectra (FRS). The latter, as known, is strongly related to nonstructural components and contents demand [20].

Figure 12 summarizes the results in terms of lateral displacement demand. It allows clearly highlighting the significant reduction of demand the proposed control strategy in the SH1A case led to. Actually in this case the maximum 1st

interstory drift resulted in being 5.1 mm for the uncontrolled structure and 2.7 mm for the controlled case. The maximum 2nd interstory drift passed from 6.9 mm to 4.7 mm. Therefore a 30–45% of reduction in terms of displacements has been achieved. The SH2A test did not lead to the same good results. The peak value of displacement demand at the 1st level is reduced less than in the SH1A case, while at the 2nd level it results in being even greater (8.3 mm) than the value (6.9 mm) registered for the uncontrolled configuration.

Figure 13 shows floor acceleration time histories and spectra for the uncontrolled and the controlled structure, both for the SH1A and SH2A tests. Also in this case, the test SH1A led to better results compared to SH2A, given that the demand resulted in being strongly reduced for both levels of the structure. Calibration of the SA control with 2A (test SH2A) even led to a worsening of the response for the first floor (peak acceleration 0.67 g in the uncontrolled case, 0.97 g in the SH2A case), at the same time not significantly reducing the large acceleration demand at the roof level. To the contrary, the SH1A test led to a strong mitigation of floors' acceleration demand, with percentage reduction in the range 30–50%.

As known, the floor acceleration is one of the more effective parameters to measure seismic demand to nonstructural components and contents. Figures 13(e) and 13(f) show the 1st and 2nd floor response spectra, respectively. It is worth noting that both SA tests led to a high reduction of spectral accelerations in the low frequency range. However, for higher frequencies (lower periods) the trend is different. The SH1A test leads to results similar to those of the naked structure, even reducing the peak value, which occur for a period of about 0.08 s. To the contrary, the SH2A test resulted in amplifying acceleration demand for low period (<0.1 s) components, in some cases even leading to spectral ordinates that are three times those of the uncontrolled structure. Also

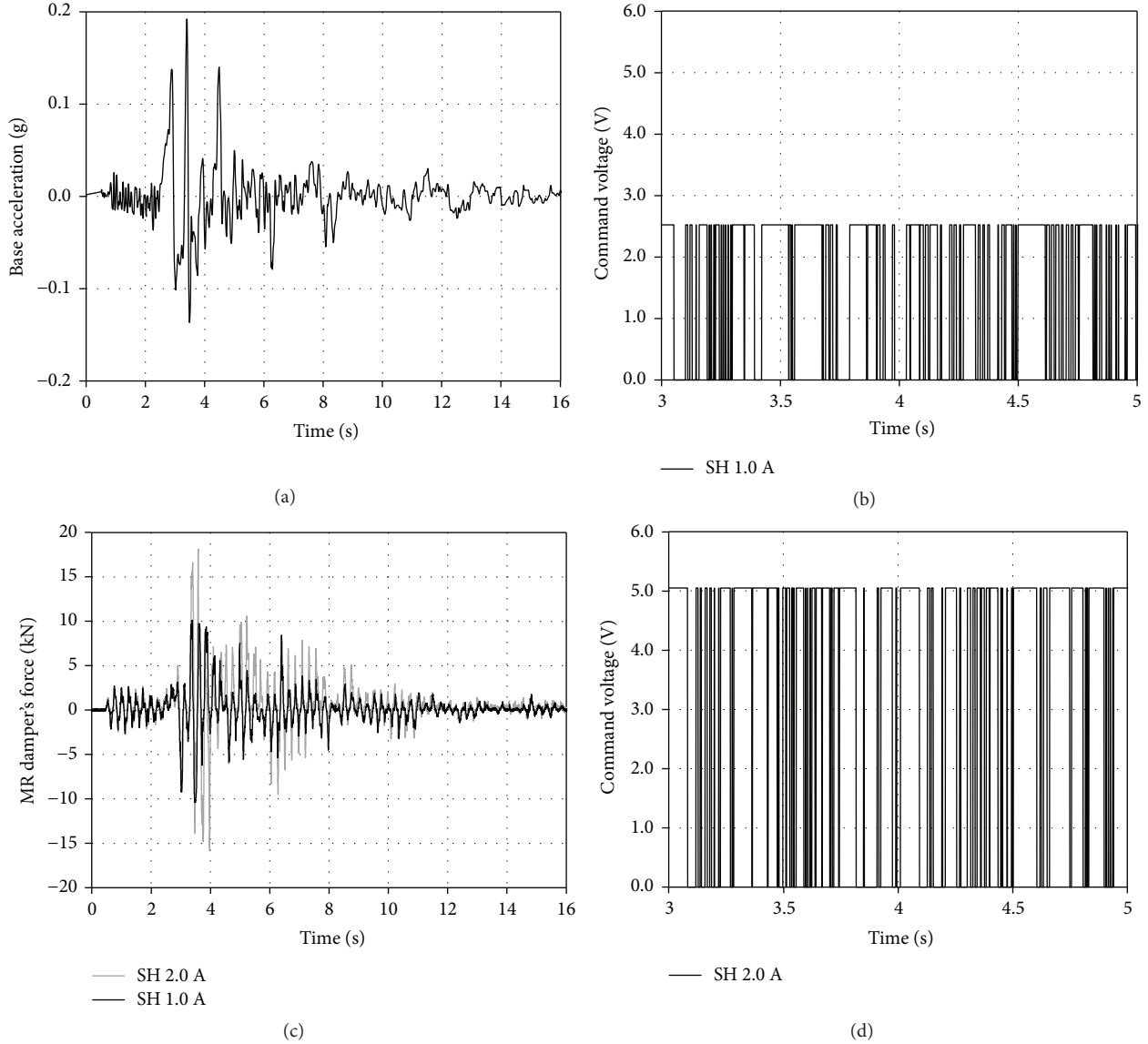


FIGURE 11: SA tests: registration of base acceleration (a), command voltage (b, d), and damper's reacting force (c).

peak value at 0.08 s results in being amplified when the structure is SA controlled using $i_{\max} = 2$ A.

To further compare the three cases (uncontrolled, SH1A, and SH2A) in terms of demand to nonstructural components, four special periods of vibration have been selected and focused on. The results are summarized in Table 2. Selected periods are referred to generic components that could be installed to one of the two floors. In more detail,

- (i) case (a) refers to a hypothetical component firmly fixed (period $T = 0$) to the slab of the 1st or 2nd floor; it is worth noting that, in such case, the spectral accelerations are equal to the PFA (peak floor accelerations) highlighted in Figures 13(a)–13(d);
- (ii) case (b) is an ideal hollow clay partition wall having dimensions $2.5 \times 2 \times 0.3$ m and weight per unit volume 8 kN/m^3 ; according to the Italian building

code [21], the vibration period of such component is equal to 0.02 s;

- (iii) case (c) is that of a component whose fundamental period is equal to the first resonance period of the floor where it is installed (0.29 s for the naked structure, 0.24 s for the SA controlled cases);
- (iv) case (d) is that of a component whose fundamental period equal to the second resonance period of the floor where it is installed (0.09 s for the naked structure, 0.08 s for the SA controlled cases).

Numerical values in Table 2 allow underlining once again that the SH controller calibrated with $i_{\max} = 1$ A results in being more effective in reducing seismic demand to nonstructural elements. When it is calibrated with $i_{\max} = 2$ A, the dynamic response is sometimes even worse than the uncontrolled case, especially at the first floor.

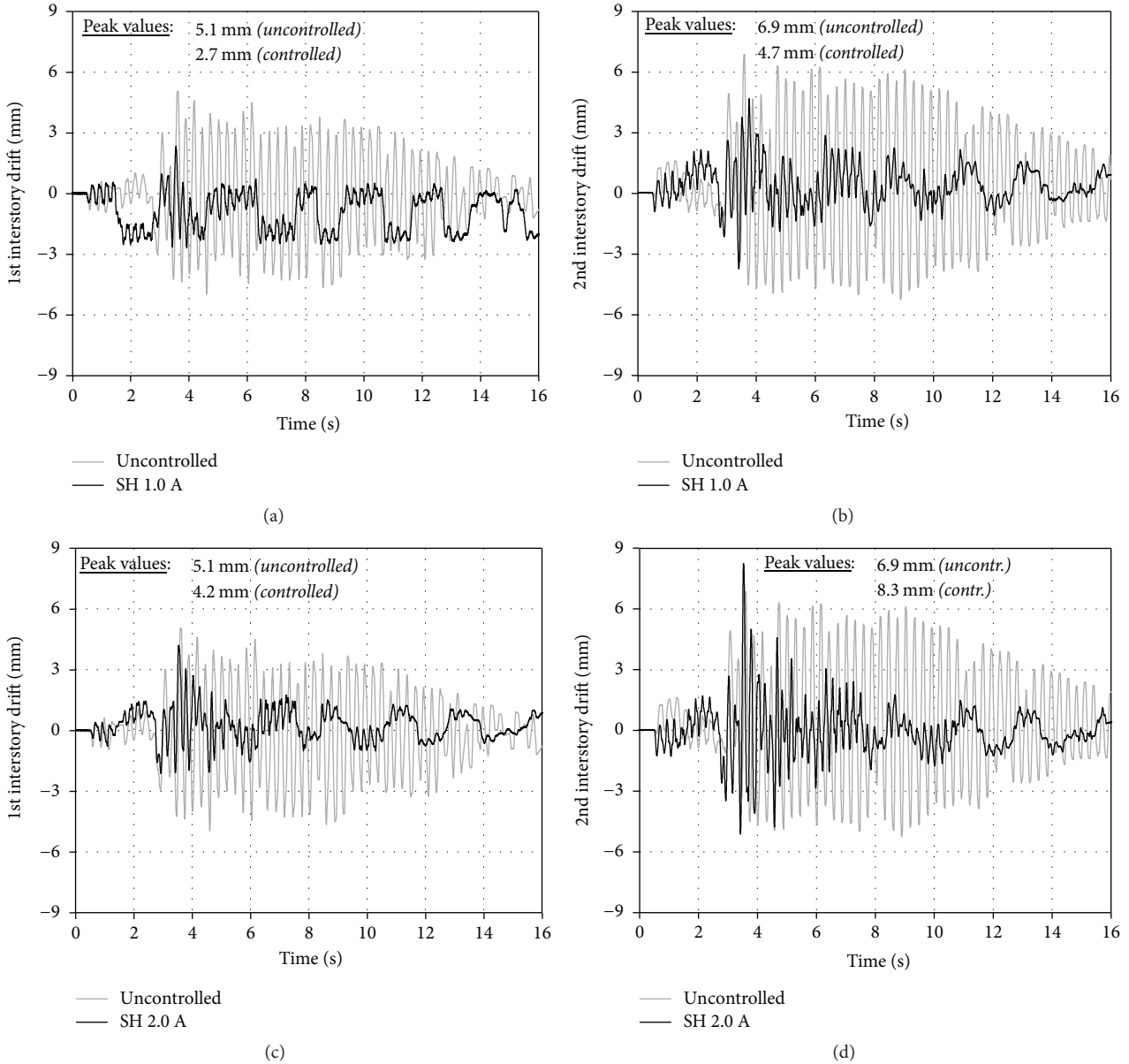


FIGURE 12: Response reduction in terms of interstory drifts for both SH1A and SH2A tests.

TABLE 2: Floor spectral accelerations for selected periods of vibration of nonstructural components, corresponding to the cases of (a) a component firmly fixed to the slab, (b) a partition wall, and an element in resonance with the first (c) and the second (d) frequencies.

Case	T [s]	Spectral 1st floor acceleration [g]			Spectral 2nd floor acceleration [g]		
		Uncontrolled	SH 1 A	SH 2 A	Uncontrolled	SH 1 A	SH 2 A
(a)	0.00	0.67	0.45	0.97	1.11	0.54	0.91
(b)	0.02	0.72	0.71	1.63	1.21	0.80	1.29
(c)	0.24–0.29	17.00	2.30	2.70	33.00	5.10	7.00
(d)	0.08–0.09	4.70	4.10	5.00	3.60	2.40	2.80

5. Conclusions

The main results of a wide experimental campaign on a near full-scale semiactively controlled steel building have been presented and discussed. A sky-hook damping based control

algorithms driving SA MR dampers have been investigated through shaking table tests under the action of a natural earthquake. The control logic is able to change in real-time the dynamical properties of the dampers according to the actual values of response quantities measured in the close

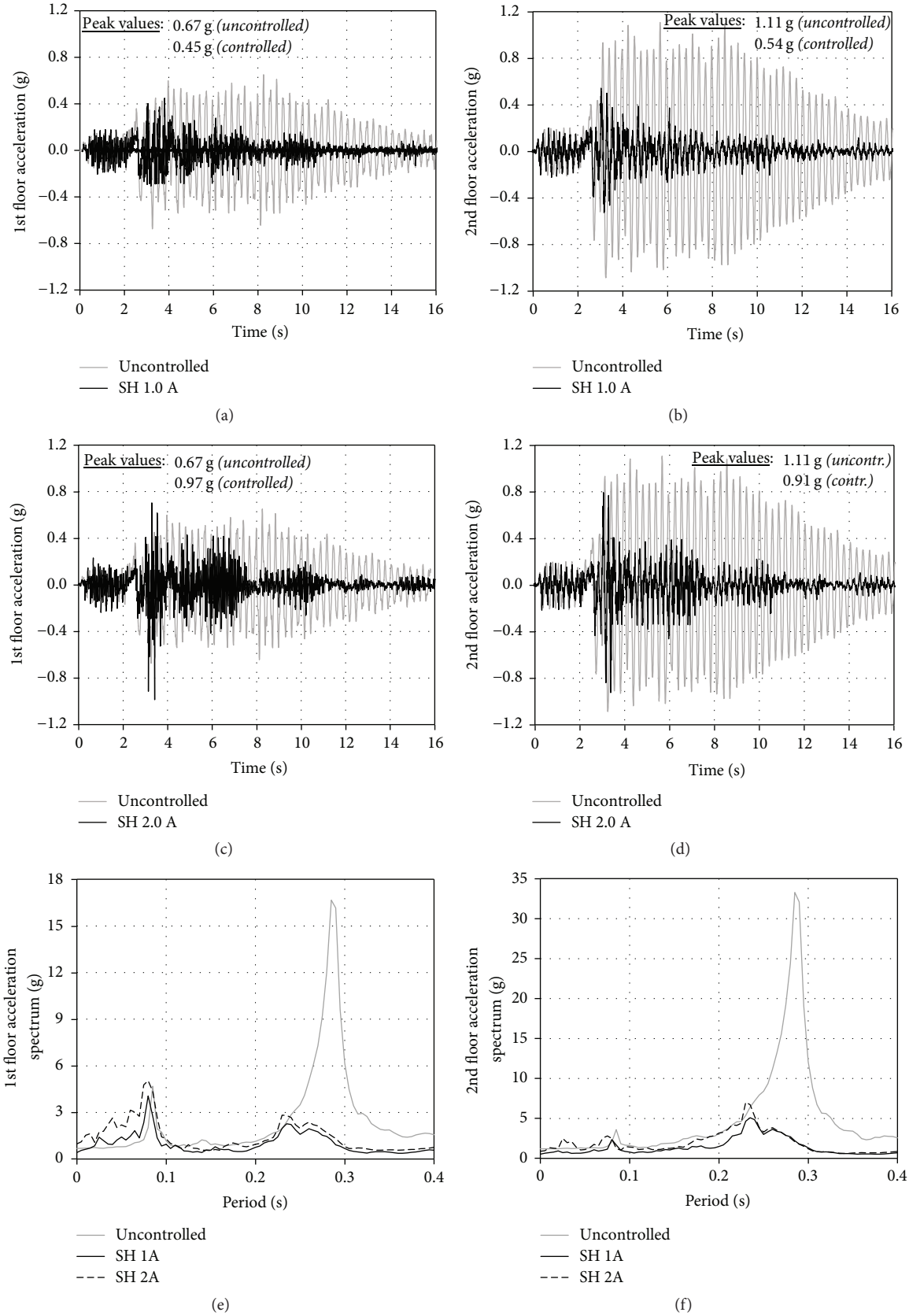


FIGURE 13: Comparison of uncontrolled and controlled (tests SH1A and SH2A) response in terms of floor acceleration time histories (a to d) and spectra (e, f).

surroundings of the dampers. It aims to make the MR device mimic the behaviour of a damper constrained to the fixed space.

The effectiveness of the control system related to two different configurations of the controller has been compared. The latter were different only because of the maximum value of feeding current (1 A and 2 A, resp.). The gained results led to the following main conclusions.

The experimental response reduction in terms of inter-story drifts and accelerations achieved by SA control system in the SH1A case, compared to the bare, uncontrolled frame, can be even close to 50%. The control strategy results in being particularly effective in reducing the floor accelerations, so achieving a high seismic protection for nonstructural components and contents potentially installed at the two storeys of the structure. The performance of the SA controller configured with $i_{\max} = 2$ A (test SH2A) is not satisfactory to the same extent. As a matter of fact, the structural response in this case is slightly better than the uncontrolled case, or even worse, in terms of displacement as well as acceleration demand.

The so different performance of the control strategy in the cases SH1A and SH2A is mainly due to the fact that the MR devices were installed at the first storey only. When they were set to be “stronger” (i.e., when higher intensity of current was used), reaction forces became higher and resulted in a more abrupt change over time. Since they acted at the first level only, they undesirably tended to activate the participation of the second vibration mode, which was less involved in the motion of the uncontrolled structure. This outcome could be taken as a general indication for semiactively controlled systems when smart devices cannot be present on all floors (e.g., for architectural or cost limitations). In similar cases, the additional damping should not be too high, so as not to favor irregularities in height and undesired amplification of the structural response.

Further analyses have been programmed by the authors to be done with reference to different seismic loads and configurations of the controller. This will allow gathering additional information useful to understand how, in real applications, the SA control strategy could be calibrated in order to be effective in reducing the structural response.

Conflicts of Interest

The authors declare that they have no conflicts of interest.

Acknowledgments

The research activity has been supported by the University of Naples “Parthenope” with a grant within the call “Support for Individual Research for the 2015–17 Period” issued by Rectoral Decree no. 953-954/2016 and in the framework of the ReLUIIS Research Project funded by the Italian Department for Civil Protection. The above supports are gratefully acknowledged. The dampers have been designed, manufactured, and provided for free by Maurer Söhne (Munich, Germany) that is also acknowledged for the support.

References

- [1] T. Kobori, M. Takahashi, T. Nasu, N. Niwa, and K. Ogasawara, “Seismic response controlled structure with active variable stiffness system,” *Earthquake Engineering & Structural Dynamics*, vol. 22, no. 11, pp. 925–941, 1993.
- [2] M. J. Crosby and D. C. Karnopp, *The Shock and Vibrations Bulletin*, vol. 43, Naval Research Laboratory, Washington DC, USA, 1973.
- [3] D. Cao, X. Song, and M. Ahmadian, “Editors’ perspectives: road vehicle suspension design, dynamics, and control,” *Vehicle System Dynamics*, vol. 49, no. 1-2, pp. 3–28, 2011.
- [4] Z.-X. Li and L.-H. Xu, “Shaking-table test on semi-active control for seismic response of tall buildings using MRF-04K damper,” in *Proceedings of the 13th World Conference on Earthquake Engineering*, Vancouver, B.C., Canada, 2004.
- [5] H.-J. Lee, H.-J. Jung, S.-J. Moon, S.-K. Lee, E.-C. Park, and K.-W. Min, “Experimental investigation of MR damper-based semiactive control algorithms for full-scale five-story steel frame building,” *Journal of Intelligent Material Systems and Structures*, vol. 21, no. 10, pp. 1025–1037, 2010.
- [6] M. Basili, M. De Angelis, and G. Fraraccio, “Shaking table experimentation on adjacent structures controlled by passive and semi-active MR dampers,” *Structures of Sound and Vibration*, vol. 332, no. 13, pp. 3113–3133, 2013.
- [7] Y.-J. Cha, J. Zhang, A. K. Agrawal et al., “Comparative studies of semiactive control strategies for MR dampers: Pure simulation and real-time hybrid tests,” *Journal of Structural Engineering (United States)*, vol. 139, no. 7, pp. 1237–1248, 2013.
- [8] N. Caterino, M. Spizzuoco, and A. Occhiuzzi, “Shaking table testing of a steel frame structure equipped with semi-active MR dampers: comparison of control algorithms,” *Smart Structures and Systems*, vol. 15, no. 4, pp. 963–995, 2015.
- [9] F. C. Ponzio, A. Di Cesare, C. Moroni et al., “JET-PACS: Joint Experimental Testing on Passive and semiActive Control Systems,” in *Proceedings of the L’Ingegneria Sismica in Italia – XIII Convegno Nazionale dell’ANIDIS*, Bologna, Italy, 2009.
- [10] A. Occhiuzzi and M. Spizzuoco, “Experimental analysis of a semi-actively controlled steel building,” *Structural Engineering and Mechanics*, vol. 19, no. 6, pp. 721–747, 2005.
- [11] J. A. Inaudi, “Performance of variable-damping systems: theoretical analysis and simulation,” in *Structural Control for Civil and Infrastructure Engineering*, F. Casciati and G. Magonette, Eds., World Scientific, pp. 301–316, 2000.
- [12] C. W. Stammers and T. Sireteanu, “Vibration control of machines by use of semi-active dry friction damping,” *Journal of Sound and Vibration*, vol. 209, no. 4, pp. 671–684, 1998.
- [13] N. Caterino, M. Spizzuoco, and A. Occhiuzzi, “Understanding and modelling the physical behaviour of magnetorheological dampers for seismic structural control,” *Smart Materials and Structures*, vol. 20, no. 6, Article ID 065013, 2011.
- [14] D. Karnopp, M. J. Crosby, and R. A. Harwood, “Vibration control using semi-active force generators,” *Journal of Manufacturing Science and Engineering*, vol. 96, no. 2, pp. 619–626, 1974.
- [15] N. Caterino, M. Spizzuoco, and A. Occhiuzzi, “Promptness and dissipative capacity of MR dampers: experimental investigations,” *Structural Control and Health Monitoring*, vol. 20, no. 12, pp. 1424–1440, 2013.
- [16] A. Di Cesare, F. C. Ponzio, D. Nigro, M. Dolce, and C. Moroni, “Experimental and numerical behaviour of hysteretic and visco-recentring energy dissipating bracing systems,” *Bulletin of Earthquake Engineering*, vol. 10, no. 5, pp. 1585–1607, 2012.

- [17] N. Caterino, M. Spizzuoco, J. M. Londoño, and A. Occhiuzzi, "Experimental issues in testing a semiactive technique to control earthquake induced vibration," *Modelling and Simulation in Engineering*, vol. 2014, Article ID 535434, 11 pages, 2014.
- [18] A. Preumont, *Vibration control of active structures*, Kluwer Academic Publishers, 2nd edition, 2002.
- [19] N. Caterino, M. Spizzuoco, and A. Occhiuzzi, "Skyhook-based monitoring and control of a steel building under seismic action," in *Proceedings of the 2016 IEEE Workshop on Environmental, Energy, and Structural Monitoring Systems, EESMS 2016*, Italy, June 2016.
- [20] J. L. Sackman and J. M. Kelly, "Seismic analysis of internal equipment and components in structures," *Engineering Structures*, vol. 1, no. 4, pp. 179–190, 1979.
- [21] NTC08, "Norme Tecniche per le Costruzioni," D.M. 14.01.2008. (In Italian).

Research Article

Mechanical Performance and Design Method of Improved Lead Shear Damper with Long Stroke

Baoshun Wang, Weiming Yan, and Haoxiang He 

Beijing Key Laboratory of Earthquake Engineering and Structural Retrofit, Beijing University of Technology, Beijing 100124, China

Correspondence should be addressed to Haoxiang He; hxx7856@163.com

Received 2 July 2017; Revised 12 November 2017; Accepted 2 January 2018; Published 29 January 2018

Academic Editor: Felice Ponso

Copyright © 2018 Baoshun Wang et al. This is an open access article distributed under the Creative Commons Attribution License, which permits unrestricted use, distribution, and reproduction in any medium, provided the original work is properly cited.

The paper presents experimental study on an improved plate lead shear damper with long stroke (ILSD-LS) which is developed to meet the engineering requirements for high-rise structures with long periods subjected to the long-period earthquakes. Finite element analysis is also carried out to investigate the proposed damper. Based on the ideal rigid-plastic constitutive law of lead, a mechanical model of the ILSD-LS is established. Compared with ordinary dampers, ILSD-LS has better damping force, energy dissipation capacity, and stability according to the results of simulation and experiments. The method of calculating damping force is reasonable and accurate. In order to verify the damping effect of ILSD-LS for the structures with long periods under long-period ground motions, the nonlinear time history analysis of a typical high-rise structure with ILSD-LS is carried out. The numerical results indicate that the seismic responses of the high-rise structure with ILSD-LS are significantly reduced when subjected to long-period ground motion.

1. Introduction

Earthquake can generate huge loss and damage to human beings and society, so it is meaningful to study the dynamic effect of ground motion on structure and to reduce structural vibration with high-performance dampers.

According to epicentral distance, ground motion can be divided into the near-field earthquake and the far-field earthquake, and the far-field vibration is also called long-period ground motion. In earthquake engineering, long-period ground motion usually refers to the ground motion whose predominant period ranges from 2 s to 10 s, and long-period components are abundant in this range [1]. Long-period ground motion is often characterized by relatively low acceleration, low frequency components mainly concentrated in the later stage, large velocity and displacement, long duration, and so on. The previous earthquake damage phenomena show that the tall building structures with long periods may generate large horizontal displacement and serious damage under the action of far-field earthquake with rich long-period components. In addition, with the development of city construction and the increasing social demand, the form of

high-rise building structure is becoming more flexible and complex. For typical high-rise buildings such as large span structure, tall structure, and long-span suspension structure, they have longer natural periods and many of them are important lifeline projects; the seismic performance is very important for the normal use of structures and the safety of public life. Hence, it is necessary to carry out seismic research and structural control technology of long-period structures.

In civil engineering structure, the structural control technology is developing vigorously. The control system mainly reduces the structural vibration to prevent damage to structures subjected to natural disasters such as wind and earthquake. The structure can be controlled by the active control system and the passive control system. Since the active control system needs to input higher external energy and has higher developing costs, the passive control system is preferred in general structures. Passive control system mainly uses energy dissipation components such as dampers to dissipate dynamic energy. The main dampers currently include friction dampers, viscoelastic dampers, viscous dampers, metal dampers, and tuned mass dampers, and the corresponding theoretical research and technology

are intensively studied. If the traditional dampers are installed on the high-rise building structure, the structural deformation may exceed the effective stroke of the damper under long-period ground motion, so the performance of the damper is not fully exploited; even the damper itself could fail. Therefore, it is necessary to use large stroke dampers to reduce vibration for high-rise building structure subjected to long-period earthquake. Compared with the traditional damper, the requirements of the composition, design scheme, and production accuracy for the large stroke damper are higher; the stroke especially should fully meet the engineering demand, and the stroke distance is usually in tens of centimeters. At present, the research on the structure and mechanical properties and design method of large stroke damper has a promising tendency towards development, so it is necessary to carry out in-depth theoretical and experimental research.

In order to develop long-stroke dampers, the characteristics and the potential of various traditional dampers can be considered. Friction damper has the strong capacity of energy dissipation; the load frequency has little influence on the performance, and it has the advantages such as simple structure, easy material selection, and low cost. However, the friction damper's performance relies on the materials' long-term static contact in the constant positive pressure, which will produce cold bonding or solidification. The desired coefficient of friction cannot be guaranteed, and loading cycles will also dramatically reduce the friction coefficient of the damper; this makes the friction device unfavorable. In addition, the friction damper will produce permanent deviation after large displacement of structure occurs. It also needs maintenance and protection, so its energy dissipation capacity is limited [2–4].

Viscoelastic dampers can dissipate energy with small vibration amplitudes, and they have stable dynamic performance and strong capacity of energy dissipation under different loading frequencies and cycle numbers. However, its energy dissipation capacity decreases with the increase of temperature and strain amplitude [5–7]. Although viscous damper has strong capacity of energy dissipation under small deformation, it has low efficiency of shock absorption and no additional stiffness to the main structure. Therefore it is hard to meet the performance requirements for strong earthquake or large deformation [8–10].

As a typical kind of metal damper, low-yield point steel damper has the advantages of stable hysteretic characteristics, simple structure, and easy replacement after the earthquake, and so on. However, it will cause distortion of hysteresis loop if the shape of low-yield point damper is not suitable. In addition, the damper can just play a role in the strong earthquake, and it accumulates deformation in the earthquake and wind excitation; the hardening of steel makes the seismic response of the structure seriously inconsistent with the design [11–14].

Although the tuned mass damper (TMD) is easy to install, maintain, and replace, the TMD has a damping effect on the structure only for limited tuning frequency bands, and severe time-delay phenomenon may occur especially when large structural deformations appear [15–18]. Therefore, it will inevitably cause defects and hidden dangers to directly

enlarge the stroke of these dampers or simply adjust them into large stroke dampers.

Compared with other metal materials, lead has advantages of high density, high stiffness, good flexibility, and ductility, and a large amount of energy can be absorbed during its deformation. Since the melting point of lead is lower, deformation will take place during dynamic recovery and dynamic recrystallization process. In theory, the cumulative fatigue phenomenon will not occur after the plastic cyclic at room temperature. Therefore, the lead damper has the advantages of high energy dissipation and stable performance and it is suitable for the engineering requirement of long-stroke dampers. At present, the typical lead dampers in civil engineering application include lead extrusion damper [19, 20], lead shear damper [21, 22], and cylindrical damper [23]. Lead shear damper has been extensively used in practical engineering. Robinson and Greenbank firstly proposed one such device that was an energy absorber extruding lead back and forth through an orifice [24]. Tsai et al. have tested and explored the characteristics of the new lead extrusion damper (LED). The test results showed that the new LED possessed excellent capability for energy absorption. The hysteresis loop behaved like “plastic solids” or “coulomb dampers.” The internal force and the speed of the movement were correlated while the damper was subjected to harmonic loadings. By comparing the numerical results obtained from the proposed analytical model with experimental results under various displacements and frequencies, Tsai et al. concluded that a good agreement between the computational and experimental results has been achieved [20]. Curadelli and Riera proposed a new type of lead ring shearing metal damper of energy dissipation and established relevant design and performance measurement methods [22]. Monti and Robinson proposed a damper based on shear deformation of lead, and the effectiveness of the device was proved by experimental research and theoretical analysis. The damper could be used in buildings or industrial structures to resist external excitations such as wind, earthquake, and traffic [25].

Although the research on the seismic performance of the traditional lead damper is sufficient, there is still a lack of study on the effect of lead damper on high-rise structures subjected to long-period ground motion. The research on the structure and seismic performance with long-stroke lead shear damper is also relatively limited.

Ni et al. designed a magnetorheological damper with large stroke, in which the damping effect was studied through a scaled adjacent structural system consisting of a 12-story building model and an 8-story building model, and a shaking table test was carried out. The results showed that the magnetorheological (MR) damper of large stroke provided effective damping effect, but the location of the damper was the main factor affecting the control efficiency [26]. Behrens et al. proposed an electromagnetic shunt damper (EMSD). It required small shunt voltages, provided large stroke, and reduced the vibration of larger mechanical structures; the theoretical results were also presented [27]. In order to meet the needs of large stroke and large output of high-rise buildings, a new type of intelligent friction damper was proposed based on constrained energy dissipation system by Zhou and Peng

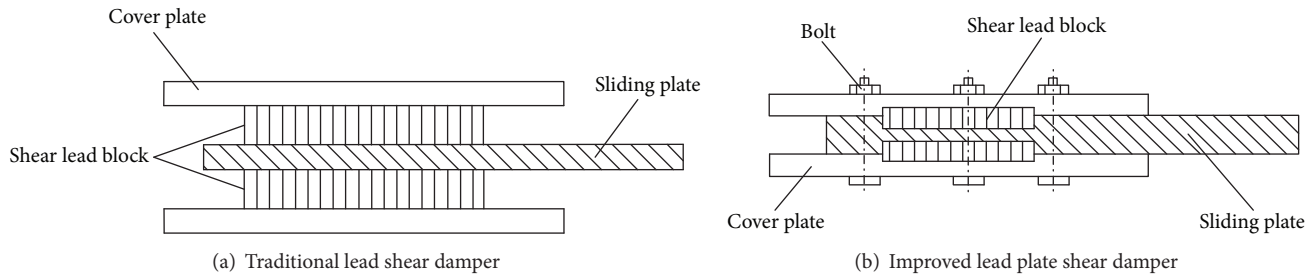


FIGURE 1: Ordinary plate lead shear damper.

[28]. Through the finite element analysis of damper and the nonlinear time history analysis of a structure equipped with dampers, it was proved that the new type of intelligent friction damper had larger friction force and larger allowable displacement, meeting the requirements of engineering applications. Aiming at the demand for viscous dampers with large stroke and strong energy dissipation for the building structures subjected to long time periodic earthquake, Minagawa et al. proposed a viscous-friction hybrid damper as an effective vibration control device suitable for structures having long natural period. The hybrid damper consisted of an oil damper and a friction damper in series [29]. Seismic response analysis of a boiler building with the hybrid damper was carried out, and superior damping performance was confirmed.

Many researchers have also studied the application of long-stroke damper in the seismic design of bridges. Sharabash and Andrawes developed a super elastic shape memory alloy device (SMA). The experiments showed that the stroke of this device could reach 80 mm and the performance of energy dissipation was stable [30]. SMA was applied to the three long-span bridge model; it was shown that the damper could improve the seismic performance of the bridge. Shen et al. proposed a novel system with transverse steel dampers (TSDs) [31]. The experimental results showed that the TSD had excellent performance in energy dissipation, large displacements, and synchronization of triangular plates under complex contact conditions. A 620 m long-span cable-stayed bridge was selected for a case study of the TSD seismic system. The ground motions records considering various site conditions were used as seismic inputs. Numerical results proved that the TSD system had good energy dissipation ability and it was insensitive to the input characteristics of ground motion.

A new type of lead shear damper with capabilities of large deformation was used to achieve energy dissipation by Zhou et al. [21]. It was found that the damping effect of this new damper was as good as normal viscous damper, and leakage and metamorphism did not occur for the new damper. In addition, the new damper was much cheaper than viscous damper. Hence, the lead shear damper has an excellent prospect in structure control. Although the traditional lead plate damper is simpler and cheaper than the magnetorheological damper, friction damper, and viscous damper, it still cannot meet the requirements of large deformation and energy dissipation stability for large structures. Considering

theoretical analysis, processing cost, and engineering feasibility, it is significant to develop a new type of lead plate damper with long stroke and high performance.

The previous research provided basic methods and ideas for the design and analysis of lead plate damper with long stroke. However, since the yield point of lead is low and it is hard to fill up during perfusion, the yield force of normal damper is not sufficient, and the capacity of energy dissipation is unstable. Hence, it is necessary to improve the mechanical structure of the current lead plate damper with long stroke to keep its capacity of energy dissipation to be strong and stable during large deformation. Furthermore, the theoretical method of the damper with long stroke should be established. In consideration of the study of long-stroke dampers for building structures not sufficient enough, this study is mainly aimed at investigating the seismic response of long-span or large-deformation building structures with long-stroke dampers.

An improved lead shear damper with long stroke (ILSD-LS) is proposed in this paper; the mechanical model is established, and the finite element simulation is carried out. The actual performance of ILSD-LS is tested by low cycle reciprocating cycle load experiment. The structural time history analysis of high-rise building with ILSD-LS is studied. The results show that the mechanical model of the damper is in good agreement with the experimental results, and the damper has the advantages of large stroke and stable performance.

2. Mechanical Structure of ILSD-LS

The mechanical structure of the traditional lead shear damper is shown in Figure 1(a); the main shortcoming is that the machining requirement of the connection between shear lead block and cover plate is strict; thus the actual yield force of the damper is extremely unstable when longer stroke and larger damping force are needed.

For the improved lead plate shear damper, the mechanical structure is shown in Figure 1(b). Once the stroke exceeds the relative shear length of the lead block, the effective shearing area of lead block rapidly decreases and the output force of the damper declines, so the performance of energy dissipation of the improved lead plate shear damper is still unstable.

To meet the damper requirements of higher yield force and larger stroke for practical engineering, the lead plate

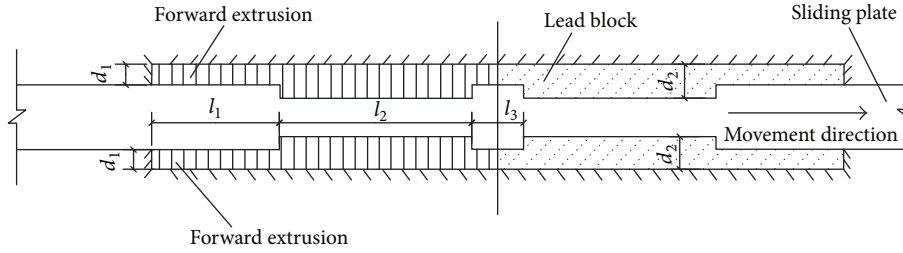


FIGURE 4: Structure and dimension of ILSD-LS.

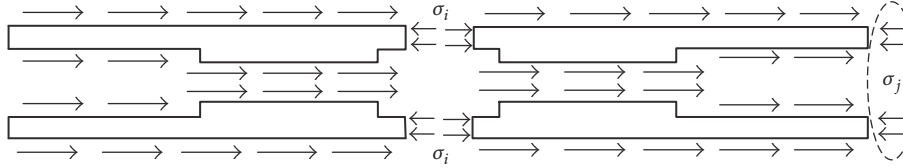


FIGURE 5: Stress distribution diagram of ILSD-LS.

the side baffle and the slide plate. Two end blocks are welded along the width direction of each cover plate, and there is no gap between the end block and the upper and lower surfaces of the slide plate. Two side blocks are welded in the width direction at the inner end of each side baffle, and there is also no gap between the side block and the slide plate. The inner surfaces of the upper cover plate and the lower cover plate are welded with end cover-plate bar and central cover-plate bar. The central sliding plate bars are respectively welded in the middle part of the two grooves of the sliding plate; besides the end cover-plate bar is required to be separated from the sliding plate without clearance. There is no connection between the central cover-plate bar and the central sliding plate bar, but no clearance exists between both of them. Then a cavity is constituted by fixing cover plate, sliding plate, side baffle, side block, and end baffle by bolts. Finally, the melted lead poured into the cavity solidifies into the block. To reduce the relative shear length of the lead block and ensure the lead block to yield completely, the internal lead block of ILSD-LS is treated separately and the additional constraints are added. The shear lead blocks in the groove will dissipate energy continuously when the sliding plate reciprocally moves.

3. Mechanical Model of ILSD-LS

In traditional analysis, the shear lead block is assumed to generate shear deformation in the axial direction and yield at the same time when the yield force of the shear lead damper is calculated. For ILSD-LS, the lead blocks in the lead grooves are in compressional stress state during the sliding plate reciprocal movements; thus, ILSD-LS can be considered as an extrusion damper. Therefore, the lead in operation can be assumed as ideal rigid plastic material, and the mechanical model of ILSD-LS is established according to the microstress state of lead.

The dimension of the ILSD-LS is shown in Figure 4, and the lateral width of the damper is set as B . Based on the

ideal rigid-plastic constitutive law of lead, it is assumed that the shear deformation of the lead is homogeneous and the friction forces of sliding plate, side plate, and lead and side plate are all ignored. In addition, the friction between the lead block and the cover plate is also ignored because the corresponding sliding motion is not significant. Assume the lead block is split along the center line, and stress analysis of the lead block is carried out, as shown in Figure 5. On the basis of the assumption plane-strain, the analytic expression of the normal stress on the center line of the groove is obtained. The specific process is described as follows.

Firstly, the lead blocks in forward compressional stress state are selected as the research object. Since the lead blocks are symmetric and both of lead blocks are spliced in the same direction, their stress diagram is shown in Figure 5. In Figure 6, the lead blocks are divided into six domains according to the flow law of metal in forward compressional stress state, and stress analysis and solution can be carried out for the six domains, respectively.

In Domain I, as shown in Figure 7(a), the antideformation stress of the lead block is assumed as σ_s , which is suggested to be 12.7 MPa [32]. σ_{n1} is the normal stress of lead block interface in Domain I. σ_{n1} approximately equals σ_s . τ_{k1} is the shear stress of lead block interface, μ is friction coefficient, set as 0.15, and τ_{k1} equals $\mu\sigma_s$ according to the friction theorem.

The equation of static equilibrium can be obtained in the horizontal direction, as follows:

$$2\sigma_1 B d_1 = 2\tau_{k1} l_1 B = 2\mu\sigma_s l_1 B. \quad (1)$$

The normal stress on the center line at the end of the Domain I is given by

$$\sigma_1 = \frac{\mu\sigma_s l_1}{d_1}, \quad (2)$$

where d_1 is the thickness of lead block out of groove region and l_1 is the length of lead block in working region.

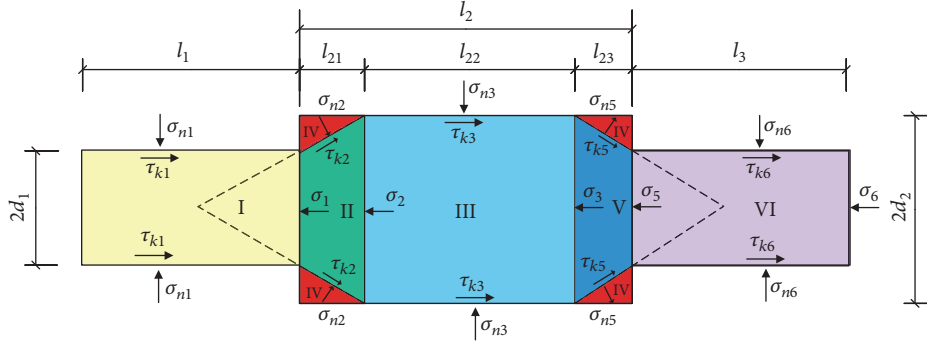


FIGURE 6: Stress diagram of lead in forward compressive state.

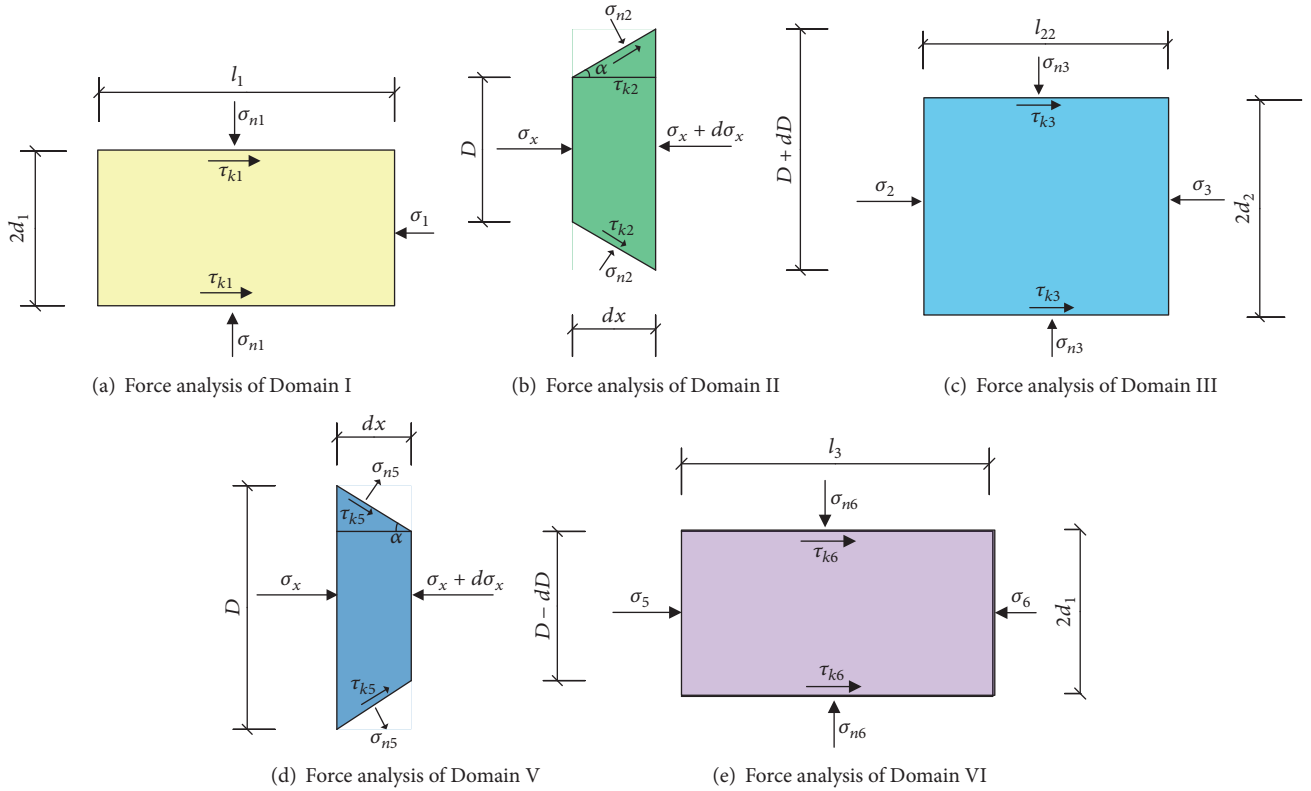


FIGURE 7: Stress analysis of lead in the forward compressive state.

The stress state of Domain II is shown in Figure 7(b). As the Domain IV is static during the reciprocating motion of the lead, the shear failure occurs at the cross section of the Domain II and Domain IV, and the corresponding angle of the horizontal plane is α . Thus, the shear stress reaches the maximum τ_{\max} on the interface between Domain II and Domain IV. If the normal stress of lead block on the interface between Domain II and Domain IV is σ_{n2} , and the corresponding shear stress is τ_{k2} , then $\tau_{k2} = \tau_{\max} = \sigma_s / \sqrt{3}$ can be proved by Von-Mises yield criterion.

The horizontal component of σ_{n2} is

$$T_2 = 2\sigma_{n2} \sin \alpha \cdot \frac{dx}{\cos \alpha} B. \quad (3)$$

The horizontal component of τ_{k2} is

$$T_2' = 2\tau_{k2} B \frac{dx}{\cos \alpha} \cdot \cos \alpha = \frac{2}{\sqrt{3}} \sigma_s B dx. \quad (4)$$

The equation of static equilibrium can be obtained in the horizontal direction of the Domain II as follows:

$$B(\sigma_x + d\sigma_x)(D + dD) - \sigma_x B D - T_2' - T_2 = 0. \quad (5)$$

Consider that the approximate plastic condition $\sigma_{n2} - \sigma_x = \sigma_s$ is acceptable [33], and the geometric relationship $dD = 2 \tan \alpha dx$ is obtained, where α is the dead angle and set as 60° . Eq. (5) is integrated with the boundary condition when

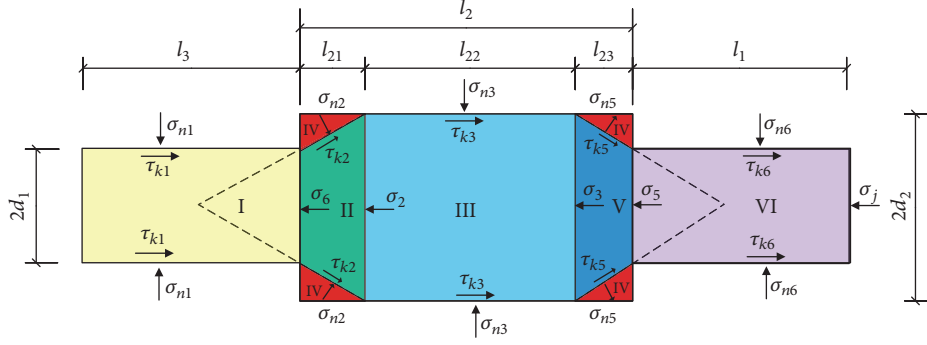


FIGURE 8: Stress diagram of lead in the back forward compressive state.

$D = 2d_1$ and $\sigma_x = \sigma_j$; the normal stress in the center line of Domain II can be obtained

$$\sigma_{2x} = \sigma_s \left[\left(1 + \frac{1}{\sqrt{3} \tan \alpha} \right) \ln \frac{D}{2d_1} + \frac{\mu l_1}{d_1} \right]. \quad (6)$$

If d_2 is the thickness of lead block in groove region and $D = 2d_2$, the normal stress on the center line at the end of Domain II can be obtained by (6), which is expressed as

$$\sigma_2 = \sigma_s \left[\left(1 + \frac{1}{\sqrt{3} \tan \alpha} \right) \ln \frac{d_2}{d_1} + \frac{\mu l_1}{d_1} \right]. \quad (7)$$

In Domain III, as shown in Figure 7(c), the shear stress of the lead block on the upper and lower interfaces is obtained as $\tau_{k3} = \sigma_s / \sqrt{3}$. l_{22} is lead block length in Domain III, and $l_{22} = l_2 - 2(d_2 - d_1) / \tan \alpha$, where l_2 is the length of a single lead groove. The static equilibrium equation in the horizontal direction can be obtained as

$$\sigma_2 \cdot 2d_2 \cdot B + 2\tau_{k3} \cdot l_{22} \cdot B = \sigma_3 \cdot 2d_2 \cdot B. \quad (8)$$

The normal stress on the center line at the end of Domain III can be obtained by (7) and (8) as follows:

$$\sigma_3 = \sigma_s \left[\left(1 + \frac{1}{\sqrt{3} \tan \alpha} \right) \ln \frac{d_2}{d_1} + \frac{\mu l_1}{d_1} + \frac{l_{22}}{\sqrt{3}d_2} \right]. \quad (9)$$

The stress state of Domain V is shown in Figure 7(d); the analysis process is similar to that of Domain II, and the equilibrium equations in the horizontal direction are also established. Finally, the normal stress on the center line at the end of Domain V is obtained as follows:

$$\sigma_5 = \sigma_s \left[2 \left(1 + \frac{1}{\sqrt{3} \tan \alpha} \right) \ln \frac{d_2}{d_1} + \frac{\mu l_1}{d_1} + \frac{l_{22}}{\sqrt{3}d_2} \right]. \quad (10)$$

The stress state of Domain VI is shown in Figure 7(e), the analysis process is similar to that of Domain I, and the normal stress on the center line at the end of Domain V is given by

$$\sigma_6 = \sigma_s \left[2 \left(1 + \frac{1}{\sqrt{3} \tan \alpha} \right) \ln \frac{d_2}{d_1} + \frac{\mu(l_1 + l_3)}{d_1} + \frac{l_{22}}{\sqrt{3}d_2} \right]. \quad (11)$$

Similarly, according to the above method, if the lead blocks on the other side of the center line of groove are regarded as the research object as shown in Figure 8, the normal stress σ_j , which is on the end of the whole lead block, may be expressed as

$$\sigma_j = \sigma_s \left[5 \left(1 + \frac{1}{\sqrt{3} \tan \alpha} \right) \ln \frac{d_2}{d_1} + \frac{\mu(2l_1 + l_3)}{d_1} + \frac{2l_{22}}{\sqrt{3}d_2} \right]. \quad (12)$$

After the normal stress at the end of the whole lead block is obtained by (12), the total yield force P of ILSD-LS is ultimately calculated according to the effective area of the lead block as follows:

$$P = 2\sigma_s \left[5 \left(1 + \frac{1}{\sqrt{3} \tan \alpha} \right) \ln \frac{d_2}{d_1} + \frac{\mu(2l_1 + l_3)}{d_1} + \frac{2l_{22}}{\sqrt{3}d_2} \right] B d_1. \quad (13)$$

For a well-designed lead shear damper, the total yield force is stable and its postyielding stiffness can be ignored due to the small yield displacement, which is usually not greater than 5 mm. Thus, the hysteretic curve of lead damper is generally a standard rectangle, and its mechanical constitutive model is equivalent to an ideal rigid plastic model. Therefore, the mechanical model and the hysteresis curve can be established after the yield force of ILSD-LS is calculated by (13). In the following sections, the correctness and the feasibility of the mechanical model will be verified by numerical simulation and experimental results.

4. Finite Element Simulation and Analysis of ILSD-LS

In order to investigate whether the hysteretic characteristics of ILSD-LS can meet the requirements of large yield force and long stroke for practical engineering, the finite element simulation and analysis of the damper were carried out. The design parameters for ILSD-LS are shown as follows:

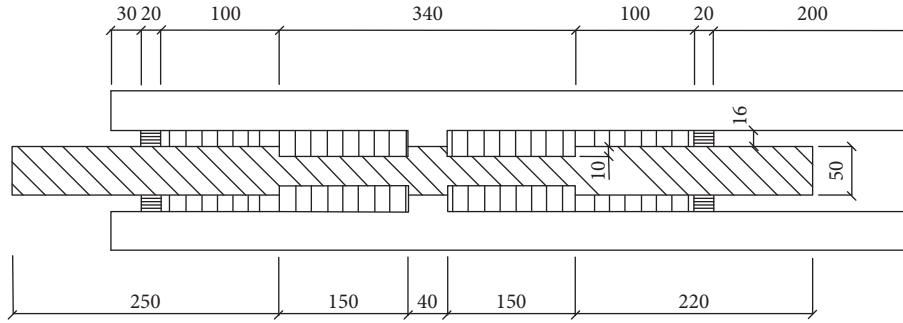


FIGURE 9: Detail drawing of ILSD-LS (Unit: mm).

$B = 200$ mm, $d_1 = 16$ mm, $d_2 = 26$ mm, $l_1 = 100$ mm, $l_2 = 150$ mm, and $l_3 = 40$ mm. The detailed dimensions are shown in Figure 9. According to the ILSD-LS mechanical analysis model based on (13), the theoretical yield force is 946.1 kN.

Finite element (FE) simulation of ILSD-LS was carried out by ABAQUS software to verify the stability of energy dissipation and the yield degree of the lead blocks in the damper. The FE model is established according to the design dimension, as shown in Figure 10, and the following assumptions are used in the simulation:

(1) According to the construction of ILSD-LS, there is no relative movement between the lead block and the cover plate in horizontal and vertical directions, so the lead block is directly imposed consolidation constraint in the FE mode. The deformation of the sliding plate is ignored because the strength of the sliding plate is much greater than that of the lead block, and it is simplified as a discrete rigid body.

(2) In the initial state, there is no gap or contact between the lead block and the sliding plate, and there is also no interaction between the interfaces. The contact action is simulated by rigid-flexible contact method.

(3) The friction between lead and sliding plate is taken into account, and the friction coefficient is set as 0.7 [34]. The maximum frictional stress on the contact surface is 11.5 MPa.

(4) The material property of lead is assumed to be ideal rigid plastic; although the recrystallization process of lead at room temperature cannot be considered in ABAQUS, it can be equivalent to a stress process by choosing a reasonable strength value of lead. The yield strength σ_y of lead metal is selected as 14.0 MPa, the elastic modulus E is 1.646×10^4 MPa, and Poisson's ratio μ is 0.42 according to the statistical analysis of the experimental data of mechanical properties of lead metal. The yield state of lead material in complex stress state is judged by the Mises criterion.

The FE analysis results of ILSD-LS are illustrated in Figure 11. The yield displacement of the damper is 2 mm, the yield force is 1000.21 kN, and the yield force remains essentially the same with the increase of loading displacement.

When the loading displacement is 90 mm, the stress contour of the whole lead block is shown in Figure 12. The results indicate that the stress of lead block is nearly uniform and the energy dissipation is relatively adequate because the whole section has basically reached the stress yielding state,

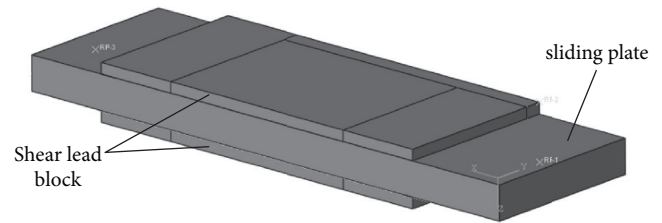


FIGURE 10: Finite element model of ILSD-LS.

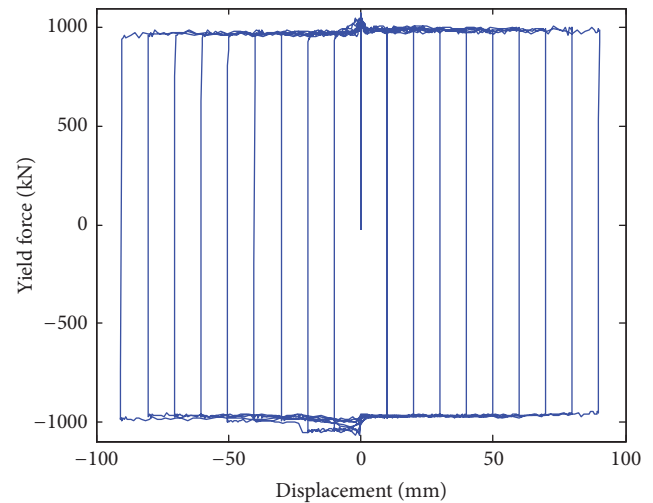


FIGURE 11: Numerical simulation results of ILSD-LS.

so the ILSD-LS can provide a long stroke with satisfactory stability.

In order to verify the consistency between the theoretical results and the simulation results, the axial normal stress at the end of I–VI domains of the FE model is extracted and compared with the theoretical values, which are shown in Figure 13. It reveals that the theoretical and the simulation results are relatively close. The FE results are larger than the theoretical results mainly due to local stress concentration, which leads to the higher overall average stress of the section. In conclusion, the yield force that is directly based on the

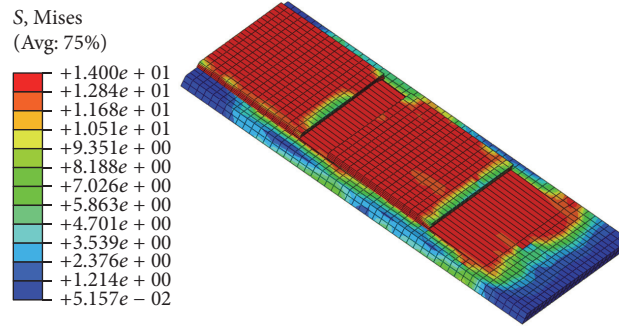


FIGURE 12: Stress nephogram of displacement 90 mm.

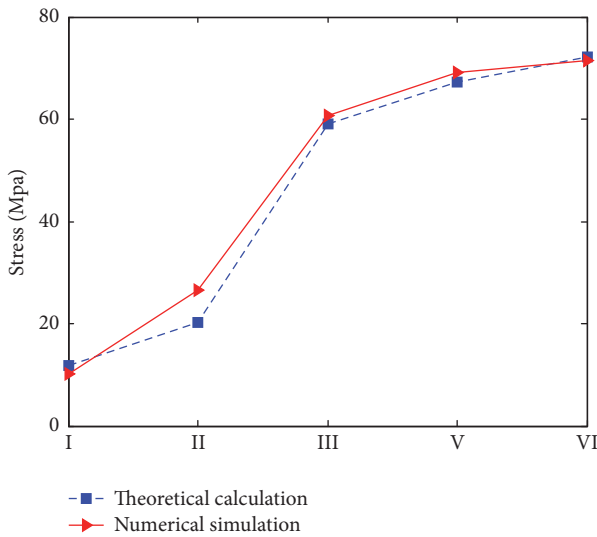


FIGURE 13: Comparison of theoretical and finite element solution of sectional normal stress.

theoretical method of this study basically meets the accuracy requirement of ILSD-LS design.

5. Experimental Study of ILSD-LS and LSD-LS

In order to compare the energy dissipation capacity and the stability between LSD-LS and ILSD-LS, and to further verify the accuracy of the theoretical analysis, one LSD-LS and one ILSD-LS were fabricated. The basic dimensions of both specimens are the same as those shown in Figure 9.

The low cycle reciprocating load experiments are carried out for two specimens, as shown in Figure 14. Among them, the internal structure of the lead block for lead groove of LSD-LS is shown in Figure 14(a), and the lead block is not divided. The internal structure of the lead block for lead groove of ILSD-LS is shown in Figure 14(b), and the lead block is divided into two parts by bars.

The experiments are carried out by using a 3000 kN damper test system, which can operate test on the dynamic performance of the energy dissipation dampers, such as viscous dampers, lead damper and friction damper, and so on. The test specimen is required to be 0.4 m–5 m in length

and its maximum width is 1.5 m. The level of the test system allows the static tension to be 4500 kN, and the operating frequency is 0–20 Hz. In this paper, the specimen is subjected to simple harmonic loading with 0.1 Hz frequency.

The displacement-controlled method is adopted, and the loading history is shown in Figure 15. The displacement and the damping force of the damper are recorded, respectively, with a displacement meter and a force sensor.

The experimental results of the LSD-LS are shown in Figure 16. It can be seen that the yield force is inadequate under small displacement. As the loading displacement gradually increases, the yield force also increases, and the hysteresis curve appears a concave shape. It indicates that the energy consumption of the shearing block lead is insufficient and does not yield completely. As the displacement increases, local compaction state appears in the lead block near the side baffle, and the pressure between the lead block and the cover plate could increase; then the yield force increases. When the displacement reaches 60 mm, the yield force progressively deteriorates with the numbers of loading cycle increase.

The experimental results of the ILSD-LS are shown in Figure 17. It can be found out that the hysteresis curve no longer shows a concave shape, which indicates that the shearing lead block has reached the yield state under small displacement and the stress is homogeneous. During the loading process, the yield force of the ILSD-LS approximately remains about 1000 kN, which is larger than that of LSD-LS. When the displacement is 90 mm, the degradation degree of yield force is not significant with the increasing numbers of loading cycles.

According to (13), the theoretical yield force of the ILSD-LS is 946 kN. Four types of results are obtained and comparatively analyzed: the experimental result of LSD-LS at the displacement of 60 mm, the simulation results of ILSD-LS at the displacement of 90 mm, and the experimental results of ILSD-LS at the displacements of 60 mm and 90 mm, respectively, as shown in Figure 18. It can be seen that the energy dissipation capacity of LSD-LS is significantly lower than that of ILSD-LS because the relative shear lead block length of LSD-LS is longer and the damping efficiency is not high. In addition, the yield force of ILSD-LS is as large as 66.6% of the yield force of LSD-LS, and the energy dissipation of ILSD-LS is more stable. The experimental results, simulation results, and theoretical calculations of

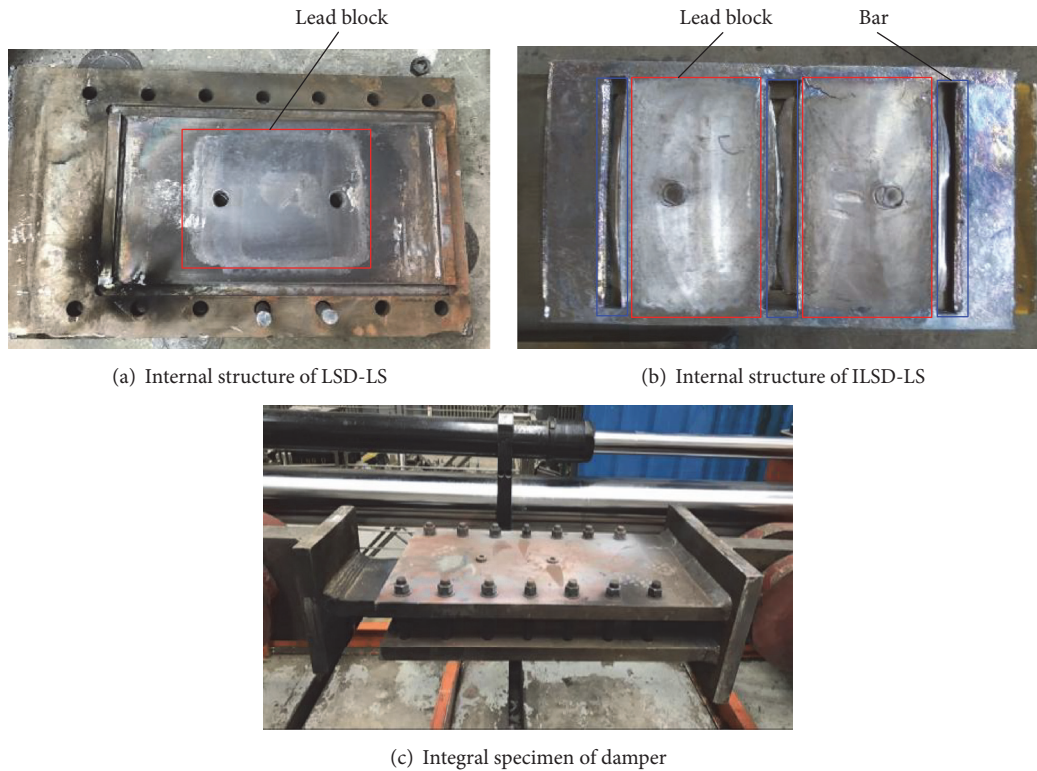


FIGURE 14: Experiment of LSD-LS.

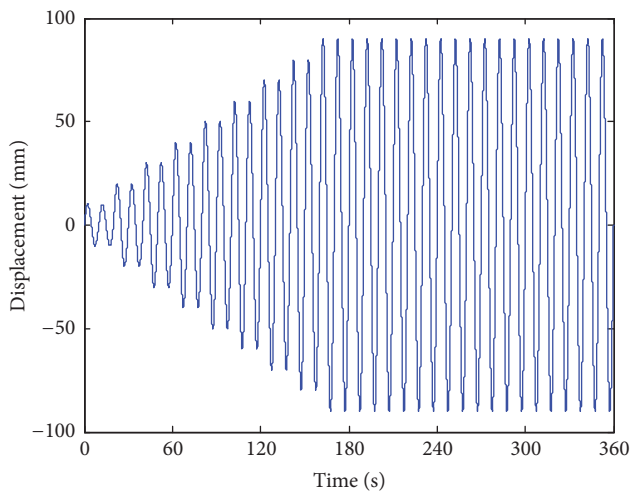


FIGURE 15: Loading history.

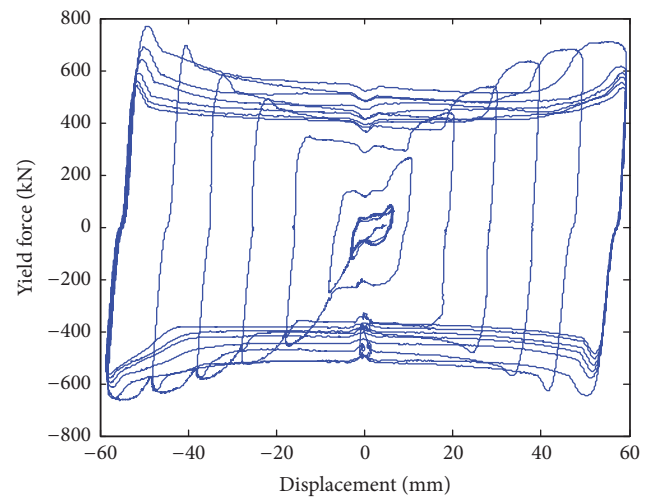


FIGURE 16: Experiment result of LSD-LS.

ILSD-LS are in good agreement, and the difference among the three is not more than 6%.

Taking into account the above analysis results, it can be concluded that ILSD-LS can meet the requirements of long stroke and large yield force, and its damping efficiency and stability are better than those of LSD-LS.

The above theoretical analysis, FE simulation, and experiment about ILSD-LS show that its energy dissipation performance is stable and excellent, and the following section

is analyses of the control effects of a high-rise building with ILSD-LS under the action of actual ground motion.

6. Case Analysis

To verify the damping capacity of ILSD-LS on the seismic response of high-rise buildings subjected to normal ground motions and long-period ground motions, a reinforced concrete (RC) frame structure is selected as a typical case,

TABLE 1: Information of recorded ground motions.

Event	Station	Number	Time	Magnitude	Peak acceleration (cm/s ²)	Duration (s)
Borrego Mtn	San Onofre-SoCal Edison	T1	1968	6.6	46.30	45.20
Kern County	LA-Hollywood Stor FF	T2	1952	7.4	57.80	70.00
Imperial Valley-06	Calipatria Fire Station	T3	1979	6.5	126.22	39.63
Chi-Chi_ Taiwan-03	CHY078	T4	1999	6.2	17.15	59.00
Chi-Chi_ Taiwan	CHY054	T5	1999	7.6	93.00	77.60
Chi-Chi_ Taiwan-03	CHY107	T6	1999	6.2	45.59	90.00

and numerical analysis is carried out. The structure has 15 stories with a total height of 60 m. The RC beam section is rectangular and the dimension is 1000 mm × 700 mm, the elastic modulus of the concrete is 3.0×10^4 N/mm², the axial compressive strength is 14.3 N/mm², and the axial tensile strength is 1.43 N/mm². The RC column section is also rectangular, and the dimension is 900 mm × 900 mm, the elastic modulus of the concrete is 3.15×10^4 N/mm², the axial compressive strength is 16.7 N/mm², and the axial tensile strength is 1.57 N/mm². The RC plate thickness is 100 mm, and the elastic modulus is 3.0×10^4 N/mm², axial compressive strength is 14.3 N/mm², and axial tensile strength is 1.43 N/mm². The gravity loads used in the design are represented by dead- and live-loads, equal to 2.0 kN/m² and 2.5 kN/m², respectively. The site type is soft rock and the seismic precautionary intensity is 8.0, which means the structure may suffer from the earthquake whose exceeding probability of this intensity is 10% in the 50 year period, and the basic seismic acceleration value is 0.15 g. The fundamental period of the RC frame is 1.55 s. In order to enhance the structural safety, diagonal steel braces equipped with ILSD-LSs are installed on the high-rise structure. According to the dynamic characteristics of the structure, the performance parameters of the damper are as follows: the yield force is 1000 kN, the stroke is 90 mm, and the initial stiffness is 8.0×10^5 kN/m. Moreover, the properties of the ILSD-LS are assumed as the same for each story, including yield force and initial stiffness, which may be relatively low damping efficient, and the upper stories have greater stiffness than the lower stories. However, the typical RC frame structure does not have any adverse effects during earthquakes after installing ILSD-LSs, and the more optimal method for damper design and installation can consult the corresponding study by Ponzo et al. [35, 36].

In order to avoid structural eccentricity and weak stories, and considering the energy dissipation efficiency of the dampers, the ILSD-LSs are arranged along the four corners of the structure, and 8 dampers are installed for each story; thus, the total number of ILSD-LSs is 120. The elastic-plastic structural model is established in SAP2000, as shown in Figure 19, in which the beam and column are modeled by beam-column element, and the ILSD-LS is simulated by

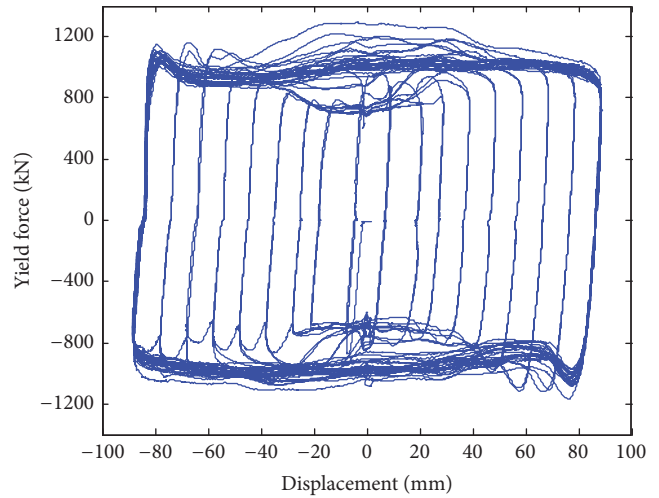


FIGURE 17: Experiment result of ILSD-LS.

LINK elements, and the LINK element setting property is plastic (Wen) model. On this basis, the nonlinear dynamic time history analysis considering single-dimensional ground motions is carried out.

In this study, in order to investigate the influence of long-period ground motion on the response of dampers and structure, and the technical requirements of ILSD-LS, 6 natural ground motion records are selected, and the specific information is shown in Table 1. In accordance with the code for seismic design of buildings in China, the peak acceleration of all the waves is adjusted to 400 cm/s², and the corresponding acceleration response spectra are shown in Figure 20. The six waves are input along the long-axis direction; then the structural elastic-plastic time history analysis is carried out.

By analyzing the structural dynamic responses, it indicates that the interstory drifts of the structure under long-period ground motions are obviously larger than that of the normal ground motions. When the uncontrolled structure is subjected to long-period ground motions, the maximum interstory drift can reach 72.6 mm. Since the biggest interstory drift usually occurs on the fourth story, the corresponding results that are interstory drift and acceleration of this

TABLE 2: Peak damping ratio of different ground motions (%).

Wave number	T1	T2	T3	T4	T5	T6
Interstory drift angle	36.27	36.21	34.14	45.35	42.92	41.08
Peak acceleration	0.32	-4.13	-8.5	-1.05	-4.66	0.68
Base shear force	0.27	1.01	23.71	6.18	26.78	6.46

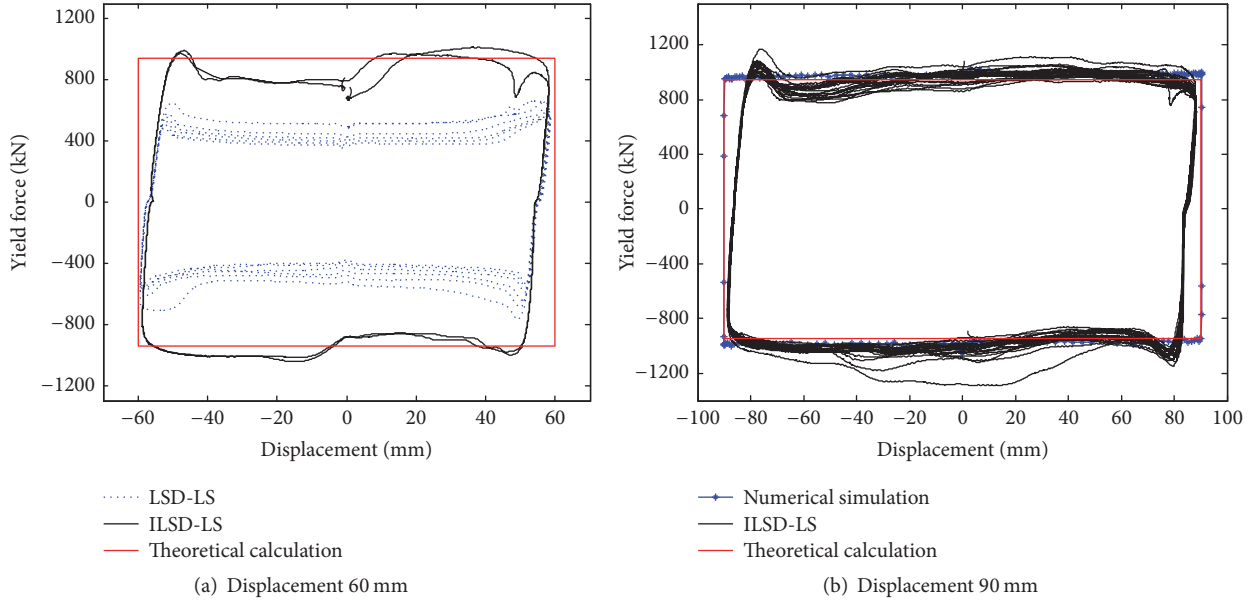


FIGURE 18: Comparison of hysteretic curves with different displacement amplitude.

story before and after control is chosen and compared, and the responses under wave T1 and wave T4 are shown in Figures 21 and 22, respectively. The results show that ILSD-LS can effectively reduce the story drift. In contrast, the stroke of ordinary lead shear damper usually cannot be reached more than 40 mm, though the stroke of LSD-LS may meet the basic requirements; however, its energy dissipation capacity is insufficient. Hence, the superior damping effect as ILSD-LS cannot be obtained if the ordinary dampers or LSD-LSs are adopted.

To further discuss the effect of ground motion on the seismic response of the structure with ILSD-LS, the damping ratio of peak interstory drift angle is calculated, as listed in Table 2. The typical interstory drift angle before and after control is shown in Figure 23. The damping effect of the dampers is obvious so the damping capacity of ILSD-LS for the overall response of the high-rise structure is further verified.

In addition, the damping effect of peak acceleration is also compared and analyzed, and the results are shown in Table 2. The typical contrast results are shown in Figure 24. The partial peak acceleration value increases after installing dampers because ILSD-LS provides additional stiffness to the structure. As a result, the structural periods slightly decrease and the seismic reaction increases. In view of amplification of acceleration being insignificant and the damping effect

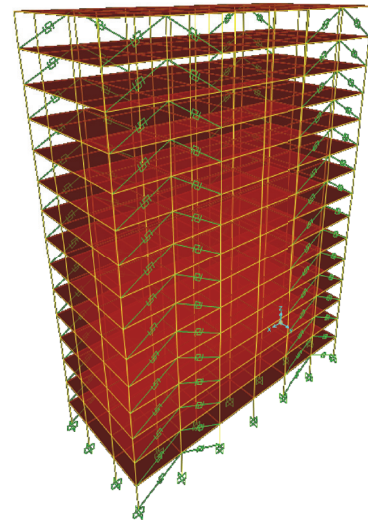


FIGURE 19: Finite element analysis model.

of displacement being obvious, the corresponding adverse effects can be accepted.

Furthermore, the damping ratio of different stories is diverse. The damping effect of the top story is the worst because the interstory drift is smaller and the ILSD-LS does

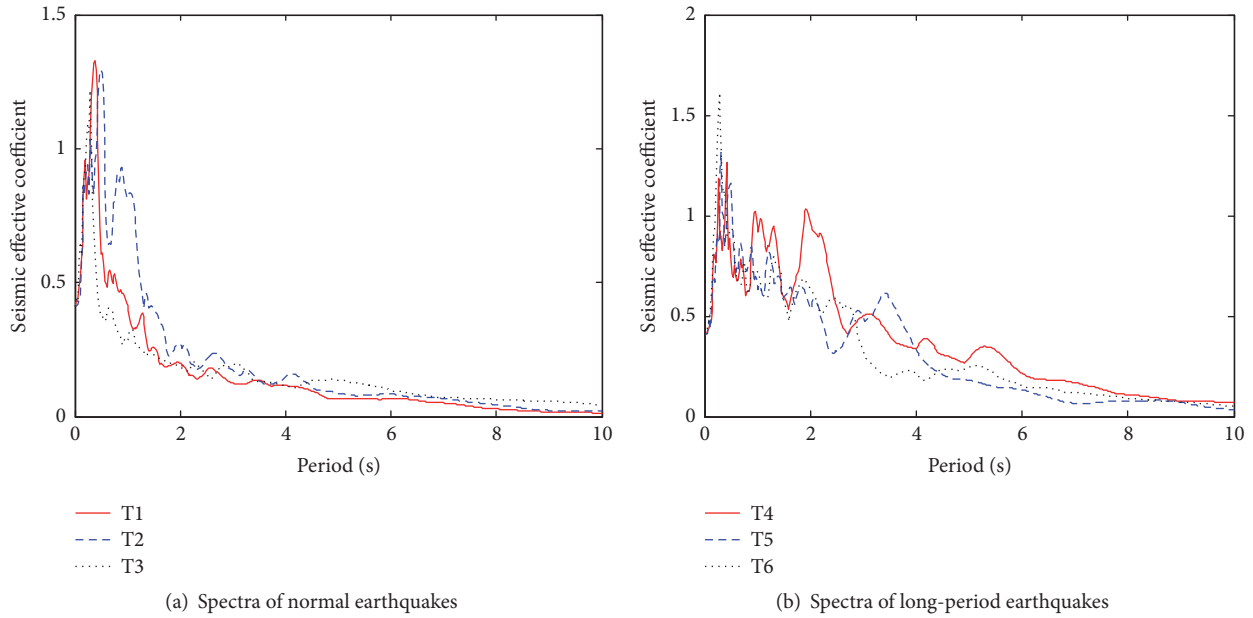


FIGURE 20: Acceleration response spectra.

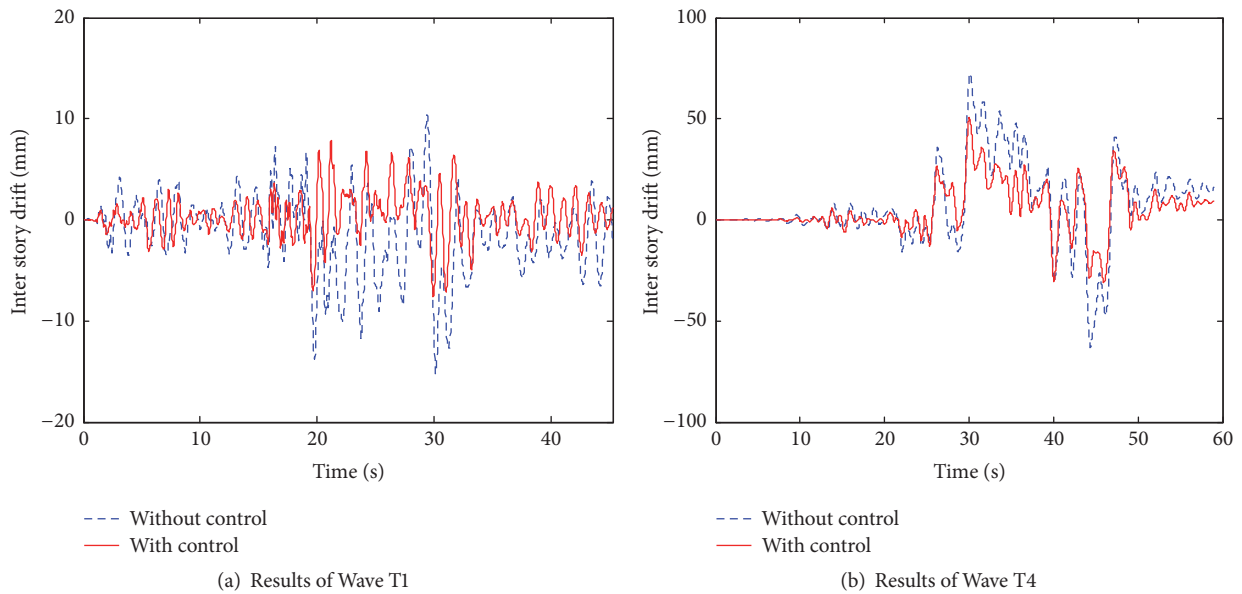


FIGURE 21: Interstory drift time history of different earthquakes.

not reach yield stage, so the kinetic energy is not necessarily dissipated and the damper provides only lateral stiffness.

In addition, the base shear force that is the shear of the bottom of the first story columns of the structure with or without control is compared, as shown in Figure 25. The damping effect of base shear force is also compared and analyzed, and the results are shown in Table 2. The results show that the force of the main body of the structure is obviously decreased, and the structural safety is improved. The hysteretic curves of ILSD-LS under the action of ground motion are shown in Figure 26; the results indicate that the damping capacity of the damper is excellent, and the long

stroke adequately meets the requirement for the long-period ground motions.

In order to further represent the ductility demand for the RC members to better enlighten the effectiveness of the ILSD-LSs, the hysteretic curves of the typical column at the bottom are compared without and with control under Wave T3, as shown in Figure 27, where the displacement refers to the displacement of the top of the column relative to the bottom, and the shear force refers to the shear force at the top of the column. The columns located between two diagonal braces with ILSD-LSs at first, fourth, and seventh stories are selected. The hysteretic curves of column of the first story

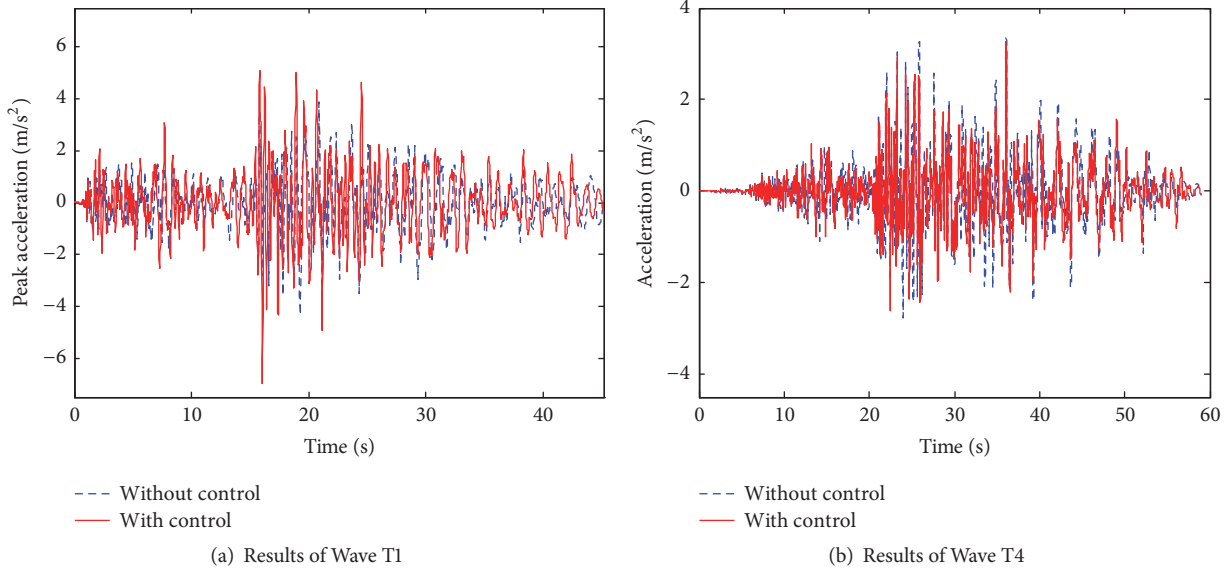


FIGURE 22: Acceleration time history of different earthquakes.

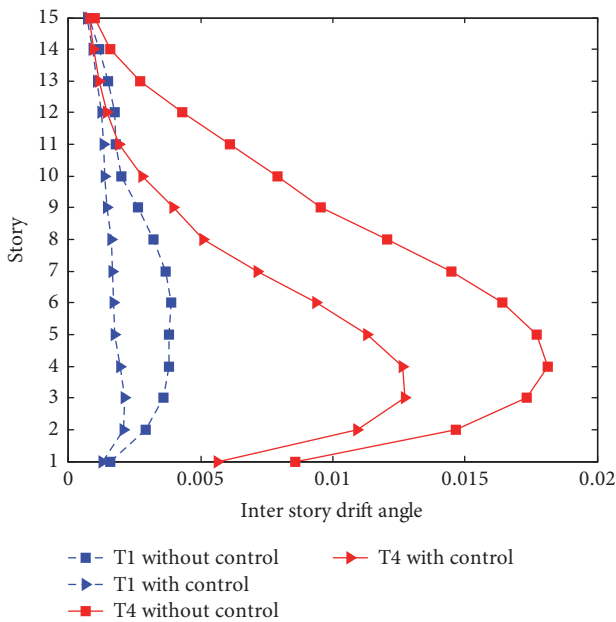


FIGURE 23: Interstory drift angle for different ground motions.

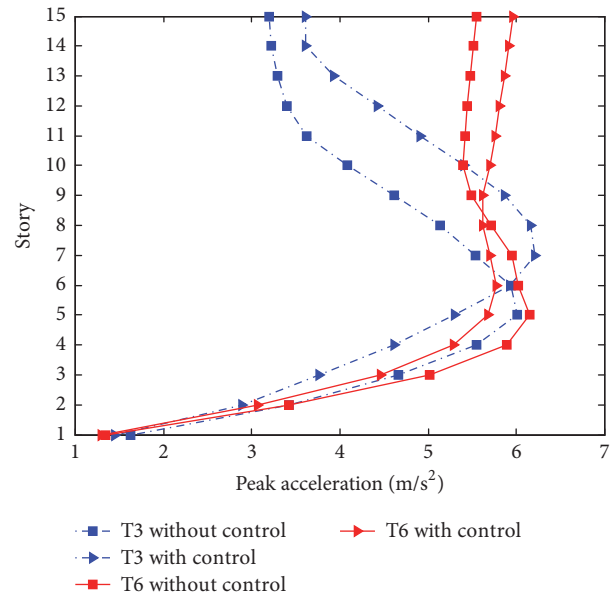


FIGURE 24: Peak acceleration before and after control.

are shown in Figure 27(a), and the maximum displacement without or with control is 6.24 mm or 5.11 mm, respectively. The hysteretic curves of column of the fourth story are shown in Figure 27(b); the maximum displacement without or with control is 15.22 mm or 7.66 mm, respectively. The hysteretic curves of column of the seventh story are shown in Figure 27(c), and the maximum displacement without or with control is 14.7 mm or 6.71 mm, respectively. The results show that the ductility demand and seismic performance of the original RC frame structural members are also improved.

The above results prove that ILSD-LS is effective in decreasing the seismic response of the high-rise buildings.

Although the structural responses under long-period ground motions are significantly greater than those of normal ground motions, the damping effect of the structure under the long-period ground motions is better because ILSD-LS has the advantages of long stroke, adequate energy dissipation, and good stability.

7. Conclusions

In this study, in order to reduce large deformation of the high-rise building structure which is subjected to far-field earthquake with long-period components, an improved lead shear damper of large stroke (ILSD-LS) is presented, and

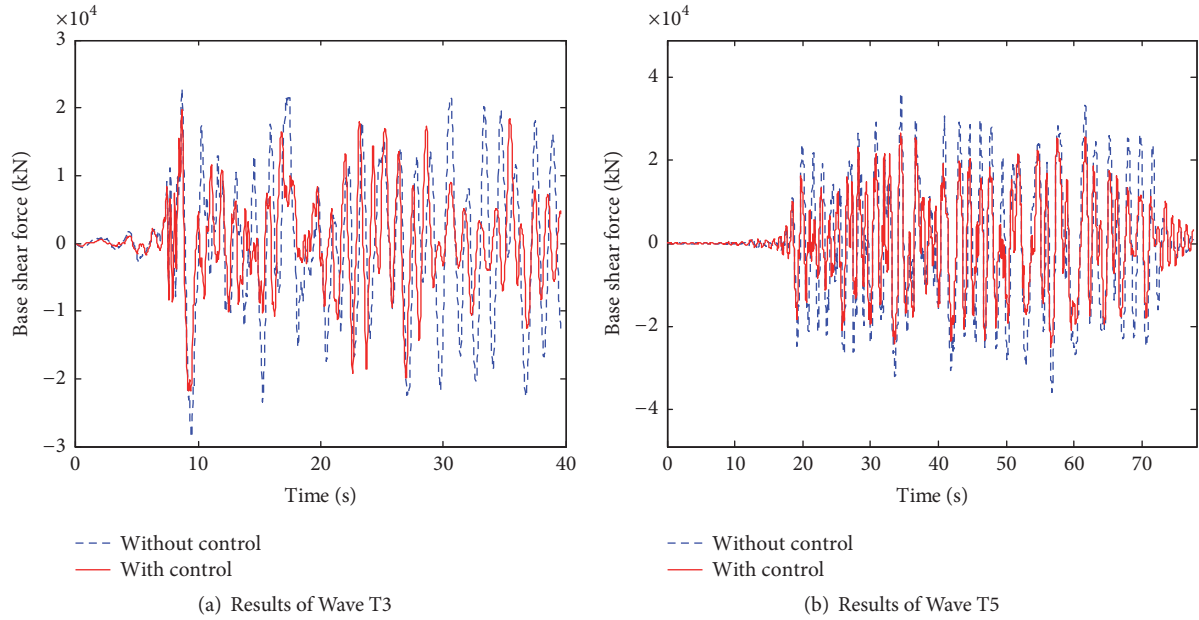


FIGURE 25: Base shear force time history of different ground motions.

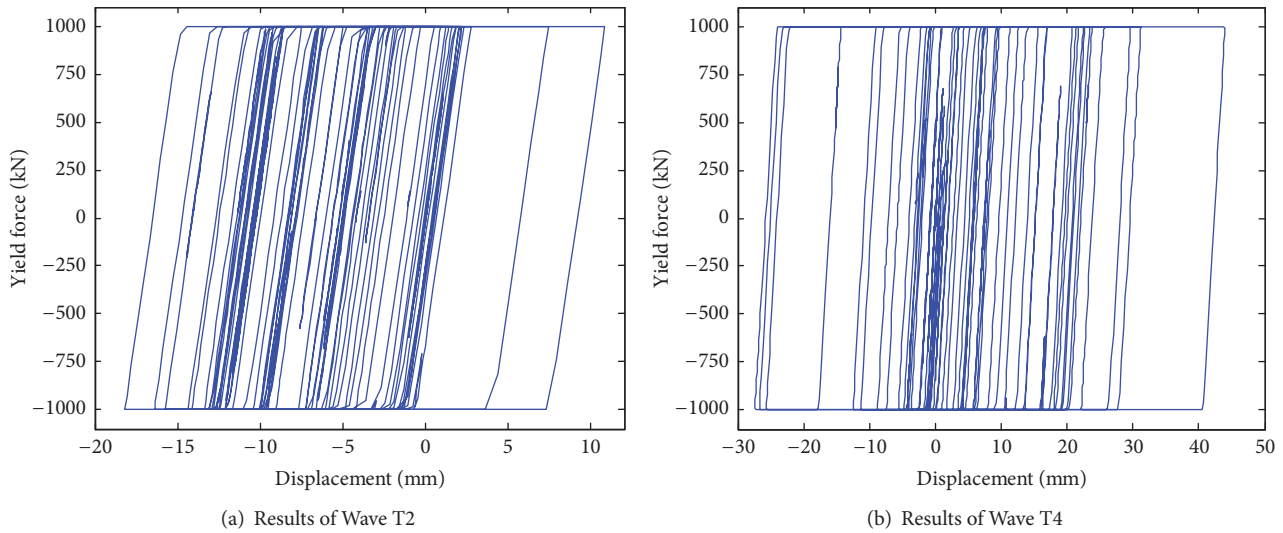


FIGURE 26: Hysteretic curves of ILSD-LS of different ground motions.

the mechanical structure of the damper is introduced. The theoretical analytic solutions, numerical simulation, and experimental research on the mechanical model of the ILSD-LS are carried out. Finally, the damper is applied to a high-rise building subjected to ground motions and the corresponding dynamic time history analysis is carried out. The results show that the energy dissipation capacity of ILSD-LS is stable and fine. The ILSD-LSs can effectively control the deformation and reduce the damage of the high-rise building structure especially for long-period earthquakes, and their beneficial effects can be improved proportioning them by some optimal design procedure according to a corresponding study [35, 36]. The main conclusions are obtained as follows:

- (1) Based on the ideal rigid-plastic constitutive law of lead, considering the extrusion effect of the bars on the sliding plate, a mechanical model of the ILSD-LS is established, and the damping force formula is proposed and its correctness is verified.
- (2) With contrast experiments on the LSD-LS and the ILSD-LS, it is evident that the energy dissipation capacity and the stability of the ILSD-LS are better, which could meet the requirements for stroke and yield force.
- (3) Taking an actual reinforced concrete frame as an analysis example, the nonlinear time analysis is carried out, and the effects of normal and long-period ground motions are considered. The numerical results indicate that dynamic

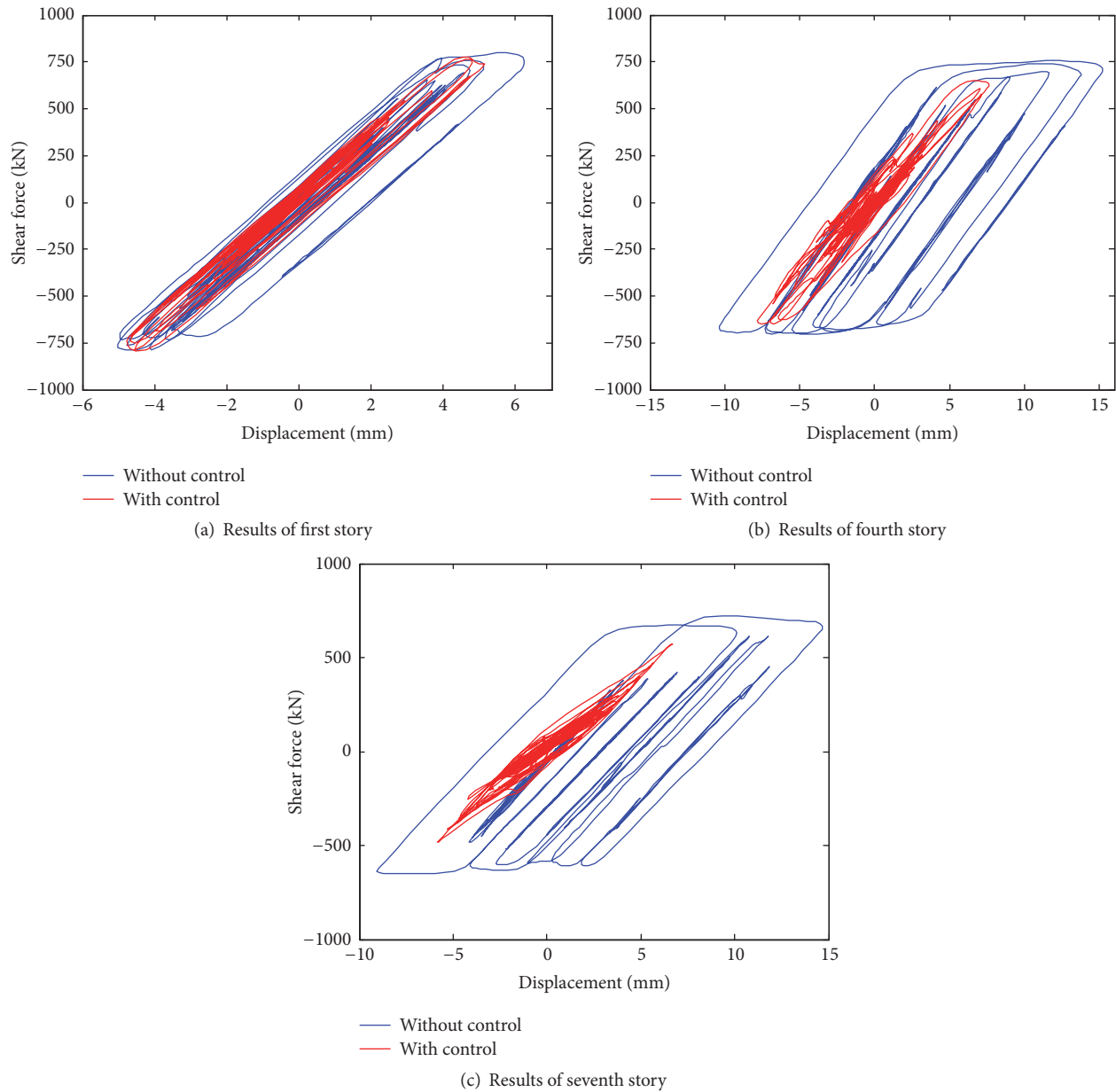


FIGURE 27: The hysteretic curves of the typical column.

responses of the high-rise structure with ILSD-LS significantly decrease, even when the structure is subjected to long-period ground motion.

Although the damping effect of ILSD-LS has been verified, the dampers are installed on all stories for structural nonlinear analysis in this study, so the cost-benefit ratio is higher. For the complex structures with uneven story stiffness or eccentric structure, how to select the effective control index to optimize the damping parameters and installation location of ILSD-LS still needs to be studied.

Conflicts of Interest

The authors declare that there are no conflicts of interest regarding the publication of this paper.

Acknowledgments

This work is partially supported by Natural Science Foundation of China under Grant nos. 51378039, 51421005, 51478024, and 91315301-03.

References

- [1] T. Ariga, Y. Kanno, and I. Takewaki, "Resonant behaviour of base-isolated high-rise buildings under long-period ground motions," *The Structural Design of Tall and Special Buildings*, vol. 15, no. 3, pp. 325–338, 2006.
- [2] D. Kim and J. Kim, "Experimental Study on the Structural Performance of Hybrid Friction Damper," *Journal of the Korean Association for Spatial Structures*, vol. 15, no. 3, pp. 103–110, 2015.

- [3] I. H. Mualla and B. Belev, "Performance of steel frames with a new friction damper device under earthquake excitation," *Engineering Structures*, vol. 24, no. 3, pp. 365–371, 2002.
- [4] K.-W. Min, J.-Y. Seong, and J. Kim, "Simple design procedure of a friction damper for reducing seismic responses of a single-story structure," *Engineering Structures*, vol. 32, no. 11, pp. 3539–3547, 2010.
- [5] R.-H. Zhang, T. T. Soong, and P. Mahmoodi, "Seismic response of steel frame structures with added viscoelastic dampers," *Earthquake Engineering & Structural Dynamics*, vol. 18, no. 3, pp. 389–396, 1989.
- [6] Z. Pawlak and R. Lewandowski, "The continuation method for the eigenvalue problem of structures with viscoelastic dampers," *Computers & Structures*, vol. 125, pp. 53–61, 2013.
- [7] J.-D. Kang and H. Tagawa, "Seismic response of steel structures with seesaw systems using viscoelastic dampers," *Earthquake Engineering & Structural Dynamics*, vol. 42, no. 5, pp. 779–794, 2013.
- [8] A. D. E. Pan and N. Yeung, "Wind tunnel experiments of a building model incorporating viscous-damping walls," *Wind and Structures, An International Journal*, vol. 4, no. 3, pp. 261–276, 2001.
- [9] C. A. Martínez, O. Curadelli, and M. E. Compagnoni, "Optimal design of passive viscous damping systems for buildings under seismic excitation," *Journal of Constructional Steel Research*, vol. 90, pp. 253–264, 2013.
- [10] E. Tubaldi, L. Ragni, and A. Dall'Asta, "Probabilistic seismic response assessment of linear systems equipped with nonlinear viscous dampers," *Earthquake Engineering & Structural Dynamics*, vol. 44, no. 1, pp. 101–120, 2015.
- [11] C. Zhang, Z. Zhang, and J. Shi, "Development of high deformation capacity low yield strength steel shear panel damper," *Journal of Constructional Steel Research*, vol. 75, pp. 116–130, 2012.
- [12] S. Maleki and S. Bagheri, "Pipe damper, Part I: Experimental and analytical study," *Journal of Constructional Steel Research*, vol. 66, no. 8–9, pp. 1088–1095, 2010.
- [13] R. W. K. Chan and F. Albermani, "Experimental study of steel slit damper for passive energy dissipation," *Engineering Structures*, vol. 30, no. 4, pp. 1058–1066, 2008.
- [14] K. Ghabraie, R. Chan, X. Huang, and Y. M. Xie, "Shape optimization of metallic yielding devices for passive mitigation of seismic energy," *Engineering Structures*, vol. 32, no. 8, pp. 2258–2267, 2010.
- [15] E. Matta, "Effectiveness of tuned mass dampers against ground motion pulses," *Journal of Structural Engineering (United States)*, vol. 139, no. 2, pp. 188–198, 2013.
- [16] K. Tarbali and F. Nateghi-A, "Effect of structural uncertainty on seismic response of steel moment-resisting frames equipped with tuned mass dampers," *International Journal of Steel Structures*, vol. 14, no. 2, pp. 231–241, 2014.
- [17] A. Lucchini, R. Greco, G. C. Marano, and G. Monti, "Robust design of tuned mass damper systems for seismic protection of multistory buildings," *Journal of Structural Engineering (United States)*, vol. 140, no. 8, Article ID A4014009, 2014.
- [18] Y. Chen, D. M. McFarland, Z. Wang, B. F. Spencer Jr., and L. A. Bergman, "Analysis of tall buildings with damped outriggers," *Journal of Structural Engineering*, vol. 136, no. 11, pp. 1435–1443, 2010.
- [19] Y. M. Parulekar, G. R. Reddy, K. K. Vaze, and H. S. Kushwaha, "Lead extrusion dampers for reducing seismic response of coolant channel assembly," *Nuclear Engineering and Design*, vol. 227, no. 2, pp. 175–183, 2004.
- [20] C. S. Tsai, W. S. Lai, C. W. Chang, and M. C. Li, "Testing and analysis of a new lead-extrusion damper," in *Proceedings of the Seismic Engineering -2002- (2002 ASME Pressure Vessels and Piping Conference)*, pp. 215–220, Canada, August 2002.
- [21] D. Zhou, W. Yan, Y. Chen, and C. Liu, "Seismic analysis of a low tower cable-stayed bridge and application of lead shear damper," *Applied Mechanics and Materials*, vol. 90–93, pp. 1715–1719, 2011.
- [22] R. O. Curadelli and J. D. Riera, "Design and testing of a lead damper for seismic applications," *Proceedings of the Institution of Mechanical Engineers, Part C: Journal of Mechanical Engineering Science*, vol. 221, no. 2, pp. 159–165, 2007.
- [23] G. W. Rodgers, J. G. Chase, J. B. Mander, N. C. Leach, and C. S. Denmead, "Experimental development, tradeoff analysis and design implementation of high force-to-volume damping technology," *Bulletin of the New Zealand Society for Earthquake Engineering*, vol. 40, no. 2, pp. 35–48, 2007.
- [24] W. H. Robinson and L. R. Greenbank, "An extrusion energy absorber suitable for the protection of structures during an earthquake," *Earthquake Engineering & Structural Dynamics*, vol. 4, no. 3, pp. 251–259, 1976.
- [25] M. D. Monti and W. H. Robinson, "A lead shear damper suitable for reducing the motion induced by wind and earthquake," in *Proceedings of the II WCEE*, vol. 271, p. 271, Mexico, Acapulco, Mexico.
- [26] Y. Q. Ni, H. J. Liu, and J. M. Ko, "Experimental investigation on seismic response control of adjacent buildings using semi-active MR dampers," in *Proceedings of the Smart Structures and Materials 2002: Smart Systems for Bridges, Structures, and Highways*, pp. 334–344, USA, March 2002.
- [27] S. Behrens, A. J. Fleming, and S. O. Reza Moheimani, "Electromagnetic shunt damping," in *Proceedings of the 2003 IEEE/ASME International Conference on Advanced Intelligent Mechatronics, AIM 2003*, pp. 1145–1150, Japan, July 2003.
- [28] X. Zhou and L. Peng, "A new type of damper with friction-variable characteristics," *Earthquake Engineering and Engineering Vibration*, vol. 8, no. 4, pp. 507–520, 2010.
- [29] K. Minagawa, S. Fujita, T. Kawamura, and G. Tanaka, "Seismic response analysis of industrial building with viscous-friction hybrid damper," in *Proceedings of the ASME 2013 Pressure Vessels and Piping Conference, PVP 2013*, France, July 2013.
- [30] A. M. Sharabash and B. O. Andrawes, "Application of shape memory alloy dampers in the seismic control of cable-stayed bridges," *Engineering Structures*, vol. 31, no. 2, pp. 607–616, 2009.
- [31] X. Shen, X. Wang, Q. Ye, and A. Ye, "Seismic performance of Transverse Steel Damper seismic system for long span bridges," *Engineering Structures*, vol. 141, pp. 14–28, 2017.
- [32] D. Zhou, *Study on Seismic Performance of Long-Span Girder Bridges Considering Soil and Structure Interaction*, Beijing University of Technology, 2012.
- [33] J. L. Wen, H. Ding, and F. R. Cao, *Extrusion and Drawing Technology for Non-Ferrous Metals*, chemical industry press, Beijing, China, 2007.
- [34] L. Y. Peng, W. M. Yan, and H. X. He, "Finite element analysis and testing of plate type shear lead damper," *Journal of Vibration and Shock*, vol. 29, no. 1, pp. 183–189, 2010.

- [35] F. C. Ponzo, A. Di Cesare, D. Nigro et al., “Jet-pacs project: dynamic experimental tests and numerical results obtained for a steel frame equipped with hysteretic damped chevron braces,” *Journal of Earthquake Engineering*, vol. 16, no. 5, pp. 662–685, 2012.
- [36] A. Di Cesare and F. C. Ponzo, “Seismic retrofit of reinforced concrete frame buildings with hysteretic bracing systems: design procedure and behaviour factor,” *Shock and Vibration*, vol. 2017, Article ID 2639361, 20 pages, 2017.

Research Article

Adaptive Gain Scheduled Semiactive Vibration Control Using a Neural Network

Kazuhiko Hiramoto ¹, Taichi Matsuoka,² and Katsuaki Sunakoda³

¹Mechanical Engineering Program, Niigata University, Niigata 950-2181, Japan

²Department of Mechanical Engineering Informatics, Meiji University, Kawasaki 214-8571, Japan

³Akita University, Akita 010-8502, Japan

Correspondence should be addressed to Kazuhiko Hiramoto; hiramoto@eng.niigata-u.ac.jp

Received 21 August 2017; Revised 25 October 2017; Accepted 4 December 2017; Published 15 January 2018

Academic Editor: Oren Lavan

Copyright © 2018 Kazuhiko Hiramoto et al. This is an open access article distributed under the Creative Commons Attribution License, which permits unrestricted use, distribution, and reproduction in any medium, provided the original work is properly cited.

We propose an adaptive gain scheduled semiactive control method using an artificial neural network for structural systems subject to earthquake disturbance. In order to design a semiactive control system with high control performance against earthquakes with different time and/or frequency properties, multiple semiactive control laws with high performance for each of multiple earthquake disturbances are scheduled with an adaptive manner. Each semiactive control law to be scheduled is designed based on the output emulation approach that has been proposed by the authors. As the adaptive gain scheduling mechanism, we introduce an artificial neural network (ANN). Input signals of the ANN are the measured earthquake disturbance itself, for example, the acceleration, velocity, and displacement. The output of the ANN is the parameter for the scheduling of multiple semiactive control laws each of which has been optimized for a single disturbance. Parameters such as weight and bias in the ANN are optimized by the genetic algorithm (GA). The proposed design method is applied to semiactive control design of a base-isolated building with a semiactive damper. With simulation study, the proposed adaptive gain scheduling method realizes control performance exceeding single semiactive control optimizing the average of the control performance subject to various earthquake disturbances.

1. Introduction

Semiactive vibration control of structural systems with ER, MR dampers, or variable stiffness device, and so on can realize control performance exceeding the passive control, that is, structural modification including the addition of tuned mass dampers to the main structural system. Moreover, semiactive control is simple, has low energy consumption, and is safe against failure of the control element compared to active control that is realized by sensors, a (feedback) controller, and actuators requiring a large power supply. Because of the above advantages, semiactive control has been actively studied as a vibration control method for structural systems subject to large-scale earthquake disturbances in which surrounding power failure can be occurred [1–5].

One of the most important specifications that the semiactive control system should satisfy is that the designed semiactive control law has high control performance against

future unknown seismic disturbances. In order to satisfy the specification, design parameters in the semiactive control law are optimized to achieve good control performance against recorded and/or artificial earthquake disturbances having various time and frequency characteristics. In designing a single time-invariant control law that does not depend on the disturbance characteristics, the semiactive control system is necessary to realize the averagely good control performance on vibration suppression for earthquake disturbances with various time and frequency characteristics. It means that the semiactive control law must satisfy the performance robustness with respect to the variation of the earthquake disturbance and the realizable control performance of the single semiactive control law is limited because of the performance robustness itself.

To overcome such a situation, if we can adaptively change the semiactive control law depending on the characteristics of the earthquake disturbance, higher control performance

than that of the single control law described above, that is, the single control law optimizing the control performance on average for all disturbances, is expected to be realized. As an example of the adaptive change, the following method can be considered:

- (1) We firstly design multiple control laws for seismic disturbances with some different properties. Each of the semiactive control laws is designed to maximize control performance only for a single disturbance with a specific property.
- (2) For the future unknown earthquake disturbance, the best semiactive control law is selected from or interpolated with the multiple semiactive control laws designed in the previous step. The selection or interpolation is determined based on available sensor data, for example, the earthquake disturbance.

Regarding the characteristic analysis of earthquake disturbance, many methodologies in the time and/or frequency domain have been proposed from the viewpoint of seismology. However, we cannot determine what kind of characteristics of the earthquake wave should be considered as a reference for selecting the most appropriate semiactive control law from multiple candidates of the control law (or interpolating multiple semiactive control laws) to obtain the good control performance.

In this study, we adopt an artificial neural network (ANN) as an approach to make appropriate selection or interpolation of the above-mentioned multiple semiactive control laws. Artificial neural networks have been widely used for pattern recognition, modeling, and control system design during some decades [6]. Recently, along with the development of techniques such as deep learning, the application of the neural network to artificial intelligence has become actively studied. In this paper, we design an ANN with an input of a measured earthquake disturbance and an output of parameters to schedule multiple semiactive control laws with different properties. Parameters in the ANN, for example, weighting and bias, are optimized so that the ANN can be used as a good adaptive gain scheduler to interpolate multiple semiactive control laws from earthquake disturbance information. We demonstrate the effectiveness of the proposed method by simulation using the adaptive gain scheduled semiactive control law with the ANN-based scheduling mechanism.

The rest of the paper is organized as follows. In Section 2, a structural model with semiactive control devices is defined. In Section 3, the detail of the methodology of the gain scheduled semiactive control system composed of the multiple semiactive control laws and the ANN-based scheduler are described. The simulation study is given in Section 4 and the conclusion of the study is shown in Section 5.

2. Structural Model

The control object in the study is a n -DOF structural system that has n_s semiactive control devices whose damping coefficients can be changed with command signals shown in

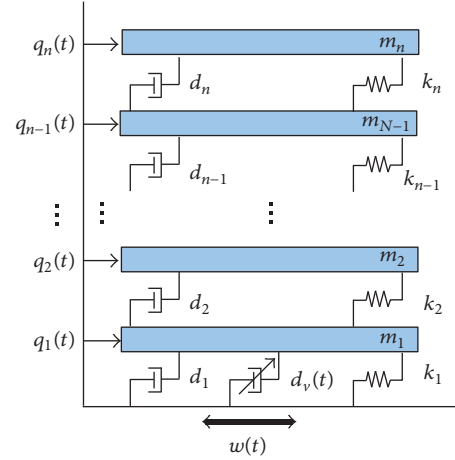


FIGURE 1: n -DOF structural system with n_s semiactive dampers.

Figure 1. The equation of motion and the state-space form of the control object are given as follows:

$$M\ddot{q}(t) + \left(D_0 + \sum_{j=1}^{n_s} d_j^s(t) D_j^s \right) \dot{q}(t) + Kq(t) = Gw(t) + \left(H_0 + \sum_{j=1}^{n_s} d_j^s(t) H_j^s \right) \dot{w}(t) \quad (1)$$

$$q(t) = [q_1(t) \ q_2(t) \ \cdots \ q_n(t)]^T, \quad (2)$$

where $q_i(t)$, $i = 1, \dots, n$, and $w(t)$ are the absolute displacement of i -th mass (floor) and the earthquake disturbance, respectively. Matrices $M = M^T > 0$, $D_0 = D_0^T > 0$, and $K = K^T > 0$ are the structural mass, damping, and stiffness matrices, respectively. Matrices G and H_0 are the influence coefficient matrices.

The state-space model of the structural system defined in (1) is given by

$$\dot{x}(t) = \left(A_0 + \sum_{j=1}^{n_s} d_j^s(t) A_j^s \right) x(t) + \left(B_0 + \sum_{j=1}^{n_s} d_j^s(t) B_j^s \right) v(t) \quad (3)$$

$$z(t) = C_z x(t) + D_z v(t)$$

$$y(t) = C_y x(t) + D_y v(t),$$

$$x(t) = [q^T(t) \ \dot{q}^T(t)]^T,$$

$$v(t) = [w(t) \ \dot{w}(t)]^T,$$

$$A_0 = \begin{bmatrix} 0_{n \times n} & I_n \\ -M^{-1}K & -M^{-1}D_0 \end{bmatrix},$$

$$\begin{aligned}
A_j^s &= \begin{bmatrix} 0_{n \times 2n} \\ 0_{n \times n} & -M^{-1}D_j^s \end{bmatrix}, \quad j = 1, \dots, n_s, \\
B_0 &= \begin{bmatrix} 0_{n \times 2} \\ M^{-1}G & M^{-1}H_0 \end{bmatrix}, \\
B_j^s &= \begin{bmatrix} 0_{n \times 2} \\ 0_{n \times n} & M^{-1}H_j^s \end{bmatrix}, \quad j = 1, \dots, n_s,
\end{aligned} \tag{4}$$

where $z(t)$ and $y(t)$ are the controlled output for the performance evaluation and the measurement vector obtained with sensors installed on the structural system.

The variable damping coefficient of the j th semiactive damper $\bar{d}_j^s(t)$ is varied in a range given as follows:

$$0 \leq \underline{d}_j^s \leq \bar{d}_j^s(t) \leq \overline{d}_j^s, \quad j = 1, \dots, n_s, \tag{5}$$

where \overline{d}_j^s and \underline{d}_j^s are the maximum and minimum values of the variable damping coefficient of the j th semiactive damper, respectively.

Moreover, there exists a dynamic delay in the damping coefficient of the semiactive damper for its command signal. The characteristics of the dynamic delay are modeled as follows:

$$\begin{aligned}
\dot{x}_j^s(t) &= -\frac{1}{T_j^s} x_j^s(t) + \frac{1}{T_j^s} d_j^c(t) \\
d_j^s(t) &= s_j(x_j^s(t)), \\
j &= 1, \dots, n_s,
\end{aligned} \tag{6}$$

where T_j^s and $d_j^c(t)$, $j = 1, \dots, n_s$, are the time constant and the command signal of the j th semiactive damper, respectively. The function $s_j(\cdot)$, $j = 1, \dots, n_s$, is a saturation function defined as

$$s_j(x_j^s) = \begin{cases} \overline{d}_j^s & (x_j^s \geq \overline{d}_j^s) \\ x_j^s & (\underline{d}_j^s < x_j^s < \overline{d}_j^s) \\ \underline{d}_j^s & (x_j^s \leq \underline{d}_j^s), \end{cases} \quad j = 1, \dots, n_s. \tag{7}$$

3. Control System Design

3.1. Adaptive Gain Scheduling. It is well-known that seismic waves have common characteristics to some extent in time and frequency domain [7, 8]. On the other hand, there are many different characteristics between seismic waves. The difference is due to many factors such as the mechanism of the earthquake, the distance between the seismic center and the controlled structural system, and the propagation path of the seismic wave.

Generally, structural vibration control systems subject to earthquakes are designed in consideration of the commonality of the above frequency characteristics. In other

words, if the vibration control law is designed so as to exhibit good control performance against typical disturbance, then, from the commonality point of view, the control system is expected to achieve good control performance for unknown earthquake disturbances including future seismic events.

However, it is also a fact that the achievable performance of the vibration control system changes depending on characteristics of the earthquake disturbance. For example, when a vibration control system that optimizes the design parameters so as to exert good control performance for the disturbance A receives a disturbance B that is different in time and frequency characteristics from the disturbance A, the performance of the control system is not necessarily equivalent to that exerted against disturbance A.

In order to deal with the performance variation of the control system, the design parameters of the control law for determining the control characteristics are optimized for multiple recorded and/or artificial earthquakes (that are used as test disturbance signals for the simulation of the control system) so that the control performance becomes good on average in the general design process of the vibration control system. This concept can be referred to as a robust performance concept for various characteristics of earthquake disturbance. However, taking a robust performance approach, control performance against the individual earthquake tends to be limited due to the robust performance property of the control law itself.

Remark 1. In control community, the concept of the robust performance is dealt with more mathematically with the notion of the structured singular value of the closed-loop system [9]. However, the authors dare to use the term ‘‘robust performance’’ here because the control design for multiple disturbance aims at the robust performance of the control system from the practical viewpoint.

Contrary to the robust performance approach described above, a method that achieves optimum control performance by adaptively scheduling multiple control laws can be considered. Each of the control laws in the approach has been obtained in advance so as to have high control performance against a specific earthquake disturbance. Because this control concept does not require consideration of the robust performance specifications, further improvement in control performance can be expected.

In this study, we propose a mechanism to adaptively schedule multiple semiactive control laws with different control characteristics based on information such as earthquake disturbance obtained from sensors. The block diagram of the control system is shown in Figure 2, where P , C_k , $k = 1, \dots, n_c$, are the structural system to be controlled and a semiactive control law with high control performance against a specific earthquake disturbance, respectively. The input to C_k , $k = 1, \dots, n_c$, is the structural response $y(t)$ obtained from the sensor, and the output is the command signal of the semiactive damper denoted by a vector $u_k^c = [(d_1^c)_k \cdots (d_{n_s}^c)_k]^T$, $k = 1, \dots, n_c$, where j -th element of the vector u_k^c is the command signal to change the variable

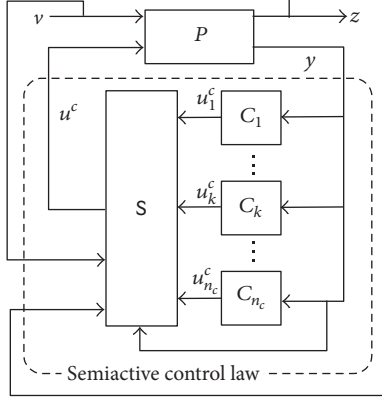


FIGURE 2: Block diagram of the adaptive gain scheduling semiactive control system with $C_k, k = 1, \dots, n_c$, and the scheduling mechanism S.

damping coefficient $d_j^s(t), j = 1, \dots, n_s$ (defined in (6)), by the k th semiactive control law C_k . The block S is an adaptive gain scheduling mechanism that determines the most appropriate selection or interpolation of all $u_k^c(t)$'s generated by n_c semiactive control laws $C_k, k = 1, \dots, n_c$, at the time instant t . The scheduled command signal of n_s semiactive dampers is defined as $u^c = [d_1^c \dots d_{n_s}^c]^T$. In principle, the adaptive scheduling mechanism S can utilize sensor information used by the semiactive control law and command signal $u^c(t)$ itself.

In the next two subsections, we describe the detail of the design method of the feedback control law C_k and the adaptive scheduling mechanism, the block S in Figure 2.

3.2. Design of the Semiactive Control Law C_k . The semiactive control law $C_k, k = 1, \dots, n_c$, in the previous subsection is designed to achieve high control performance against a specific single earthquake disturbance. The block diagram for designing the semiactive control law $C_k, k = 1, \dots, n_c$, is shown in Figure 3, where $v_k, k = 1, \dots, n_c$, is the specific single earthquake disturbance considered during the design of the semiactive control law C_k . The adjustable design parameters in the semiactive control law C_k are optimized so that the closed-loop system consisting of the control object P and the semiactive control law C_k exhibits high control performance under the earthquake disturbance v_k .

In this study, the semiactive control law C_k is designed using the output emulation approach [5] recently proposed by the authors. In the output emulation method, the command signal of the variable damping coefficient of the semiactive damper is switched between the maximum and minimum values. The switching criterion is the error between the predicted controlled outputs of the semiactive control and reference active systems. In the following, the detail of the output emulation approach will be described in detail.

The reference active control system can be obtained by replacing the semiactive dampers of the control object in (3) with force actuators. The reference active control system is a virtual system that cannot be realized in the present situation

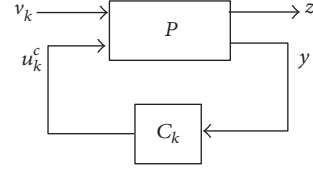


FIGURE 3: Block diagram of the control system for the synthesis of the semiactive control law C_k .

but is used as the performance target of the semiactive control system. The state-space form of the reference active control system is defined as follows:

$$\begin{aligned} \dot{x}_a(t) &= A_0 x_a(t) + B_0 v(t) + B_a u^a(t) \\ z_a(t) &= C_z x_a(t) + D_z v(t) \end{aligned} \quad (8)$$

$$y(t) = C_y x_a(t) + D_y v(t),$$

$$x_a(t) = [q^T(t) \quad \dot{q}^T(t)]^T, \quad (9)$$

$$v(t) = [w(t) \quad \dot{w}(t)]^T,$$

where $x_a(t)$ and $u^a(t) = [u_1^a(t) \dots u_{n_s}^a(t)]^T$ are the state vector and the control force vector of the reference active control system, respectively. Note that the controlled output $z_a(t)$ of the reference active control system has the same components as those of $z(t)$ of the control object in (3).

In this study, we assume the state vector $x_a(t)$ is available with sensors; that is, the measured output in (8) is $y(t) = x_a(t)$. Under the assumption, we define the reference active control law as a state-feedback given by

$$u_a(t) = -K_a x_a(t), \quad (10)$$

where K_a is the state-feedback gain matrix of the reference active control law. The closed-loop system with the reference active control system in (8) and the state-feedback control law in (10) becomes

$$\begin{aligned} \dot{x}_a(t) &= A_c x_c(t) + B_0 v(t) \\ z_a(t) &= C_z x_c(t) + D_z v(t), \end{aligned} \quad (11)$$

$$A_c = A_0 - B_a K_a.$$

In the output emulation approach, the command signal to change the variable damping coefficient of the semiactive damper is changed with a measure of the closeness of the controlled output between the semiactive and reference active control systems. The closeness between the semiactive and reference active control systems is evaluated by using the predicted controlled output of two systems. The detail of the process to obtain the command signal of the semiactive damper in the output emulation approach is described below.

Let t_0 and $\Delta t > 0$ be the current time and the small prediction length, respectively. From (11), the predicted control output of the reference active control is given as

$$z_a(t_0 + \Delta t) = C_z x_a(t_0 + \Delta t) + D_z v(t_0 + \Delta t). \quad (12)$$

The predicted value of the disturbance vector at $t = t_0 + \Delta t$ can be approximately obtained by

$$\begin{aligned} v(t_0 + \Delta t) &\approx v(t_0) + \Delta t \dot{v}(t_0) \\ &= \begin{bmatrix} \dot{w}(t_0) \\ w(t_0) \end{bmatrix} + \Delta t \begin{bmatrix} \ddot{w}(t_0) \\ \dot{w}(t_0) \end{bmatrix}. \end{aligned} \quad (13)$$

Similarly the predicted state vector of the reference active control system at $t = t_0 + \Delta t$ is approximately given as follows:

$$x_a(t_0 + \Delta t) \approx x_a(t_0) + \Delta t \dot{x}_a(t_0). \quad (14)$$

With (11), we have the time derivative of $x_c(t)$ at $t = t_0$ as

$$\dot{x}_a(t_0) = A_c x_a(t_0) + B_0 v(t_0). \quad (15)$$

In order to get $\dot{x}_a(t_0)$, we can adopt numerically stable integration methods such as the Runge-Kutta method and Newmark's β method. The predicted control output vector $z_a(t_0 + \Delta t)$ of the reference active control system can be obtained by (12)–(15). With the continuing measurement of $x_a(t_0)$ and $v(t_0)$, we can obtain the predicted output signal of the reference active control system.

Similarly, we can obtain the predicted control output of the semiactive system. The predicted control output of the semiactive system $z(t_0 + \Delta t)$ is given as

$$z(t_0 + \Delta t) = Cx(t_0 + \Delta t) + Dv(t_0 + \Delta t). \quad (16)$$

The predicted value of the disturbance vector $v(t_0 + \Delta t)$ can be obtained with (13). The predicted state vector of the semiactive control system is given as

$$x(t_0 + \Delta t) \approx x(t_0) + \Delta t \dot{x}(t_0). \quad (17)$$

With (3), (5), and (6), the time derivative of the state vector of the j th semiactive control system at $t = t_0$ is obtained as follows:

$$\begin{aligned} \dot{x}_j^s(t_0) &= -\frac{1}{T_j^s} x_j^s(t_0) + \frac{1}{T_j^s} d_j^c(t_0) \\ d_j^s(t_0) &= s_j(x_j^s(t_0)), \quad j = 1, \dots, n_s, \\ \dot{x}(t_0) &= \left(A_0 + \sum_{j=1}^{n_s} d_j^s(t_0) A_j^s \right) x(t_0) \\ &\quad + \left(B_0 + \sum_{j=1}^{n_s} d_j^s(t_0) B_j^s \right) v(t_0). \end{aligned} \quad (18)$$

When we fix all the command signals of the semiactive damper at $t = t_0$, we can obtain $\dot{x}(t_0)$. As the candidates of the command signal of the semiactive damper at $t = t_0$, we assume the maximum and minimum values of the variable damping coefficient of the semiactive damper given as follows:

$$d_j^c(t_0) = \begin{cases} \overline{d}_v^j & \\ \underline{d}_v^j & \end{cases} \quad j = 1, \dots, n_s. \quad (19)$$

For all possible command signal combinations, we can calculate the predicted control output of the semiactive control system at $t = t_0 + \Delta t$ with (13) and (16)–(18). For the bang-bang type command signal in (19), the number of n_s command signals' combinations is 2^{n_s} .

In the output emulation approach, the command signal of the j th semiactive damper at $t = t_0$ is selected from 2^{n_s} combinations of command signals (shown in (19)) in real time as follows:

$$d_j^c(t_0) = \underset{d_j^{c(t_0)} = \overline{d}_j^c \text{ or } \underline{d}_j^c}{\operatorname{argmin}} J_e(t_0), \quad (20)$$

$$J_e = \|z_a(t_0 + \Delta t) - z(t_0 + \Delta t)\|, \quad j = 1, \dots, n_s.$$

Remark 2. In the present study, the state vector in (3) is composed of the absolute displacement and velocity of each floor. In conventional modeling of the civil structural system subject to earthquake disturbance, the state vector is defined as the relative displacement and velocity between each floor and ground motion given by

$$x_c = \begin{bmatrix} q(t) - \mathbf{1}w(t) \\ \dot{q}(t) - \mathbf{1}\dot{w}(t) \end{bmatrix}, \quad \mathbf{1} = \underbrace{[1 \cdots 1]}_n^T. \quad (21)$$

In this case, the disturbance is defined as $\ddot{w}(t)$, the acceleration of the earthquake wave. In the output emulation approach, predicted values of disturbance velocity and displacement are obtained by using (13) in order to obtain the predicted value of the controlled output $z(t_0 + \Delta t)$. In general, earthquake waves are often measured by an acceleration sensor. The velocity and displacement of the disturbance can be obtained by performing numerical integration of sensor measurement $\ddot{w}(t)$. Then, in the state-space model of the present study, the predicted disturbance signal $v(t_0 + \Delta t)$ is obtained. On the other hand, if the output emulation method is applied to the conventional model whose disturbance term is defined as the acceleration, the jerk which is the time derivative of the acceleration is required in order to obtain the predicted value of the disturbance in a similar way to that of (13). The numerical differentiation of the measured disturbance acceleration is sometimes not appropriate because it may be contaminated with the sensor noise in the higher-frequency range. Therefore, the state-space form as (3) is employed in this study.

Moreover, the predicted controlled output signals in (12) and (16) are the 1st-order approximation of the Taylor series expansion of $z_a(t_0 + \Delta t)$ and $z(t_0 + \Delta t)$. In the ideal noise-free situation, higher order time derivative terms of the disturbance signal, for example, $d^3 w(t)/dt^3$ and $d^4 w(t)/dt^4$, work to improve the accuracy of the approximation of $z_a(t_0 + \Delta t)$ and $z(t_0 + \Delta t)$. However, it is not necessarily true in the real situation because of the sensor noise problem shown in the above paragraph. This is the reason why the 1st-order approximation of the controlled output is used.

In the output emulation approach, the characteristics of closed-loop reference active control system in (11) are adjusted to optimize the control performance of the semiactive control system. In this study, we adopt the state-feedback

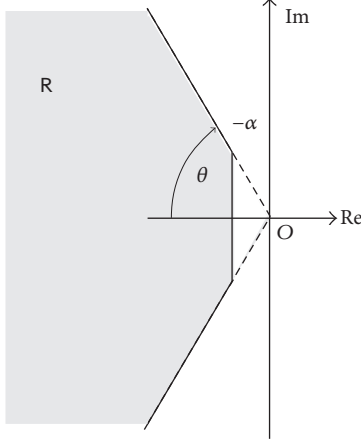


FIGURE 4: Region R in the complex plane.

gain matrix K_a of the reference active control law in (10) so that the closed-loop poles locate in a region R in the complex plane shown in Figure 4 with the method of [10]. By changing constants α and θ , we can change the dynamic characteristics

of the closed-loop reference active control system because the region where eigenvalues of the matrix $A_c = A_0 - B_a K_a$ lie in the complex plane is changed. For example, the larger the constant $\alpha > 0$ constraining the real part of the closed-loop pole, the larger the expected damping of each mode of vibration because the underdamped pole of the i th mode of vibration is given as the follows:

$$p_i = -\zeta_i \omega_i \pm j \sqrt{1 - \zeta_i^2} \omega_i, \quad i = 1, \dots, n, \quad j = \sqrt{-1}, \quad (22)$$

where p_i , ζ_i , and ω_i are the pole, the damping ratio, and the undamped natural frequency of the i th mode of vibration, respectively. Moreover, from the expression in (22), α and $\theta > 0$ also constrain the value of the (undamped) natural frequencies ω_i , $i = 1, \dots, n$, of the reference active control system as the imaginary part of the pole.

The state-feedback gain matrix K_a satisfying the above closed-loop pole constraints can be obtained with the LMI (Linear Matrix Inequality) based method [10]. All poles of the closed-loop reference active control system lie in the region R if $X = X^T > 0$ exists satisfying matrix inequalities as follows:

$$\begin{aligned} A_c X + X A_c^T + 2\alpha X &= (A_0 - B_a K_a) X + X (A_0 - B_a K_a)^T + 2\alpha X < 0. \\ \begin{bmatrix} \sin \theta (A_c X + X A_c^T) & \cos \theta (A_c X - X A_c^T) \\ \cos \theta (X A_c^T - A_c X) & \sin \theta (A_c X + X A_c^T) \end{bmatrix} & \\ = \begin{bmatrix} \sin \theta \{(A_0 - B_a K_a) X + X (A_0 - B_a K_a)^T\} & \cos \theta \{(A_0 - B_a K_a) X - X (A_0 - B_a K_a)^T\} \\ \cos \theta \{X (A_0 - B_a K_a)^T - (A_0 - B_a K_a) X\} & \sin \theta \{(A_0 - B_a K_a) X + X (A_0 - B_a K_a)^T\} \end{bmatrix} < 0 \end{aligned} \quad (23)$$

With the change of variable $W = K_a X$, (23) become LMIs on $X = X^T > 0$ and W given as follows:

$$\begin{aligned} A_0 X + X A_0^T - B_a W - W^T B_a^T + 2\alpha X &< 0, \\ \begin{bmatrix} \sin \theta (A_0 X + X A_0^T - B_a W - W^T B_a^T) & \cos \theta (A_0 X - X A_0^T + W^T B_a^T - B_a W) \\ \cos \theta (X A_0^T - A_0 X + B_a W - W^T B_a^T) & \sin \theta (A_0 X - B_a W + X A_0^T - W^T B_a^T) \end{bmatrix} < 0. \end{aligned} \quad (24)$$

Once matrices $X = X^T$ and W are found, the state-feedback gain matrix K_a that places the closed-loop poles in the region R is given by

$$K_a = W X^{-1}. \quad (25)$$

The reference active control law in the output emulation approach is designed with the LMI-based method shown above. We define $\alpha > 0$ and $\theta > 0$ as design parameters to change the characteristics of the closed-loop reference active control system.

For the specific earthquake disturbance v_k , $k = 1, \dots, n_c$, the characteristics of the reference active control law are adjusted so that the control performance of the semiactive control system based on the output emulation approach is optimized. Two design parameters, α and θ , that shape the region R are optimized so that the semiactive control system based on the output emulation approach has the best control performance for the earthquake disturbance v_k . The reference active control law for the semiactive control law C_k is defined as follows:

$$u_k^{\text{ra}}(t) = -K_k x_a(t), \quad k = 1, \dots, n_c, \quad (26)$$

where $u_k^{\text{ra}}(t)$ and K_k , $k = 1, \dots, n_c$, are the active control input of the reference active control system and the state-feedback gain matrix of the k th semiactive control law C_k . The state-feedback gain matrix K_k is obtained so that the semiactive control system with P and C_k in Figure 3 achieves the best control performance for the k th earthquake disturbance v_k .

In the design of the reference active control law, the parameter α enables adjusting the damping characteristic of the reference active control system and the parameter θ indirectly assigns the mode frequency of the control system. The physical meaning of the two parameters in vibration control of structural systems is clear. Furthermore, the reference active control that satisfies the pole placement constraints is formulated as the LMI problem (in (24)) that is efficiently solvable [10].

In obtaining the predictive controlled output, it is possible to use the discrete-time representation of the structural systems. In the discrete-time setting, the required amount of computation to obtain the predicted controlled output becomes smaller than that of the continuous time setting adopted in the present study. However, when we assume that the reference active control system is designed under the discrete-time setting, it is difficult to define a few design parameters that can easily understand the control characteristics like the above continuous time case because the stable region becomes the inside of a unit circle in a complex plane. Furthermore, the method for obtaining the discrete-time reference active control law satisfying the damping and mode frequency constraints have not been established to date as far as the authors know. Therefore, in this study, we designed the control system under the continuous time setting which facilitates the design of the optimum reference active control law.

Remark 3. In obtaining the optimal reference semiactive control in (26) for the earthquake disturbance v_k , $k = 1, \dots, n_c$, we can adopt any indices if they properly represent the performance on vibration suppression of the semiactive control system subject to the disturbance v_k , for example, the quadratic performance index employed in the LQ optimal control and the peak value of the power spectrum density of the specific output signal subject to the disturbance v_k . The optimal design parameters of the reference active control system, α and θ , are obtained to optimize the performance index obtained with the structural response of the semiactive control system (subject to the disturbance v_k) based on the output emulation approach.

3.3. Design of the Adaptive Scheduling Mechanism. Design method for the adaptive scheduling mechanism of n_c semiactive control laws C_k , $k = 1, \dots, n_c$, is described in the following.

The adaptive scheduling is performed by interpolating the reference active control law used in the n_c semiactive control laws obtained in the previous section. For example, when $n_c = 2$, that is, we have two semiactive control laws C_1 and C_2 , the

interpolated reference active control input $u_I^{\text{ra}}(t)$ is defined as follows:

$$\begin{aligned} u_I^{\text{ra}}(t) &= \beta_1(t) u_1^{\text{ra}}(t) + \{1 - \beta_1(t)\} u_2^{\text{ra}}(t) \\ &= -[\beta_1(t) K_1 + \{1 - \beta_1(t)\} K_2] x_a(t), \end{aligned} \quad (27)$$

where $0 \leq \beta_1(t) \leq 1$ is the parameter for the interpolation. The number of the interpolation parameters is $n_c - 1$. The adaptive scheduling mechanism S in the block diagram in Figure 2 outputs the interpolation parameters $\beta_l(t)$, $l = 1, \dots, n_c - 1$, with the information on the earthquake disturbance $v(t)$, the controlled output signal $z(t)$, and available other signals. The interpolated reference active control input $u_I^{\text{ra}}(t)$ is a convex combination of the n_c reference active control input $u_k^{\text{ra}}(t)$, $k = 1, \dots, n_c$. In this study, with the interpolated reference active control $u_I^{\text{ra}}(t)$, the command signal of the semiactive control device denoted by u^c in Figure 2 is obtained with the output emulation approach described in the previous subsection.

Recall that each of the input signals of the reference active control system denoted by $u_k^{\text{ra}}(t)$, $k = 1, \dots, n_c$, is obtained to achieve the best control performance only for the k th earthquake disturbance. For the earthquake disturbance (with unknown time and frequency characteristics) that occurs in the future, we can expect that the semiactive control law based on the interpolated reference active control input shows the good control performance if the semiactive control laws C_k , $k = 1, \dots, n_c$, are designed for the recorded and/or artificial earthquake disturbances with a wide variety of the time and frequency characteristics and the interpolation parameters $0 \leq \beta_l(t) \leq 1$, $l = 1, \dots, n_c - 1$, are properly tuned in real time. Then, we can escape from the control specification on the robust performance that can be the constraint in improving the control performance as discussed earlier when we adopt a single semiactive control law.

By optimizing design parameters α and θ under the semiactive control based on the output emulation approach in the previous subsection, it is possible to obtain a semiactive control law C_k with good control performance for a single earthquake disturbance v_k . In fact, since there are only two design parameters, it is possible to apply an exhaustive search and find the globally optimal solution. Therefore, the remaining problem is to get a tuning strategy that interpolates n_c reference active control laws with available information. In other words, we need to get a map M from the available sensor data (and/or their functions) to the interpolation parameter $0 \leq \beta_l(t) \leq 1$, $l = 1, \dots, n_c - 1$. If we get a good map M to achieve high performance for a wide range of earthquake disturbances, we can adapt to the future occurring earthquake with unknown time and frequency characteristics. Such adaptive semiactive control law without constraints on the robust performance realizes further performance improvement.

However, at the moment, there is no clue to get a good map M. For example, we cannot determine what kind of sensor data should be used as input for M and what function should be employed as the map M because we cannot clarify the relationship between the characteristics of the earthquake disturbance and that of the optimized semiactive control law.

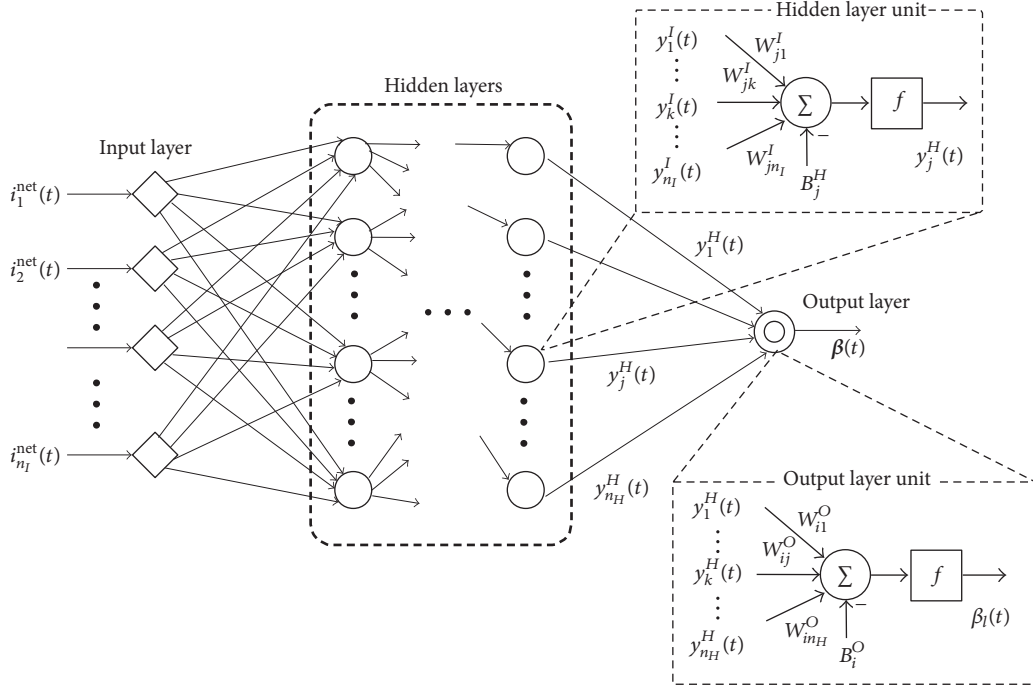


FIGURE 5: Structure of the multilayered ANN.

Therefore, in this study, we adopt a multilayered artificial neural network (ANN) as the basic structure of M and optimizing ANN parameters according to the specification of semiactive control system. We use the ANN as the map M , expecting to have a high ability to construct various functions including nonlinear mappings [6].

A schematic diagram of the multilayered ANN is shown in Figure 5. The ANN input is a vector $\mathbf{i}^{net}(t) = [i_1^{net}(t), \dots, i_{n_I}^{net}(t)]^T$ which is composed of the available signal in the control system. Signals such as $y(t)$, $u(t)$, and $v(t)$ of the structural model obtained by sensors installed on the control object are fed to the ANN input layer. The ANN outputs an interpolation parameter vector $\boldsymbol{\beta}(t) = [\beta_1(t), \dots, \beta_{n_c-1}(t)]^T$ from the output layer. Elements of the vector $\boldsymbol{\beta}(t)$ are the interpolation parameters of the reference active control input $0 \leq \beta_l(t) \leq 1$, $l = 1, \dots, n_c - 1$. There are several hidden layers between the input and output layers to enhance the mapping description capability of the ANN.

To describe the structure of the ANN more specifically, let U_k^I , $k = 1, \dots, n_I$, U_j^H , $j = 1, \dots, n_H$, and U_i^O , $i = 1, \dots, n_O$, be units in the input, hidden, and output layers, respectively, where n_I , n_H , and $n_O = n_c - 1$ are the number of neurons of the respective layers. Without loss of generality, we assume here that the number of the hidden layers is one for simplicity. The l th element of the output layer of the network $\beta_l(t)$, $l = 1, \dots, n_c - 1$, is obtained as follows:

$$\beta_l(t) = f \left(\sum_{j=1}^{n_H} W_{lj}^O y_j^H(t) - B_l^O \right), \quad l = 1, \dots, n_c - 1,$$

$$y_j^H(t) = f \left(\sum_{k=1}^{n_I} W_{jk}^H y_k^I(t) - B_j^H \right) \quad j = 1, \dots, n_H,$$

$$y_k^I(t) = i_k^{net}(t), \quad k = 1, \dots, n_I,$$

(28)

where $\underline{W}_{ij}^O \leq W_{ij}^O \leq \overline{W}_{ij}^O$, $\underline{W}_{jk}^H \leq W_{jk}^H \leq \overline{W}_{jk}^H$, $\underline{B}_i^O \leq B_i^O \leq \overline{B}_i^O$, and $\underline{B}_j^H \leq B_j^H \leq \overline{B}_j^H$, $i = 1, \dots, n_O$, $j = 1, \dots, n_H$, $k = 1, \dots, n_I$, are weights connecting U_i^O and U_j^H , U_j^H and U_k^I , and biases for U_i^O and U_j^H , respectively. The function $f(x)$ is the sigmoid function given as

$$f(x) = \frac{1}{1 + e^{-x}}. \quad (29)$$

Note that $0 \leq f(x) \leq 1 \forall x$. Because of $0 \leq f(x) \leq 1$, all the elements of the interpolation parameter $\beta_l(t)$, $l = 1, \dots, n_c - 1$ stay in the interval $0 \leq \beta_l(t) \leq 1$, $l = 1, \dots, n_c - 1$. Design parameters of the ANN are the weights and bias in all the units of the ANN. These parameters are optimized as the adaptive scheduling mechanism to improve the control performance of the semiactive control system.

If the ideal interpolation parameters of the adaptive gain scheduling mechanism are available as train sets and they can be used for the ANN learning, we can use the back propagation method [11] to optimize the weights and biases of the ANN efficiently. However, the desired map denoted by M_d is not known in advance under this problem formulation. That is, we do not know what is the best strategy to change the interpolation parameter $0 \leq \beta_l \leq 1$, $l =$

$1, \dots, n_c - 1$, for an earthquake disturbance at a certain time t . Therefore, in the present study, a genetic algorithm (GA) is applied to the optimization of the design parameters of the ANN. In the GA, all ANN design parameters are combined into one chromosome. Individuals with different chromosomes are randomly generated in the initial stage and the optimal chromosome is searched by the GA. In the GA search, genetic operations, for example, crossover, mutation, and selection, are repeatedly applied to all individuals so that the fitness of the individual is maximized; that is, the objective function representing the control performance of the semiactive control systems is optimized.

4. Design Example

A 6-DOF base-isolated structural system with a semiactive damper [12, 13] in Figure 6 is used as a design example. The structural parameters of the 6-DOF structural system are shown in Table 1. The maximum and minimum damping coefficients of the semiactive damper in (1) are defined as $\bar{d}_1^s = 20 \times 10^3$ [Ns/m], $\underline{d}_1^s = 0$ [Ns/m] in (5), respectively.

In this example we obtain three semiactive control laws C_k , $k = 1, \dots, 3$, for the specific earthquake disturbance. These semiactive control laws are designed to exert the best control performance for three recorded earthquake disturbances used, that is, $k = 1$: El Centro NS (1940), $k = 2$: Hachinohe NS (1968), and $k = 3 (=n_c)$: Kobe NS (1995) waves. The semiactive control law C_k , $k = 1, 2, 3$, is obtained with the output emulation approach in Section 3.2 so that the control performance of the k th semiactive control law is optimized for the corresponding k th earthquake disturbance under the setting of the control system in Figure 3. The index for evaluating the control performance of the semiactive control system is defined as follows:

$$J_k = \max(J_k^{s/on}, J_k^{s/off}), \quad k = 1, \dots, n_c \quad (30)$$

$$J_k^{s/off} = \sum_{j=1}^n \frac{\text{RMS}(r_j^{k,semi})}{\text{RMS}(r_j^{k,off})} + \sum_{j=1}^n \frac{\text{Peak}(r_j^{k,semi})}{\text{Peak}(r_j^{k,off})} + \sum_{j=1}^n \frac{\text{RMS}(q_j^{k,semi})}{\text{RMS}(q_j^{k,off})} + \sum_{j=1}^n \frac{\text{Peak}(q_j^{k,semi})}{\text{Peak}(q_j^{k,off})}, \quad (31)$$

$$J_k^{s/on} = \sum_{j=1}^n \frac{\text{RMS}(r_j^{k,semi})}{\text{RMS}(r_j^{k,on})} + \sum_{j=1}^n \frac{\text{Peak}(r_j^{k,semi})}{\text{Peak}(r_j^{k,on})} + \sum_{j=1}^n \frac{\text{RMS}(q_j^{k,semi})}{\text{RMS}(q_j^{k,on})} + \sum_{j=1}^n \frac{\text{Peak}(q_j^{k,semi})}{\text{Peak}(q_j^{k,on})},$$

where $r_j^{k,*}$ and $q_j^{k,*}$, $j = 1, \dots, n$, $*$ = semi, off, or on are the relative displacement between j and $(j-1)$ -th floors and the absolute acceleration of the j th floor for the k th, $k = 1, \dots, n_c$, earthquake disturbance, respectively. Superscripts $*$ = semi, off, or on are the case of the semiactive control based on the proposed output emulation approach, passive off, and passive

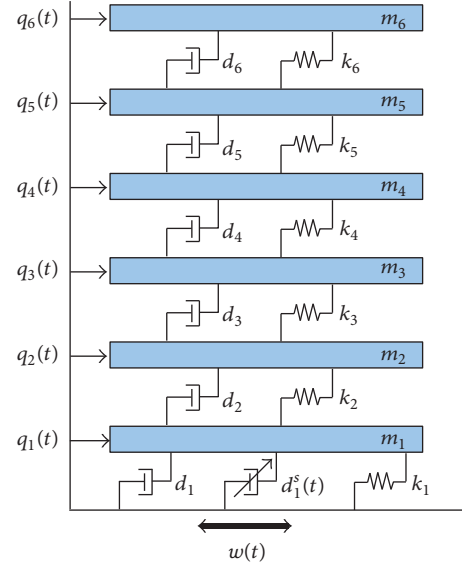


FIGURE 6: 6-DOF base-isolated structural system.

TABLE 1: Structural parameters of the 6-DOF structural system.

Floor	m_i [kg]	d_i [kNs/m]	k_i [kN]
1	6800	7.45	231.50
2	5897	670	33732
3	5897	580	29093
4	5897	570	28621
5	5897	500	24954
6	5897	380	19059

TABLE 2: Optimal design parameters of the semiactive control for each earthquake disturbance.

Earthquake wave (k)	α	θ ($\times \pi/2$)
El Centro NS ($k = 1$)	0.20	0.85
Hachinohe NS ($k = 2$)	0.38	1
Kobe NS ($k = 3$)	0.20	0.92

on cases, respectively. Indices $J_k^{s/off}$ and $J_k^{s/on}$ are functions to evaluate the control performance of the semiactive control system in the case of the k th earthquake disturbance, that is, $J_k^{s/off}$: the semiactive control case compared to the passive off case, $J_k^{s/on}$: the semiactive control case compared to the passive on case.

The optimal design parameters for each earthquake disturbance are summarized in Table 2. These optimal design parameters are obtained with the exhaustive search in a range $0.1 \leq \alpha \leq 0.4$ and $0.7 \times (\pi/2) \leq \beta \leq 1 \times (\pi/2)$. Since the optimal design parameters for the specified earthquake disturbance are different from each other, the semiactive control based on the optimal reference active control law for a specific earthquake disturbance has different control characteristics.

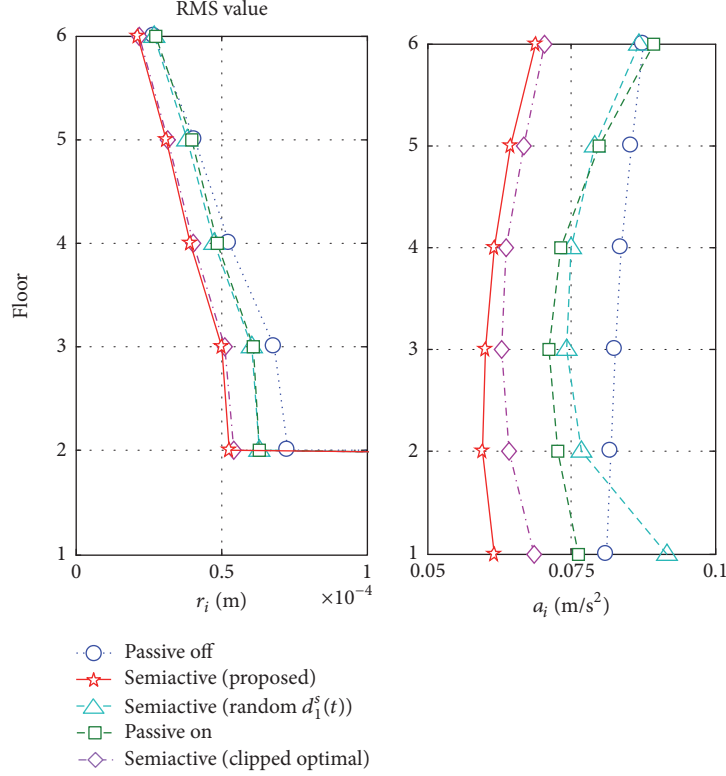


FIGURE 7: Simulation results for the El Centro NS (1940) earthquake disturbance; RMS values of the relative displacement between neighboring floors and absolute acceleration of each floor.

As the adaptive scheduling mechanism, the ANN with two output signals $0 \leq \beta_l \leq 1, l = 1, 2$, for the interpolation of three reference active control laws corresponds to three semiactive control laws $C_k, k = 1, 2, 3$. The interpolated reference active control input denoted by $u_l^{\text{ra}}(t)$ is the convex combination of $u_k^{\text{ra}}(t), k = 1, 2, 3$ with $\beta_1(t)$, and $\beta_2(t)$ given by

$$\begin{aligned} u_l^{\text{ra}}(t) &= \{1 - \beta_1(t)\} u_1^{\text{ra}}(t) + \beta_1 \{1 - \beta_2(t)\} u_2^{\text{ra}}(t) \\ &\quad + \beta_1(t) \beta_2(t) u_3^{\text{ra}}(t) \\ &= [\{1 - \beta_1(t)\} K_1 + \beta_1 \{1 - \beta_2(t)\} K_2 \\ &\quad + \beta_1(t) \beta_2(t) K_3] x_a(t), \end{aligned} \quad (32)$$

where $K_k, k = 1, 2, 3$, is the state-feedback gain matrix for the k th earthquake disturbance obtained each of which is obtained with optimal design parameters in Table 2.

As the input signal of the ANN, we employ the acceleration of the earthquake wave $\ddot{w}(t)$, its time derivative, and integral. Namely, the input signal vector \mathbf{i}^{net} is given as

$$\mathbf{i}^{\text{net}} = \begin{bmatrix} \ddot{w}(t) \\ \dot{w}(t) \\ \frac{d\ddot{w}(t)}{dt} \end{bmatrix}. \quad (33)$$

In the design example, we introduce two hidden layers whose numbers of units are 40 and 5, respectively. The number of units in each hidden layer is determined by trial and error. The total number of design parameters in the ANN becomes 377 and they are optimized with the GA. The objective function to evaluate the control performance of the semiactive control system is defined as follows:

$$J = \sum_{i=1}^{n_w} J_i, \quad (34)$$

where n_w is the number of earthquake disturbances to obtain the simulated structural response for the GA-based optimization. The index $J_i, i = 1, \dots, n_w$, is the performance index defined in (30) for the i th earthquake disturbance. In the GA-based optimization of the ANN, the objective function J in (34) is obtained with the simulation for all individuals containing design parameter of the ANN with the above three earthquake disturbances and the BCJLI (artificial) wave, that is, we determine $n_w = 4$ in (34). We set the population (number of individuals) of each generation and the maximum number of the generations in the GA as 20 and 200, respectively.

The results of the optimized semiactive control system for El Centro NS, BCJLI, Hachinohe NS, and Kobe NS waves are shown in Figures 7, 8, 10, 11, 13, 14, 16, and 17, respectively. The result of the case where the variable damping coefficient

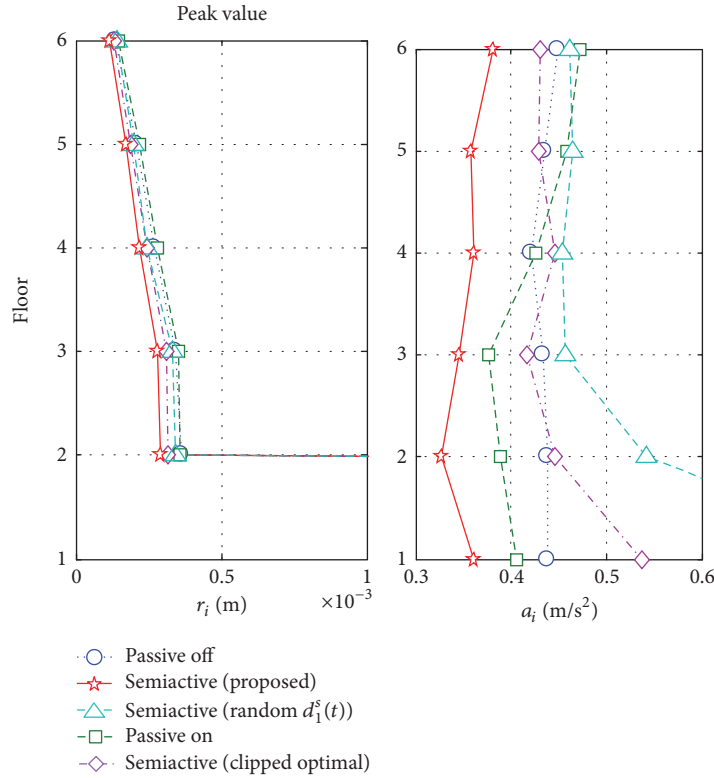


FIGURE 8: Simulation results for the El Centro NS (1940) earthquake disturbance; peak values of the relative displacement between neighboring floors and absolute acceleration of each floor.

$d_1^s(t)$ of the semiactive damper is randomly changed is also shown in the figures. The semiactive control based on the proposed approach shows good control performance for all the earthquake disturbances over the passive off and on and the random change cases.

Moreover, for comparison, the results of the case with the clipped optimal control [1], which is a popular and conventional semiactive control law that is often applied to building structures, are also shown in each figure. For the reference active control law of the clipped optimal control, the state-feedback control law in (10) is adopted as well as design parameters with the same pole location constraints as the present formulation. Design parameters α and θ minimizing the index in (34) are obtained by using the exhaustive search. In this case, the clipped optimal control law is designed to have robust performance characteristics, that is, to improve control performance on average for all considered earthquake disturbances. We can clearly see that the proposed semiactive control with the adaptive scheduling mechanism achieves better control performance compared with that of the clipped optimal control.

To see the behavior of the adaptive scheduling mechanism for each earthquake disturbance, the variable damping coefficient of the semiactive damper and the output of the ANN $\beta_1(t)$ and $\beta_2(t)$ are shown in Figures 9, 12, 15, and 18, respectively. It is found that the ANN generates the interpolation

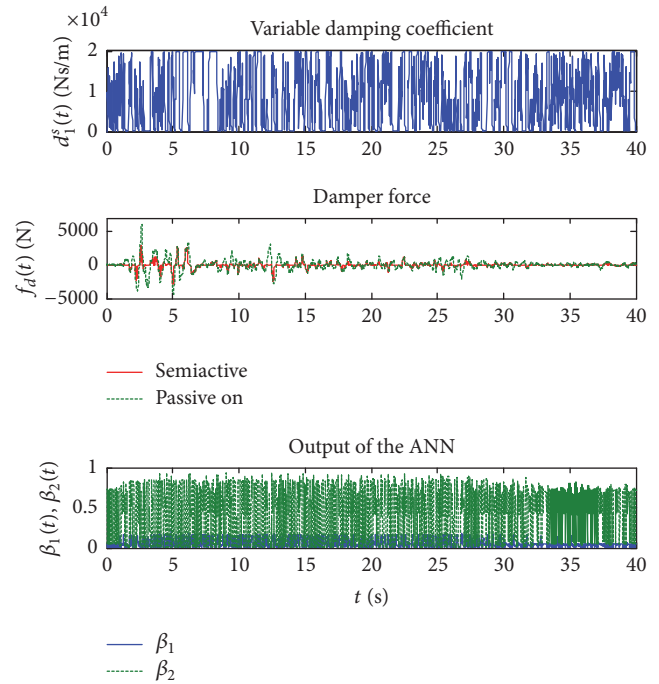


FIGURE 9: Simulation results for the El Centro NS (1940) earthquake disturbance; variable damping coefficient $d_1^s(t)$, force of damper $f_d(t)$, and output signals of the ANN $\beta_1(t)$ and $\beta_2(t)$.

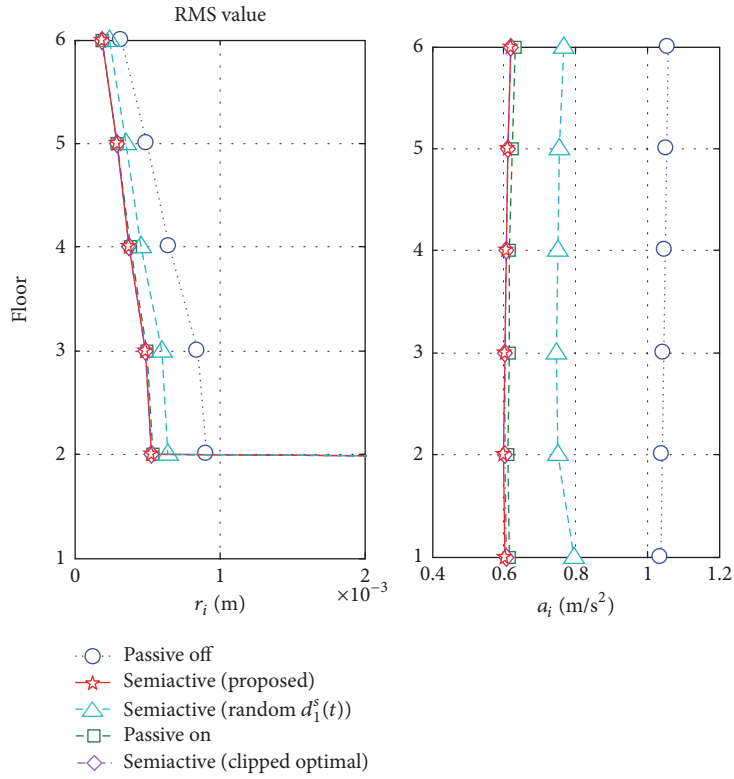


FIGURE 10: Simulation results for the BCJLI earthquake disturbance; RMS values of the relative displacement between neighboring floors and absolute acceleration of each floor.

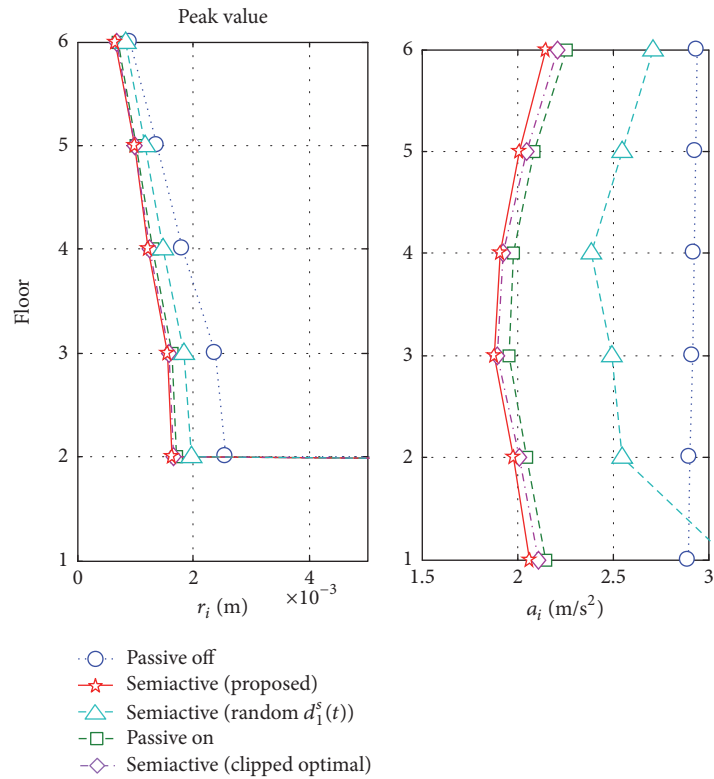


FIGURE 11: Simulation results for the BCJLI earthquake disturbance; peak values of the relative displacement between neighboring floors and absolute acceleration of each floor.

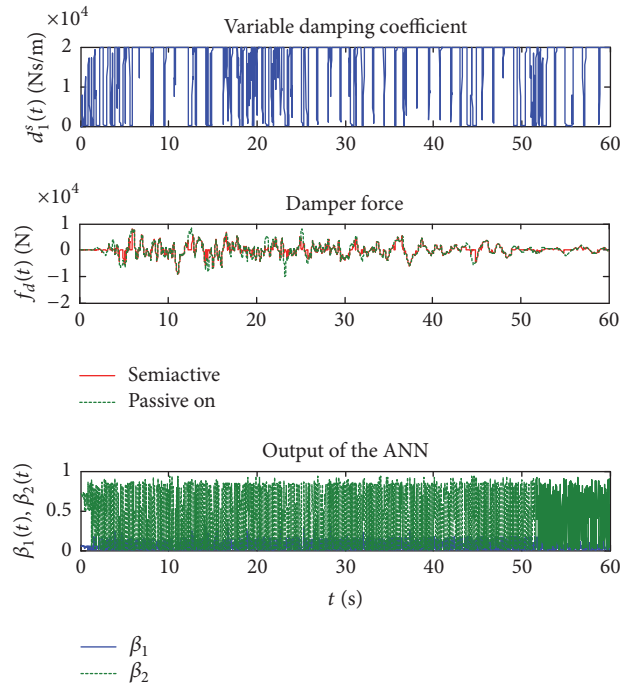


FIGURE 12: Simulation results for the BCJLI earthquake disturbance; variable damping coefficient $d_1^s(t)$, force of damper $f_d(t)$, and output signals of the ANN $\beta_1(t)$ and $\beta_2(t)$.

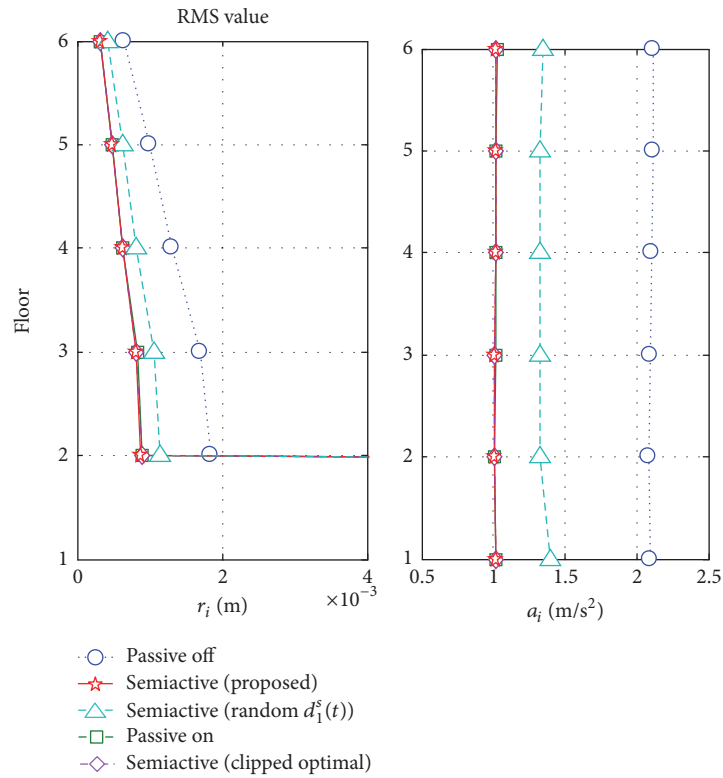


FIGURE 13: Simulation results for the Hachinohe NS (1968) earthquake disturbance; RMS values of the relative displacement between neighboring floors and absolute acceleration of each floor.

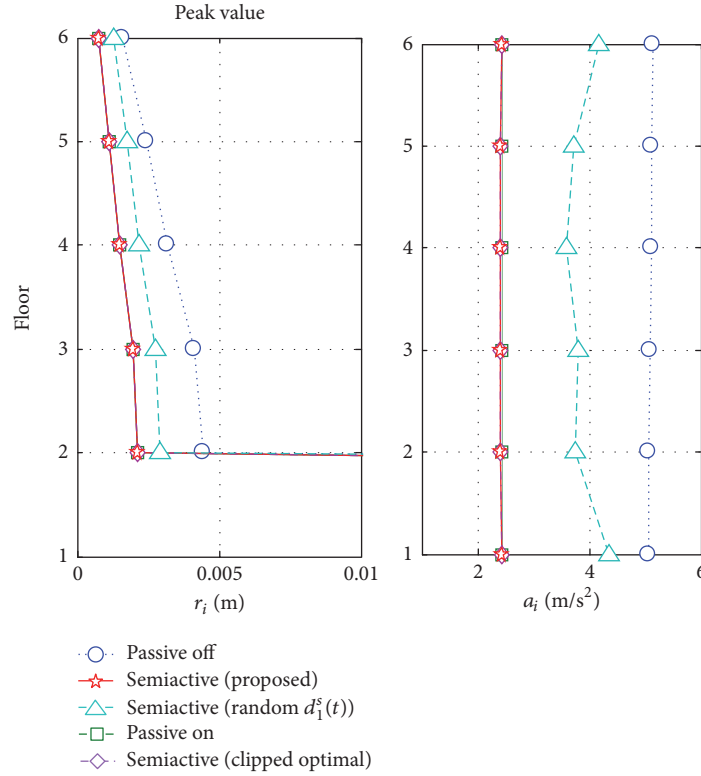


FIGURE 14: Simulation results for the Hachinohe NS (1968) earthquake disturbance; peak values of the relative displacement between neighboring floors and absolute acceleration of each floor.

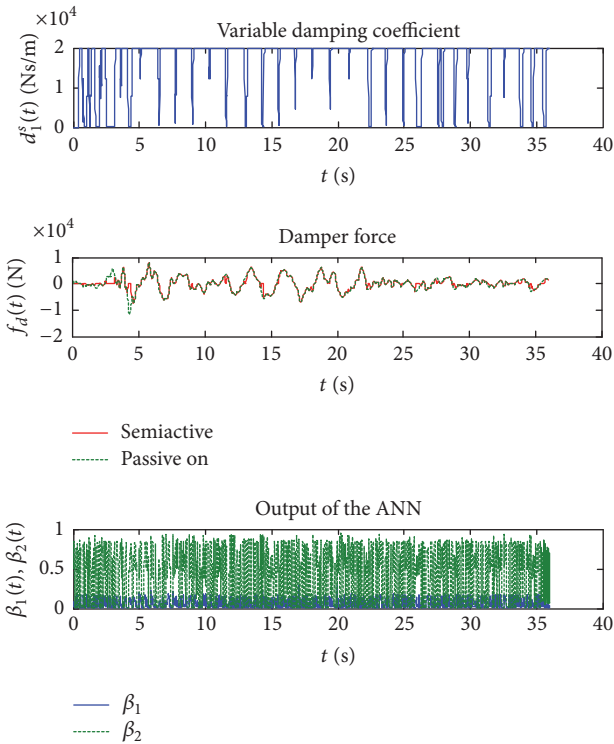


FIGURE 15: Simulation results for the Hachinohe NS (1968) earthquake disturbance; variable damping coefficient $d_1^s(t)$, force of damper $f_d(t)$, and output signals of the ANN $\beta_1(t)$ and $\beta_2(t)$.

parameters to optimize the control performance. The time history of the force of the semiactive damper $f_d(t) = d_1^s(t)(\dot{q}_1(t) - \dot{w}(t))$ for each earthquake disturbance with that in the passive on case is shown in those figures. Also, the peak value of the damper force in each case is in Table 3. We can clearly see that the force of the damper in the case of the semiactive control is much smaller than that of the passive on case. The result shows that the proposed semiactive control method shows good control performance on not only the vibration suppression but also the required damper force compared to the conventional passive control method.

To evaluate the control performance of the semiactive control system for the unknown earthquake disturbance, results for the Taft NS (1952) and Akita NS (1983) waves are shown in Figures 19, 20, 22, and 23, respectively. The variable damping coefficient of the semiactive damper, the force of the damper (in the semiactive and passive on cases), and the output of the ANN are also shown in Figures 21 and 24. Peak values of the damper force in the semiactive and passive on cases are shown in two rows at the bottom of Table 3. With the result, we can see that the good control performance is also achieved, compared to not only that of the passive off and passive on cases, but also the clipped optimal control case. This result shows that the proposed adaptive gain scheduled semiactive control method has superior control performance compared with the control method aimed at robust performance, which is conventionally used.

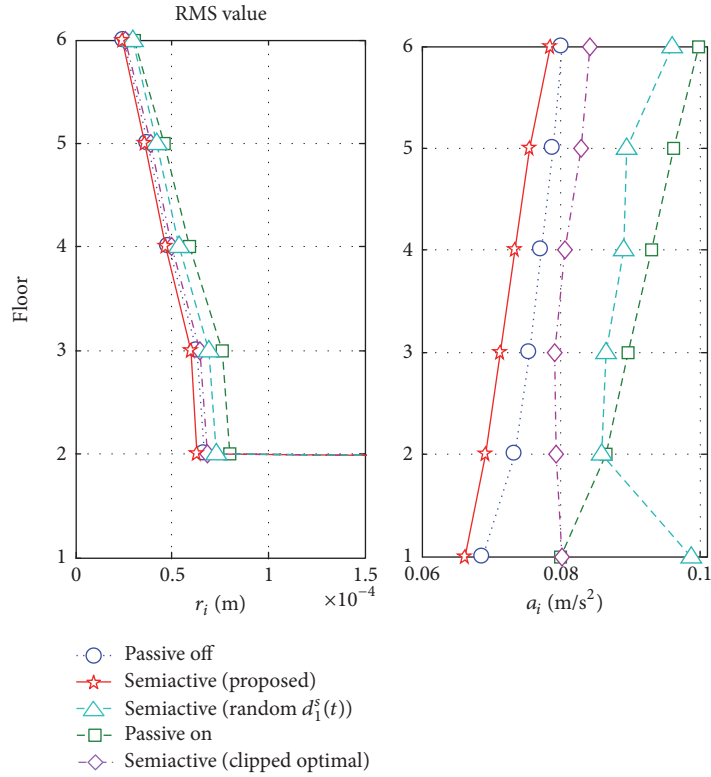


FIGURE 16: Simulation results for the Kobe NS (1995) earthquake disturbance; RMS values of the relative displacement between neighboring floors and absolute acceleration of each floor.

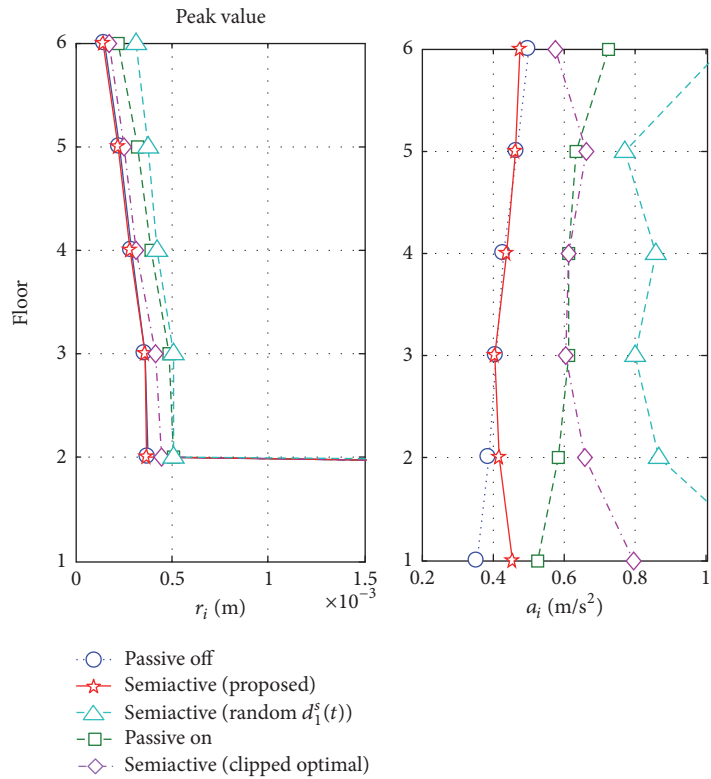


FIGURE 17: Simulation results for the Kobe NS (1995) earthquake disturbance; peak values of the relative displacement between neighboring floors and absolute acceleration of each floor.

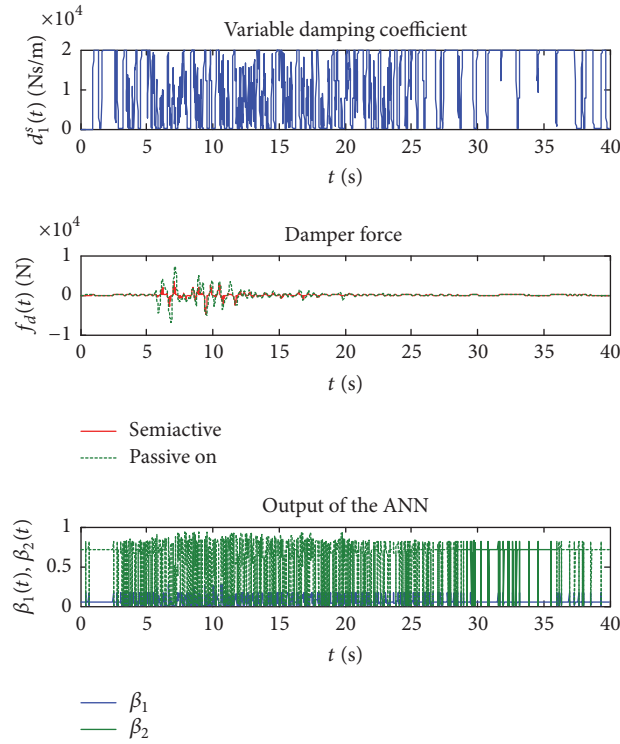


FIGURE 18: Simulation results for the Kobe NS (1995) earthquake disturbance; variable damping coefficient $d_1^s(t)$, force of damper $f_d(t)$, and output signals of the ANN $\beta_1(t)$ and $\beta_2(t)$.

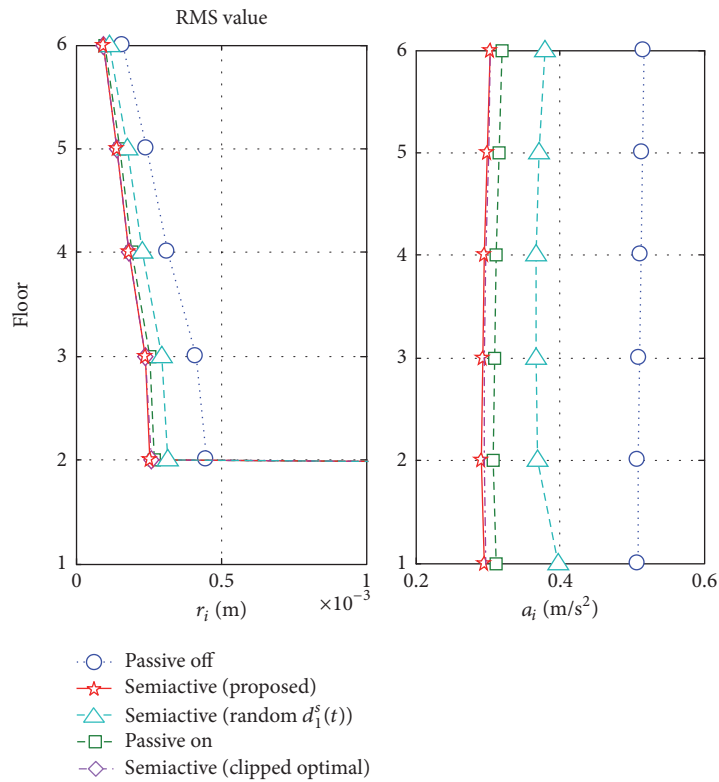


FIGURE 19: Simulation results for the Taft NS (1952) earthquake disturbance; RMS values of the relative displacement between neighboring floors and absolute acceleration of each floor.

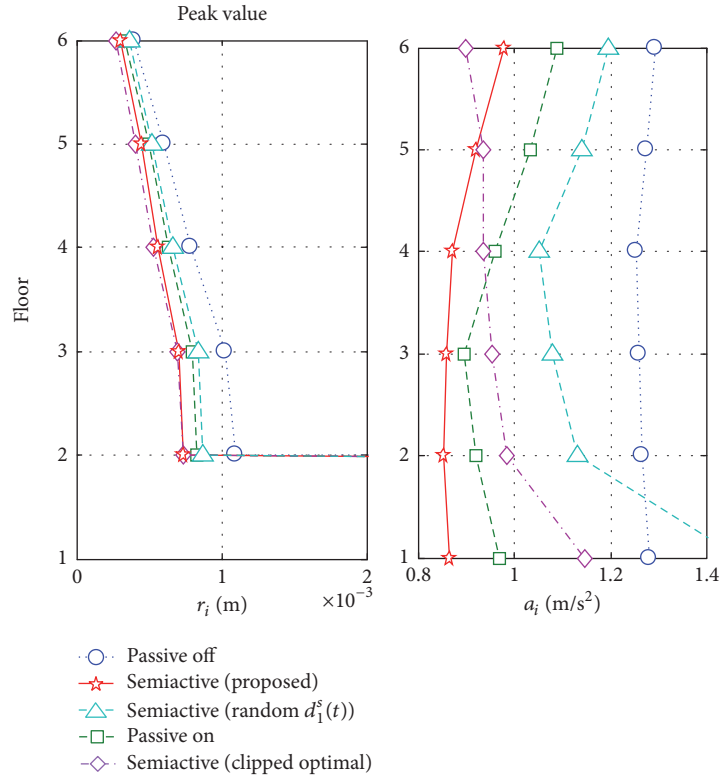


FIGURE 20: Simulation results for the Taft NS (1952) earthquake disturbance; Peak values of the relative displacement between neighboring floors and absolute acceleration of each floor.

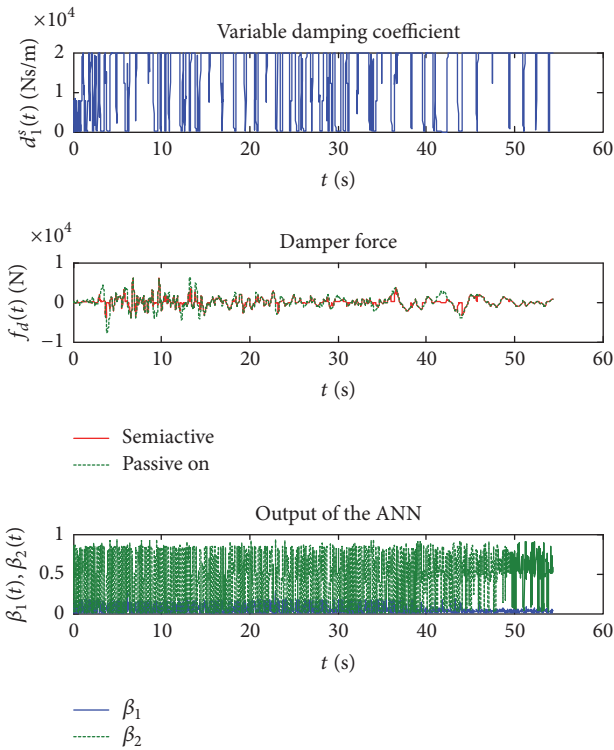


FIGURE 21: Simulation results for the Taft NS (1952) earthquake disturbance; variable damping coefficient $d_1^s(t)$, force of damper $f_d(t)$, and output signals of the ANN $\beta_1(t)$ and $\beta_2(t)$.

TABLE 3: Peak force of the damper.

Earthquake	Passive on [kN]	Semiactive [kN]
El Centro NS	6.04	2.97
BCJL1	10.02	9.24
Hachinohe NS	11.65	7.83
Kobe NS	7.29	5.00
Taft NS	7.85	6.02
Akita NS	9.39	8.20

5. Conclusion

In order to achieve high control performance of semiactive vibration control, we have proposed a control strategy consisting of adaptive scheduling mechanisms of multiple semiactive control laws with specific control characteristics. The adaptive scheduling mechanism is designed as an interpolator of the reference active control laws, each of which is designed for a specific law for the single specified seismic wave and used for the semiactive control based on the output emulation approach. The ANN is adopted as the adaptive scheduling mechanism and design parameters of the ANN are optimized by the GA. Compared to the passive control case and the conventional semiactive control method based on the clipped optimal control method, the proposed semiactive control method is shown to have better control performance on vibration suppression and flexibility

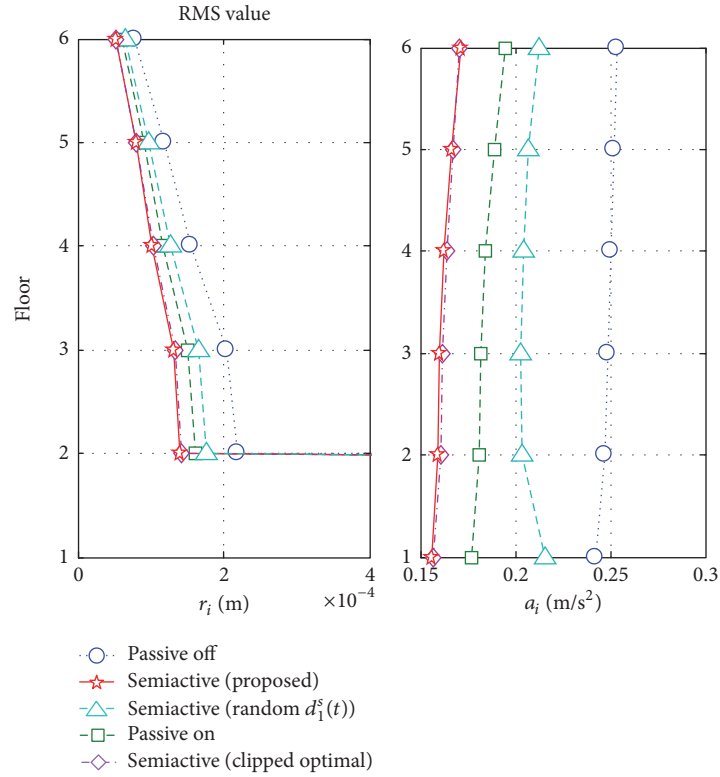


FIGURE 22: Simulation results for the Akita NS (1983) earthquake disturbance; RMS values of the relative displacement between neighboring floors and absolute acceleration of each floor.

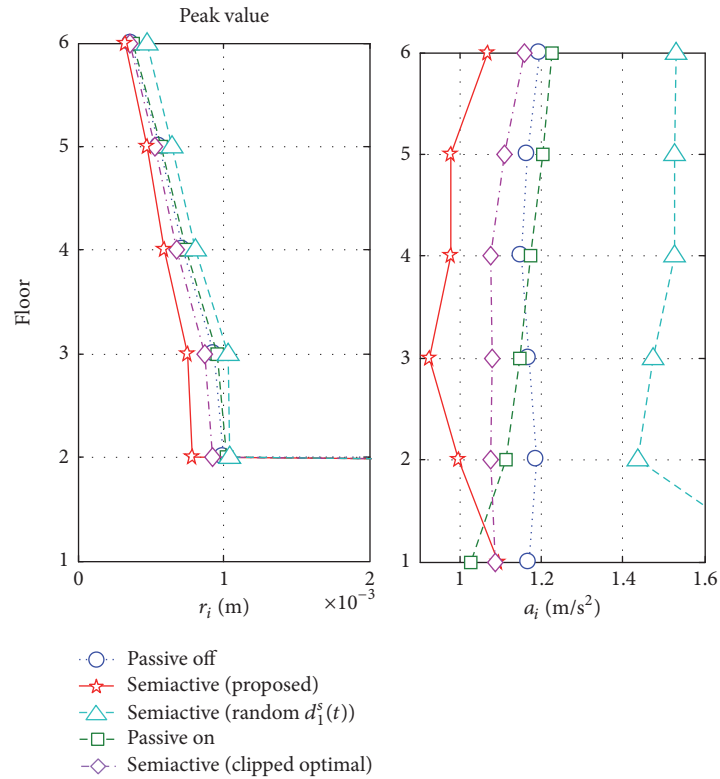


FIGURE 23: Simulation results for the Akita NS (1983) earthquake disturbance; peak values of the relative displacement between neighboring floors and absolute acceleration of each floor.

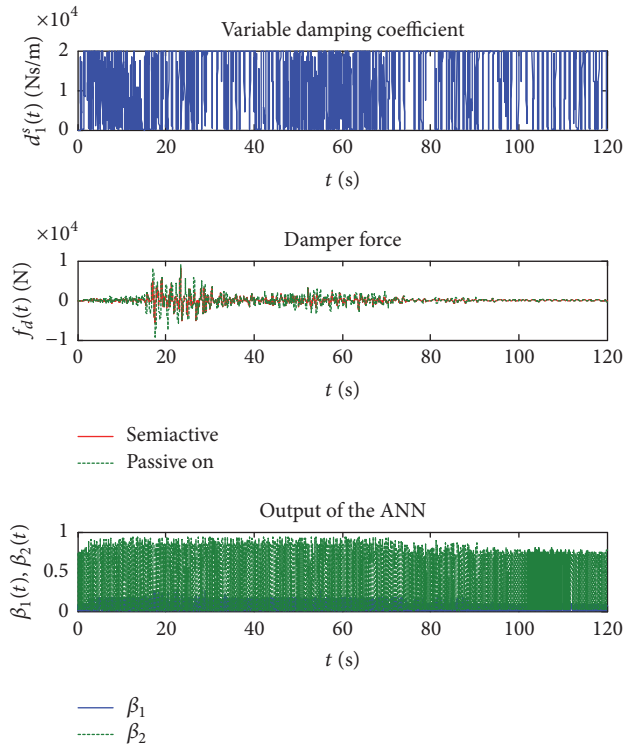


FIGURE 24: Simulation results for the Akita NS (1983) earthquake disturbance; variable damping coefficient $d_1^s(t)$, force of damper $f_d(t)$, and output signals of the ANN $\beta_1(t)$ and $\beta_2(t)$.

against earthquake disturbances whose time and frequency characteristics are unknown over the conventional semiactive control approach aiming at the robust performance characteristics.

Conflicts of Interest

The authors declare that they have no conflicts of interest.

Acknowledgments

This work was partially supported by Japan Society for the Promotion of Science (JSPS), Grant-in-Aid for Scientific Research (C), 15K05858, 2016.

References

- [1] S. J. Dyke, B. F. Spencer Jr., M. K. Sain, and J. D. Carlson, "An experimental study of MR dampers for seismic protection," *Smart Materials and Structures*, vol. 7, no. 5, pp. 693–703, 1998.
- [2] H. P. Gavin, "Control of seismically excited vibration using electrorheological materials and Lyapunov methods," *IEEE Transactions on Control Systems Technology*, vol. 9, no. 1, pp. 27–36, 2001.
- [3] H. Sodeyama, K. Suzuki, and K. Sunakoda, "Development of large capacity semi-active seismic damper using magnetorheological fluid," *Journal of Pressure Vessel Technology, Transactions of the ASME*, vol. 126, no. 1, pp. 105–109, 2004.

- [4] N. Varadarajan and S. Nagarajaiah, "Wind response control of building with variable stiffness tuned mass damper using empirical mode decomposition/Hilbert transform," *Journal of Engineering Mechanics*, vol. 130, no. 4, pp. 451–458, 2004.
- [5] K. Hiramoto, T. Matsuoka, and K. Sunakoda, "Semi-active vibration control of structural systems based on a reference active control law: Output emulation approach," *Structural Control and Health Monitoring*, vol. 23, no. 3, pp. 423–445, 2016.
- [6] M. T. Hagen, H. B. Demuth, and M. H. Beale, *Neural Network Design*, Ed. PWS Publishing, Boston, MA, USA.
- [7] K. Kanai, "Semi-empirical formula for the seismic characteristics of the ground," *Univ. Tokyo Bull. Earthquake Res. Inst.*, vol. 35, pp. 309–325, 1957.
- [8] H. Tajimi, "A statistical method of determining the maximum response of a building structure during an earthquake," in *proceedings of Proc. 2nd World Conf. Earthquake Eng.*, pp. 781–798, 1960.
- [9] A. Packard and J. Doyle, "The complex structured singular value," *Automatica*, vol. 29, no. 1, pp. 71–109, 1993.
- [10] M. Chilali and P. Gahinet, " H_∞ design with pole placement constraints: An LMI approach," *IEEE Transactions on Automatic Control*, vol. 41, no. 3, pp. 358–367, 1996.
- [11] D. E. Rumelhart, G. E. Hinton, and R. J. Williams, "Learning representations by back-propagating errors," *Nature*, vol. 323, no. 6088, pp. 533–536, 1986.
- [12] J. M. Kelly, G. Leitmann, and A. G. Soldatos, "Robust control of base-isolated structures under earthquake excitation," *Journal of Optimization Theory and Applications*, vol. 53, no. 2, pp. 159–180, 1987.
- [13] H. Li and J. Ou, "A design approach for semi-active and smart base-isolated buildings," *Structural Control and Health Monitoring*, vol. 13, no. 2-3, pp. 660–681, 2006.

Research Article

Experimental Study on Variation Rules of Damping with Influential Factors of Tuned Liquid Column Damper

Yang Yu,^{1,2,3} Lixin Xu,^{1,2} and Liang Zhang⁴

¹State Key Laboratory of Hydraulic Engineering Simulation and Safety, Tianjin University, Tianjin 300350, China

²Collaborative Innovation Center for Advanced Ship and Deep-Sea Exploration, Shanghai 200240, China

³State Key Laboratory of Ocean Engineering, Shanghai Jiaotong University, Shanghai 200240, China

⁴Beijing Spacecrafts, Beijing 100094, China

Correspondence should be addressed to Lixin Xu; lixin.xu@tju.edu.cn

Received 2 May 2017; Revised 16 August 2017; Accepted 26 September 2017; Published 26 October 2017

Academic Editor: Felice Ponzo

Copyright © 2017 Yang Yu et al. This is an open access article distributed under the Creative Commons Attribution License, which permits unrestricted use, distribution, and reproduction in any medium, provided the original work is properly cited.

A tuned liquid column damper (TLCD) is a more effective form of passive control for structural vibration suppression and may be promising for floating platform applications. To achieve good damping effects for a TLCD under actual working conditions, factors that influence the damping characteristics need to be identified. In this study, the relationships between head loss coefficients and other factors such as the total length of the liquid column, opening ratio, Reynolds number, Kc number, and horizontal length of the liquid column were experimentally investigated. By using a hydraulic vibration table, a vibration test system with large-amplitude motion simulation, low-frequency performance, and large stroke force (displacement) control is devised with a simple operation and at low cost. Based on the experimental method of uniform design, a series of experimental studies were conducted to determine the quantitative relationships between the head loss coefficient and other factors. In addition, regression analyses indicated the importance of each factor affecting the head loss coefficient. A rapid design strategy of TLCD head loss coefficient is proposed. This strategy can help people conveniently and efficiently adjust the head loss coefficient to a specified value to effectively suppress vibration.

1. Introduction

The dynamic response of tall structures such as high-rise buildings and ocean platforms is highly apparent under external loads [1–3]. The vibration of such structures can be suppressed by strengthening the structure and increasing its size; however, this leads to a significant increase in its cost. To overcome this problem, in recent years, additional dampers have been widely applied to suppress vibrations. Dampers are used in high-rise buildings to reduce the impact of wind and earthquake loads and in offshore platforms, to reduce the effect of waves.

Thus far, few studies have focused on the motion suppression of floating platforms in complex operating environments. Structural vibration control methods can be categorized into three types: active, semiactive, and passive. Passive control is usually used to suppress the vibration of structures by dissipating and absorbing energy. Passive control dampers

are of three main types: tuned mass damper (TMD), tuned liquid damper (TLD), and tuned liquid column damper (TLCD). Of these, a TLCD, which was developed based on the TLD, is the most effective.

The main body of the TLCD is a U-shaped water tunnel that consists of two vertical columns connected by a horizontal column filled with liquid, usually water. An orifice plate is installed at the center of the horizontal column; it changes the damping effect by adjusting the discharge passing through. When the main structure vibrates, a part of the energy is transferred to the liquid column, which absorbs the same energy through its movement. At the same time, the pressure difference between the two vertical liquid columns produces a damping force that suppresses the vibration of the main structure. Although few studies have investigated the application of TLCDs to floating platforms, many existing structures on such platforms, such as oil containers, fresh water containers, and even floating tanks, could be modified

to incorporate TLCDs. In addition, given that TLCDs have low manufacturing and installation costs as well as relatively low maintenance requirements, they might actually be greatly advantageous for applications to floating platforms.

Sakai et al. [4] first proposed TLCDs in 1989. Hochrainer [5] presented a detailed derivation of their working principle and applied a bang-bang control scheme based on linear optimal control to reduce transient vibrations. Hitchcock et al. [6–8] optimized the original TLCDs by varying their cross section to overcome their narrow frequency band. They also studied the damping effect of several TLCDs and its influence on the vibration frequency range and head loss coefficient. Lee et al. [9–11] built a structural model on a shaking table with acceleration control and experimentally implemented a TLCD to investigate the control of the response of building structures excited by earthquakes. By comparing the liquid column amplitude and energy consumption between a TLD and a TLCD with the same size and damping effect, they found that the natural vibration frequency of the TLCD has a greater influence on the liquid column amplitude, leading to higher energy consumption for the main structure. In addition, by integrating the characteristics of both TLD and TLCD, they designed a bidirectionally tuned liquid column and sloshing damper that suppressed vibrations along the two principal axes of a structure. Chaiviriyawong et al. [12] used a computational fluid dynamics model to study the variation of the flow velocity in the elbow between horizontal and vertical liquid columns of different widths. Chan and Ding [13] conducted structural experiments to compare the damping effects of TLCDs with liquid columns of different lengths and tilt angles. To make TLCDs more effective in reducing structural vibrations, Al-Saif et al. [14] modified a TLCD by placing a coated steel ball as a moving orifice inside the horizontal section of the damper instead of the orifice plate and disturbed the flow so as to improve the absorber's attenuation performance. In recent years, TLCDs of different forms have been developed as their range of applications has broadened. Huo and Li [15] assessed the application of a TLCD to the control system of a jacket platform and analyzed the control performance of a circular TLCD on suppressing the coupled torsion vibration of an offshore platform under waves and earthquake loads. Lee et al. [16, 17] were the first to apply a TLCD in a floating platform and provide experimental verification. Moreover, they compared the effects of two different installation arrangements: on the floating platform and underwater.

For the TLCD to have good damping effects, the functional relationships that determine the damping characteristics must be identified. The most direct way to do so is to adjust the relevant parameters of the orifice plate. For a given size and conditions such as external excitation frequency and quality, Chen and Chao [18] proposed a method for calculating the optimal damping ratio for a TLCD that has the optimum damping effect on the main structure. Additionally, the influence of the optimal damping ratio on the harmonic response was discussed for different effective length ratios. Shum and Xu [19, 20] developed a closed-form optimal solution scheme for a TLCD-structure system and determined its optimal damping ratio for suppressing harmonic

vibrations. Chakraborty et al. [21] discussed the optimization of the damping coefficient and other parameters with a reasonable maximum amplitude of liquid oscillation. Yalla and Kareem [22] varied the inclination angle of the orifice plate to determine the optimal damping ratio for an orifice plate with a narrow slit and confirmed that the damping ratio of the TLCD strongly influences the amplitude of oscillations in the main structure. Lee et al. [11] discussed the correlation between the liquid motion amplitude and different external excitation amplitudes under different frequency ratios and damping coefficients and analyzed the relationships between the excitation amplitude and the parameters related to the TLCD. Furthermore, some researchers performed experimental tests. Wu et al. [23–26] proposed an analytical method for determining the optimal damping ratio with variable cross sections and found that it is inversely proportional to the external excitation amplitude. According to the two-degree-of-freedom (2-DOF) motion equation and transfer relationship between the main structure and the TLCD, they established an experimental measurement method for the head loss coefficient based on the equivalent linear damping item and motion amplitude. The head loss for a TLCD is mainly produced by oscillation flow in the U-shaped tube. When oscillation occurred along the direction of tube flow, considering the Reynolds number, Kc number, and relative roughness of the cylinder surface, Sarpkaya and Isaacson [27–30] plotted the variation in the curves of the drag coefficient C_D and inertial force coefficient C_M for the oscillation flow of a circular cylinder after numerous experiments under different conditions. They also performed extensive analyses based on changes in the cylinder force and energy transmission. Carberry [31] compared and summarized the advantages and disadvantages of existing forced oscillation tests. They investigated the effect of the Reynolds number on the results of the experimental test when the oscillation is perpendicular to the direction of tube flow. Morse and Williamson [32] confirmed that the fluid force of self-excited vibrations is similar to that of forced oscillation under conditions in which the amplitude, frequency, and Reynolds number are equal. Note that these damping characteristic experiments are only applicable to a cylinder. The damping characteristics differ for orifice plates having a shape other than a circle or square. A similar problem is the vortex-induced vibration in marine engineering [33, 34]. Thus far, few studies have focused on the orifice plate characteristics and optimization damping ratio of TLCDs. In addition, the nonlinear damping term is usually simplified to be linear. Hence, several issues could be studied further: the functional relationship between the head loss coefficient and the orifice plate properties; the degree to which the opening rate and other TLCD parameters affect head loss; and guidelines for quickly adjusting the head loss coefficient to the specified value during engineering practice.

Experimental studies on the damping characteristics of a TLCD can be performed using an offshore engineering model basin or a vibration test system on land. The high construction cost of the former makes it impossible to repeat experiments. In addition, such devices cannot directly control the size of the external force applied to the measured model, and the wave force acting on the structure can only be

indirectly changed by adjusting the wave height and period. Thus, measuring the head loss coefficient of a TLCD on a floating platform model is extremely difficult. An on-land vibration test system is a good alternative because of its low cost and easy control. On the other hand, such systems are always designed for civil structures or machines, which differ from floating platforms in some respects such as natural vibration period, amplitude, and external environment. Because existing onshore test systems cannot effectively and inexpensively simulate the working conditions on a floating platform, it is desirable to design an alternative device with large stroke force control components for simulating large-amplitude motions at low frequency.

Current onshore vibration test systems mainly include electromagnetic vibration and electrohydraulic servo test systems. An electromagnetic vibration test system, which is costly and shows low total harmonic distortion (THD), is mainly used for high-frequency (tens to thousands of Hertz) simulation. Kim et al. [35] optimized the dynamic performance of electromagnetic exciters by using finite element analysis. By using a numerical simulation to design the control scheme for an electromagnetic actuator with a 10 kN load, Li et al. [36] found that high-precision control of the actuator signal could be achieved by adaptive inverse control theory. Zhu et al. [37] designed a new type of micro electromagnetic vibration exciter whose resonance frequency could be controlled without changing the total damping. Oliver and Priya's [38] four-bar magnet geometry increased the output power of the electromagnetic vibration exciter and the accuracy of predicting the optimal load resistance.

The other major type of onshore system is an electrohydraulic servo test system, which produces various types of oscillatory waves through a dynamic loading device and simulates the vibration for an experimental subject on a rigid surface. Despite its speed and high power, its precision is slightly less than that of the electromagnetic vibration test system. Moreover, its running and maintenance costs are quite high. Conte and Trombetti [39] found a potentially strong dynamic interaction between the oil column in the actuator and the payload when their frequencies were similar in a uniaxial servohydraulic shaking table system. Stehman and Nakata [40] used force feedback to ensure stable motion of the shaking table in a perfectly balanced position to optimize acceleration control. Jianjun et al. [41] discussed the use of the least mean square (LMS) adaptive filtering algorithm to control the amplitude and phase of the acceleration signal so as to suppress higher harmonics and reduce distortion [41]. To eliminate adverse effects on the acceleration of vibration control, Dozono et al. [42] introduced adaptive filtering compensation (AFC) to the control theory of shaking tables. To reduce the maintenance and operation cost, Ye et al. [43] invented a pneumatic shaking table that used compressed air instead of electricity as the transmission medium and changed the loading mode from hydraulic to pneumatic actuation. This type of shaking table provides more stable low-frequency harmonic frequencies (above 3 Hz).

An investigation of a shaking table test system reveals that an electromagnetic vibration system is usually used to study the strength and elastoplastic properties of the sample.

Conducting experiments with large displacements is difficult because the maximum amplitude of the electromagnetic vibration system is only 5–35 mm. However, electrohydraulic servo test systems suffer from some drawbacks. The input signal is always the acceleration or displacement, which is seldom loaded directly. Nonlinear factors such as the delay of the servo valve actuator, compression of liquid in the actuator, and closeness of the actuator greatly influence precision, especially for a small electric hydraulic servo vibration system. The distortion of the response curve is a serious impediment to processing experimental data at low frequencies (0.2–1 Hz) because the high-order harmonic generation cannot be eliminated. In this study, the frequency of the shaking table must be 0.5–1.5 Hz to simulate the horizontal movement accurately. Moreover, the maximum displacement amplitude is set above 100 mm to simulate the resonance phenomenon between the shaking table and the TLCD. Hence, conducting experiments with an electrohydraulic servo test system is extremely difficult.

As discussed above, it is challenging to find an available test system simultaneously equipped with large-amplitude motion simulation, low-frequency performance, and large stroke force control. In this study, a vibration test system that satisfies the above requirements is independently designed to achieve harmonic wave force loading based on a small hydraulic shaking table with a custom-made loading system and a device for changing stiffness. In the low-frequency range of 0.5–1.5 Hz, the maximum displacement amplitude is above 100 mm without any high-order harmonic generated during the loading process. The THD is less than 0.5%. According to the experimental data, the head loss coefficient of the nonlinear damping term of the TLCD is calculated based on the energy transmission between the TLCD and the experimental vibration system. The functional relationship between the head loss coefficient and the orifice plate properties or the TLCD's relevant parameters is also investigated. This paper is divided into two parts: the first part describes the rationale for independently designing an available test system with large-amplitude motion simulation, low-frequency performance, and large stroke force control, and the second part discusses the application of a uniform design to determine the functional relationship between the head loss coefficient and the natural frequency of the TLCD, orifice plate parameters, Reynolds number or Kc number in the liquid column of the TLCD, or ratio of the horizontal column to the vertical column. Finally, a type of rapid design strategy is proposed for the TLCD head loss coefficient under working conditions.

2. Design of Experimental System

As noted earlier, a TLCD, a type of passive vibration control device, is widely used in structures such as high-rise buildings. A TLCD suppresses motion in a structure by transferring part of the kinetic energy from the main structure to the liquid column, which causes the latter to undergo severe sloshing and absorb energy. In addition, part of the energy is consumed by damping effects in the TLCD. As shown in Figure 1, L_d is the total length of the liquid column,

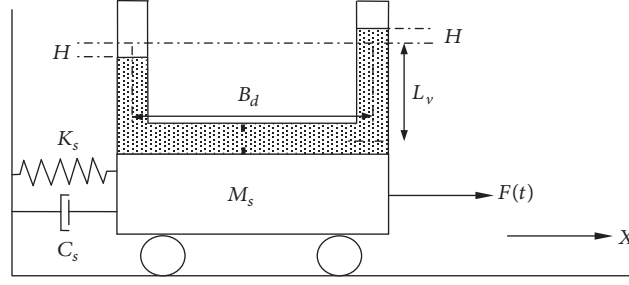


FIGURE 1: Schematic diagram of TLCD.

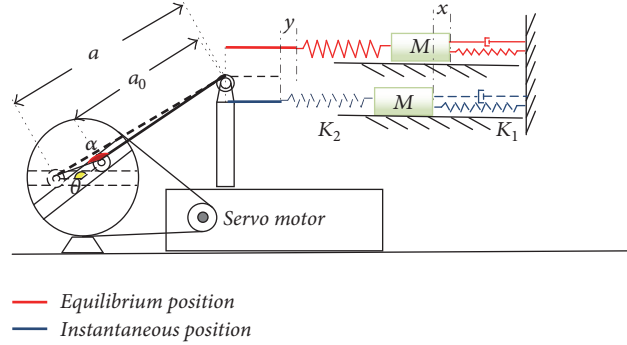


FIGURE 2: Schematic diagram of vibration test system with large motion amplitude and force control.

which can be expressed as $L_d = B_d + 2L_v$; vertical column length is denoted by L_v ; horizontal column length is denoted by B_d ; and head loss coefficient is denoted by h_d . By using the Lagrange equation and energy method, the 2-DOF motion equations of the TLCD fluid column and the main structure are established as follows:

$$\begin{aligned} M_s \ddot{X} + C_s \dot{X} + K_s X &= F(t) - \rho_d A_d B_d \ddot{H} - \rho_d A_d L_d \ddot{X} \\ \rho_d A_d L_d \ddot{H} + \frac{1}{2} \rho_d h_d A_d |\dot{H}| \dot{H} + 2\rho_d g A H & \\ &= -\rho_d B_d A_d \ddot{X}. \end{aligned} \quad (1)$$

Equations (1) show that experimental studies on the TLCD need a force control vibration test system. In addition, for the onshore simulation of a floating platform with the vibration characteristics of the above TLCD, the vibration test system should be capable of large-amplitude motion simulation, low-frequency performance, and large stroke force control. As mentioned earlier, because it is difficult to find a test system that satisfies these requirements, the system is independently designed in this study. Its working principle and design scheme are illustrated in Figure 2.

Figure 2 shows the operational principle of the loading device. Here, K_1 is the equivalent stiffness of the required measured object; K_2 , the stiffness of the extension spring; M , the quality of the required loading object; E , the elastic modulus of the wire rope; A , the cross-sectional area of the wire rope; l_0 , the length of the wire rope between the

extension spring end and the belt pulley; a_0 , the length of the wire rope from the fixed pulley to the slider before starting the device; a , the length of the wire rope from the fixed pulley to the slider at a given time after starting the device; r , the radius of the belt wheel; θ , the instantaneous rotation angle of the belt wheel; α , the angle corresponding to a in a triangle constituted by a , a_0 and the line connecting these two endpoints; x , the displacement of the object under instantaneous rotation; y , the displacement between the extension spring and the fixed pulley under instantaneous rotation; and ω , the rotational frequency of the belt pulley, usually $a_0 > 10r$. After starting the motor, the object moves from the equilibrium position to the instantaneous position. At the same time, the length variation of the wire rope is $a - a_0 - y$. In the triangle constituted by a , a_0 and the line connecting these two endpoints, Taylor expansion is used on the expression for a obtained by the cosine theorem. When $a_0 > 10r$, the higher-order terms are infinitesimal. Keeping the first-order term of the Taylor expansion of a gives

$$a = a_0 + \frac{r^2 + ra_0}{a_0} - \frac{r^2 + ra_0}{a_0} \cos \omega t. \quad (2)$$

When the wire rope is tensed at the equilibrium position, the prestressed forces from the extension spring and the measured object are equal and opposite in sign. The measured object is subjected to the force produced by the deformation quantity of the extension spring at the time of belt pulley turning. The equation of motion for object M can be

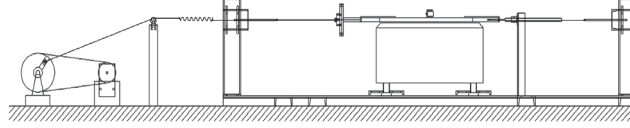


FIGURE 3: Design drawing of experimental installations.

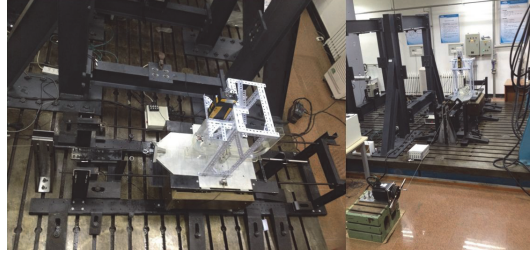


FIGURE 4: Photographs of experimental testing system.

expressed as $M\ddot{x} + C\dot{x} + K_1x = K_2(y - x)$. According to the force equilibrium between the extension spring and the wire rope, y is obtained as follows:

$$\frac{EA(a - a_0 - y)}{l_0} = K_2(y - x) \quad (3)$$

$$y = \frac{EA(a - a_0) + K_2l_0x}{EA + K_2l_0}.$$

At the moment of belt pulley turning, the external force acting on the object is obtained as follows:

$$F = K_2(y - x) = K_2 \left(\frac{1}{1 + K_2/(EA/l_0)} (a - a_0) - \frac{1}{1 + K_2/(EA/l_0)} x \right). \quad (4)$$

Thus, the resulting motion equation forms are expressed as follows:

$$M\ddot{x} + C\dot{x} + Kx = F_0 + F_t \cos \omega t$$

$$K = K_1 + K_2 \frac{EA}{EA + K_2l_0}$$

$$F_0 = \frac{K_2EA}{EA + K_2l_0} \frac{r^2 + ra_0}{a_0} \quad (5)$$

$$F_t = \frac{K_2EA}{EA + K_2l_0} \frac{r^2 + ra_0}{a_0}.$$

The expression for z is given as

$$z = x - \frac{K_2EA}{K_1EA + K_1K_2l_0 + K_2EA} \frac{r^2 + ra_0}{a_0}. \quad (6)$$

Equation (5) can then be simplified as

$$M\ddot{z} + C\dot{z} + Kz = F_t \cos \omega t. \quad (7)$$

Before starting the experiments, pretension should be imposed on the wire rope and extension spring to keep them tightening during the experiments. This test system also simulates the static and displacement loading conditions. When the angle of rotation of the belt pulley is fixed at $\omega t = \pi/2$, the constant external force acting on the object is expressed as

$$F_{\text{Constant}} = \frac{K_2EA}{EA + K_2l_0} \left(\frac{r^2 + ra_0}{a_0} \right). \quad (8)$$

By removing the tension adjusting spring, that is, using the displacement loading method alone, the displacement variation of the object is expressed as

$$x = \frac{r^2 + ra_0}{a_0} + \frac{r^2 + ra_0}{a_0} \cos \omega t. \quad (9)$$

Figure 3 shows a design drawing of the experimental installations and Figure 4 shows photographs of the experimental testing system. The experimental device consists of a servo motor, horizontal shaking table with fixed steel frame, belt pulley groups, and extension spring. The spring connection between the shaking table and the steel frame not only compensates for the lack of stiffness of the shaking table but also converts the table, which originally supplied the vibration environment, into one of the measured objects. When the springs are under tension, the horizontal shaking table shows a reciprocating motion with larger amplitude. The stiffness of the shaking table can be adjusted by simply replacing the springs with those of different stiffness. This experimental device has two loading modes: force and displacement. It can apply an alternating load or a constant load whose amplitude and frequency are adjustable across a large range. A conventional motor can be used as the power supply as long as the running speed is stable. The experimental device is quite small and easy to disassemble. Moreover, the device can be refitted conveniently for different research needs with high precision.

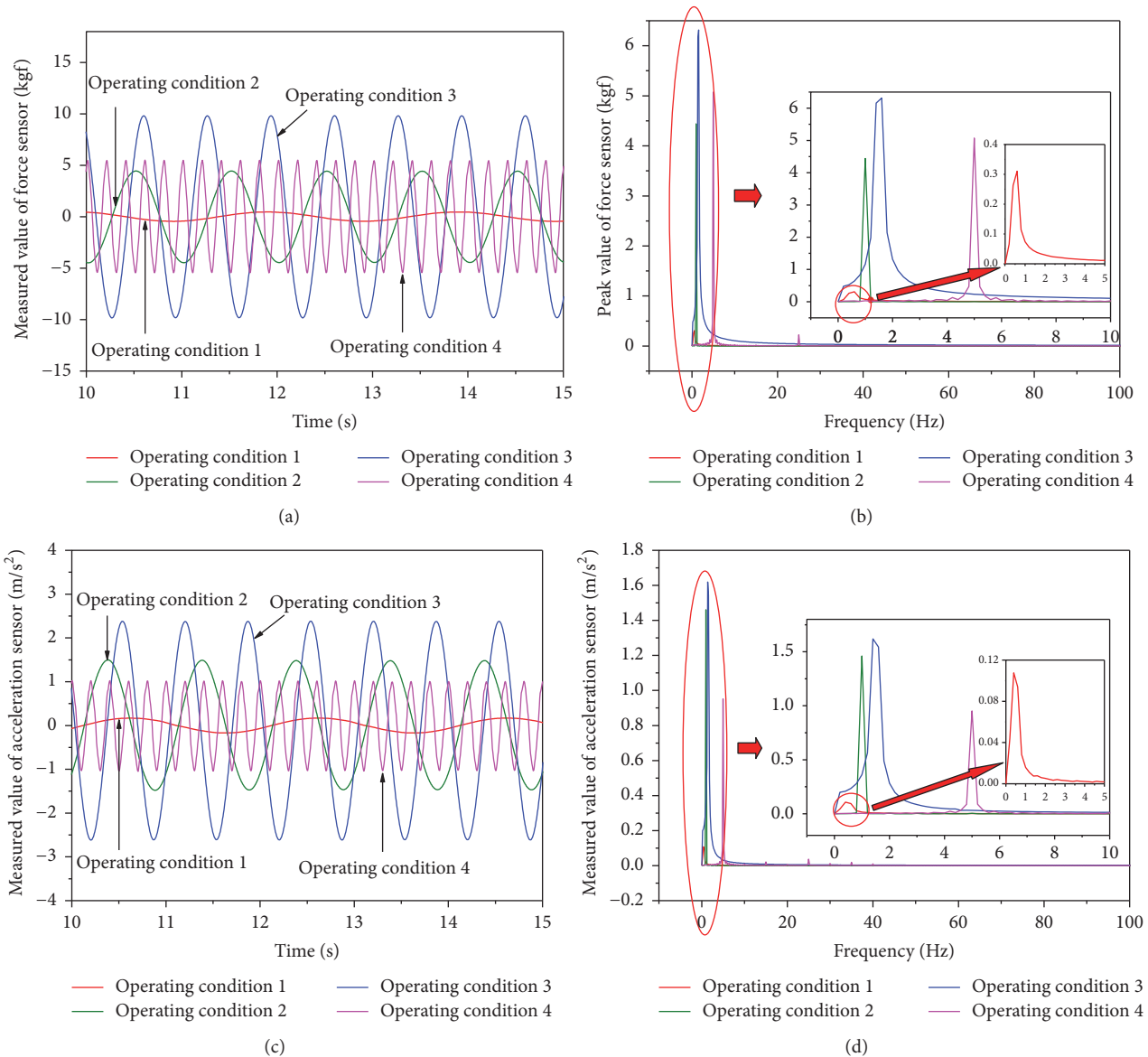


FIGURE 5: Performance test results for (a) force curve, (b) frequency spectrum of force, (c) acceleration curve, and (d) frequency spectrum of acceleration (operating condition 1: stiffness of extension spring, 100 N/m; frequency of harmonic wave, 0.5 Hz; operating condition 2: stiffness of extension spring, 460 N/m; frequency of harmonic wave, 1 Hz; operating condition 3: stiffness of extension spring, 850 N/m; frequency of harmonic wave, 1.5 Hz; operating condition 4: stiffness of extension spring, 640 N/m; frequency of harmonic wave, 5 Hz.).

The loading mode is changed by installing or removing the extension spring. The amplitude of the external load is adjusted by replacing the extension spring with one of different stiffness or by adjusting the position of the slide on the belt pulley. This is also achieved when the length of the wire rope is changed by varying the horizontal spacing or vertical height between the belt pulley and the fixed pulley. With frequency adjustment, the harmonic load signal can satisfy the frequency requirement for various experiments, ranging from low to high. The shaking table in this testing system can also be used as an experimental object. This is unlike the electromagnetic or electrohydraulic servo shaking table, which can only provide vibrations.

The results obtained from this experimental testing system are first verified. Figures 5(a)–5(d) show the force curve and acceleration curve and their corresponding frequency spectra under four operating conditions (different extension spring and total stiffness), with the frequency of the oscillatory system ranging from 0.5 to 5 Hz (sampling frequency: 204.8 Hz). The acceleration and force signals are obtained by the sensors installed on the shaking table. This shows that the high-order harmonic does not exist in the actual curve of the waveform at low frequency. In the frequency range of 0.5–5 Hz, in particular, the harmonic curve is so smooth that its accuracy satisfies the expected requirement. The waveform rapidly reaches the steady state because uncontrollable factors

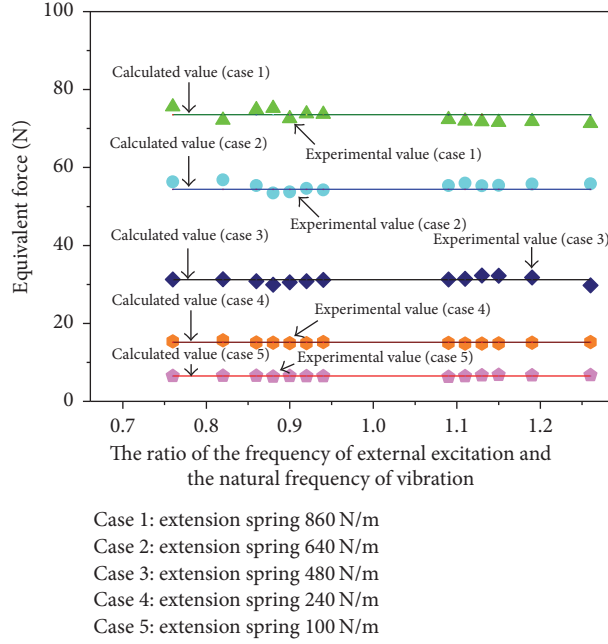


FIGURE 6: Comparison of equivalent forces with different extension springs and frequencies.

and nonlinear problems of parameters in the experimental test system have little influence on it.

Because the loading device moves with the shaking table during the operation of the vibration test system, further treatments of the experimental data are required to determine the equivalent force. Figure 6 shows a comparison between the actual equivalent force and the computed value obtained with a different loading device and extension spring. (The average equivalent force is the mean of the equivalent forces under different motor frequencies.) Under the same loading device and extension spring, the equivalent forces of the harmonic load with various frequencies are relatively constant. The maximum error of the equivalent force at a certain frequency is less than 5%; therefore, the basic experimental requirement is satisfied.

3. Analysis of TLCD Damping Characteristics

For a certain frequency band, the relevant parameters of the TLCD damping characteristics must be adjusted to achieve a good damping effect on the main structure (i.e., a smaller response and more stabilized vibration range). Owing to the characteristics of the overall and cross-sectional geometries of the TLCD, inherently nonlinear fluid damping mainly consists of head loss induced by the orifice plate, turn elbow, and, even more so, viscous damping of the shaking table. Because it is complicated to calculate each part of the damping separately, the total head loss coefficient of the TLCD is normally adopted. According to (1), the damping characteristics of the TLCD are mainly reflected in the damping force term, which is proportional to the square of the velocity and expressed as $(1/2)\rho_d A_d h_d |\dot{H}|\dot{H}$. The key parameter of the damping characteristics for a TLCD is the

head loss coefficient h_d , which has been investigated in only a few studies. In published literature, the head loss coefficient was always measured and analyzed after the nonlinear damping term was transformed into the equivalent damping or linear damping term. Moreover, quantitative relationships between the head loss coefficient and other parameters of the TLCD have not yet been characterized. These problems will be studied here.

Figure 7 shows a photograph of the experimental setup. The large-amplitude loading system described in the preceding paragraph was used. Moreover, a portable digital vibrometer (PDV), which was mounted on the shaking table and fixed by a holder, could measure the axis velocity of the liquid column along the TLCD with the catopter created through light and thin floating slices or special reflective material. To analyze orifice plates of different sizes, a flange, made in the middle of the horizontal column of the TLCD, was used to change the orifice plate fixed by screws.

We assume that ρ is the liquid density; v , the axis velocity of the liquid column along the TLCD; D , the diameter of the column in TLCD; D_0 , the diameter of the orifice plate; L , the total length of the liquid column; L_h , the horizontal length of the liquid column; ν , the kinematic viscosity of the liquid; and T , the period of liquid movement in the TLCD. Regardless of the variation of free surface in the liquid column and the wall effect of the column, the fluid resistance during the oscillation of liquid flow is described using these parameters:

$$F = f(\rho, v, D, D_0, L, L_h, \nu, T). \quad (10)$$

Among the nine variables in (10), ρ , v , and D are chosen as the independent variables. According to dimensional analysis, the oscillation flow force is transformed to the

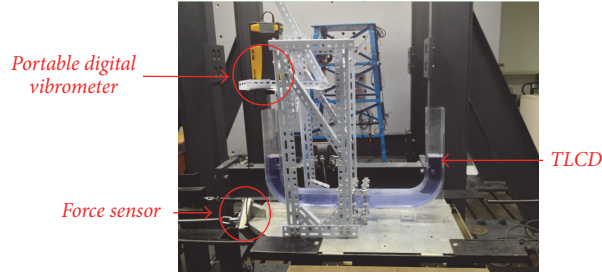


FIGURE 7: Testing device for TLCD.

dimensionless form $F/(\rho V^2 D^2)$. Therefore, (10) is rearranged to the following dimensionless form:

$$\frac{F}{(\rho V^2 D^2)} = f\left(\frac{D_0}{D}, \frac{L}{D}, \frac{L_h}{L_v}, \frac{\nu}{VD}, \frac{VT}{D}\right). \quad (11)$$

In (11), D_0/D represents the opening rate of the orifice plate; L/D , the shape of the vertical and horizontal liquid columns where the total length is associated with the natural period of the TLCD; and L_h/L_v , the ratio of the length between the vertical and the horizontal columns, which reflects the damping effect of the elbow in the TLCD. $Re = VD/\nu$ and $K_c = VT/D$ are the Reynolds number and Keulegan–Carpenter number of the fluid, respectively.

The head loss coefficient in the TLCD is mainly determined based on the resistance part of the oscillatory flow force. The experiments are designed to identify the relationship between the head loss coefficients and other factors. The acceleration and displacement of the main structure are determined by sensors installed on the shaking table. The equivalent harmonic force of the main structure's movement is calculated by the harmonic tension measured by a force sensor. The speed of the liquid column in the TLCD is obtained by a PDV measuring the speed at the center of the liquid surface of the vertical liquid column. The experimental result for the head loss coefficient of the TLCD is obtained by using the analysis of energy method.

The shaking table with a TLCD generates a simple harmonic motion upon being driven by the motor. In a large-amplitude loading system, energy loss is inevitable; therefore, it is a nonconservative system. The total energy consumption S_{total} caused by system damping is divided into two components: the energy consumption caused by internal fluid movement of the TLCD, S_{TLCD} , and the energy consumption caused by the viscous damping of the shaking table, $S_{\text{structure}}$. The total energy consumption in one motion cycle is expressed as

$$S_{\text{total}} = \int_0^T F \dot{x} dt. \quad (12)$$

Here, F is the equivalent harmonic force; in addition, \dot{x} is the speed of the vibration table, obtained by integrating acceleration against time. The damping energy consumption

caused by the viscous damping of the shaking table is expressed as

$$S_{\text{structure}} = \int_0^T C \dot{x} \cdot \dot{x} dt, \quad (13)$$

where $C = 2m_s \omega_s \xi$ is the total quality and ξ is the viscous damping ratio of the shaking table. The viscous damping ratio has been obtained by experimental measurement using the free vibration attenuation method. The damping value of the hydraulic shaking table is low, so the viscous damping ratio can be calculated as $\xi = \ln(v_n/v_{n+m})/2\pi m_s$, where v_n is the displacement amplitude and v_{n+m} is the displacement amplitude after m period of motion. With the calculation of experimental data, the viscous damping ratio of this shaking table system is 0.046 (parameters for testing system: $m_s = 76$ kg; $k_s = 1180$ N/m). In one movement cycle, the energy consumption caused by the TLCD is expressed as

$$S_{\text{TLCD}} = \int_0^T \frac{1}{2} \rho A_d h_d |\dot{H}| \dot{H} \cdot \dot{H} dt, \quad (14)$$

where ρ is the liquid density; A_d , the cross section of the liquid column; and \dot{H} , the axial velocity of the liquid column surface. The basic principles of energy consumption are given as

$$\int_0^T F \dot{x} dt = \int_0^T C \dot{x} \cdot \dot{x} dt + \int_0^T \frac{1}{2} \rho A_d h_d |\dot{H}| \dot{H} \cdot \dot{H} dt. \quad (15)$$

Therefore, the head loss coefficient is expressed as

$$h_d = \frac{\int_0^T F \dot{x} dt - \int_0^T C \dot{x} \cdot \dot{x} dt}{\int_0^T (1/2) \rho A_d |\dot{H}| \dot{H} \cdot \dot{H} dt}. \quad (16)$$

The head loss coefficient is thus calculated by (16). Many parameters can be directly measured using the experimental instruments. The speed of the vibration table is obtained by integrating the acceleration. The structural damping ratio of the shaking table is measured by attenuating the free vibrations. The experimental data are analyzed based on the regression equation. (Data acquisition instruments are manufactured by the China Orient Institute of Noise and Vibration.)

TABLE I: Experimental scheme and measured data.

Experiment number	Total length of liquid column	Opening ratio	Reynolds number	Kc number	Length of horizontal liquid column	Velocity of vertical liquid column V (mm/s)	Motor speed (r/min)	Head loss coefficient
	x_1	x_2	x_3	x_4	x_5			
N1	19.5	0.6	9615.38	8.5	13.67	238.37	32	6.7
N2	19	0.7	10538.5	7.9	13.67	241.88	32.4	4.73
N3	20	0.5	10307.7	6.7	12.33	279.87	52.3	28.53
N4	18	0.5	9615.38	7.3	13.00	261.07	44.82	25
N5	18	0.6	10076.9	7.9	12.33	249.81	36.18	8.6
N6	18	0.4	10538.5	6.1	11.67	320.09	73.56	40.8
N7	19	0.3	10076.9	6.7	13.00	353.10	85.23	73.9
N8	17.5	0.8	10538.5	5.5	12.33	226.22	40.75	2.86
N9	19	0.4	9846.15	7.9	11.67	299.07	53.07	42.5
N10	20	0.4	10538.5	7.9	13.00	320.09	56.8	40.07
N11	18	0.6	10769.2	6.7	13.67	266.97	45.59	7.57
N12	18.5	0.4	9846.15	5.5	13.67	299.07	76.23	37.75
N13	18.5	0.8	9615.38	6.7	11.67	206.41	30.52	3.14
N14	20	0.8	10076.9	6.1	13.67	216.31	35.13	3.83
N15	19.5	0.7	10769.2	7.3	11.67	247.18	35.87	5.07
N16	18.5	0.3	10769.2	8.5	12.33	377.36	71.79	73.2
N17	20	0.7	9846.15	7.3	12.33	225.99	32.8	5.87
N18	17.5	0.3	10307.7	7.3	13.67	361.19	80.02	62.1
N19	19.5	0.5	10769.2	5.5	13.00	292.40	66.62	28.7
N20	17.5	0.7	9846.15	6.1	13.00	225.99	39.24	4.95
N21	19	0.6	10307.7	5.5	11.67	255.53	53.16	6.07
N22	17.5	0.5	10076.9	8.5	11.67	273.60	40.34	22.3
N23	17.5	0.8	9615.38	5.5	11.67	206.40	31.36	2.2
Diameter of circular orifice	Opening ratio of orifice = 0.3		Opening ratio of orifice = 0.4		Opening ratio of orifice = 0.5	Opening ratio of orifice = 0.6	Opening ratio of orifice = 0.7	Opening ratio of orifice = 0.8
	37.1 mm		37.1 mm		47.88 mm	52.44 mm	56.64 mm	60.56 mm
TLCD model	Original total length		Original horizontal length		Side length of cross section			
	140 cm		60 cm		6 cm			

To investigate the relationship between the oscillating force and the dimensionless terms, a series of experiments needs to be carefully designed. Uniform design [44, 45] refers to a method of experimental design that considers the distribution of test points to be even within the scope of the test. By using this method, the number of multifactor experiments can be reduced by simply recording a data sheet. The regression analysis of experimental data (e.g., quadratic polynomial regression analysis) could then be applied. The final optimal design scheme of the TLCDC will be determined by discussing the influence of various factors on the experimental model.

Table 1 shows an experimental scheme according to the basic principle of uniform design. The head loss coefficients are treated as indices in the regression analysis. After obtaining the experimental result, all parameters of the factors

should be normalized within their own value range. The regression equation obtained from a quadratic polynomial stepwise regression analysis is expressed as follows:

$$\begin{aligned}
Y = & 1.761 - 9.82x_1 - 35.804x_2 - 33.475x_3 \\
& + 13.190x_4 + 26.140x_5 + 28.156x_1^2 + 127.908x_2^2 \\
& + 32.940x_3^2 + 12.713x_4^2 - 14.683x_5^2 \\
& + 26.691x_1x_2 - 3.183x_1x_3 - 37.106x_1x_4 \\
& - 17.688x_1x_5 - 13.278x_2x_3 - 37.871x_2x_4 \\
& - 28.436x_2x_5 + 10.349x_3x_4 + 0.388x_3x_5 \\
& + 12.901x_4x_5.
\end{aligned} \tag{17}$$

TABLE 2: Partial correlation analysis of regression coefficient.

	Partial correlation coefficient	<i>t</i> -value	<i>P</i> value
$r(y, x_1)$	-0.873	2.534	0.0551
$r(y, x_2)$	-0.976	6.387	0.0078
$r(y, x_3)$	-0.982	7.280	0.0053
$r(y, x_4)$	0.903	2.971	0.059
$r(y, x_5)$	0.984	7.834	0.0043
$r(y, x_1^2)$	0.967	5.336	0.0129
$r(y, x_2^2)$	0.997	19.749	0.0003
$r(y, x_3^2)$	0.981	7.156	0.0056
$r(y, x_4^2)$	0.903	2.964	0.0593
$r(y, x_5^2)$	-0.953	4.421	0.0215
$r(y, x_1x_2)$	0.955	4.548	0.0199
$r(y, x_1x_3)$	-0.535	0.895	0.4367
$r(y, x_1x_4)$	-0.977	6.427	0.0076
$r(y, x_1x_5)$	-0.951	4.337	0.0226
$r(y, x_2x_3)$	-0.926	3.470	0.0403
$r(y, x_2x_4)$	-0.976	6.344	0.0079
$r(y, x_2x_5)$	-0.983	7.521	0.0049
$r(y, x_3x_4)$	0.907	3.050	0.0554
$r(y, x_3x_5)$	0.107	0.1528	0.8882
$r(y, x_4x_5)$	0.951	4.357	0.0223

Based on quadratic polynomial regression analysis, the following parameter values are obtained: *F*-value of regression analysis, 535.12; significance level, $P = 0.019$; Durbin-Watson statistic, 2.28551390; correlation coefficient after adjustment, $R_a = 0.9998$. Because all statistical indices meet the basic requirements for establishing the regression analysis model, the quadratic polynomial regression equation can be applied. By using the partial correlation analysis of the regression coefficient, the correlations thus obtained are tabulated in Table 2. The *P* values for x_1x_3 and x_3x_5 are much higher than 0.05; this indicates that neither should be included in the subsequent analysis. In other words, the interaction between the total length of the liquid column and the Reynolds number and that between the horizontal length of the liquid column and the Reynolds number have very little effect on the head loss coefficient. As shown in Table 2, single factors such as the opening rate (x_2, x_2^2), Reynolds number (x_3, x_3^2), and horizontal length of liquid column (x_5) and certain interactions such as those between the length of liquid column and the Kc number (x_1x_4), the opening rate and the Kc number (x_2x_4), and the opening rate and the horizontal length of liquid column (x_2x_5) significantly influence the head loss coefficient.

To determine the reliability of (17), five sets of experimental parameters with different combinations were randomly selected. Table 3 shows the corresponding head loss coefficients obtained in the quadratic polynomial regression equation. The head loss coefficients calculated by the regression equation are in good agreement with those obtained from the experimental results. Therefore, the quadratic polynomial

regression equation can be used as the prediction equation within the scope of the experimental parameters.

To analyze the influence of various factors on the TLCD head loss coefficient more precisely, the interactions among these factors should also be considered in addition to the main effects of individual factors. By using the prediction equation within the scope of experimental parameters, parameter combinations for the head loss coefficient (e.g., Kc number–total length of liquid column–horizontal length of liquid column, opening rate–Reynolds number–Kc number, and total length of liquid column–opening rate–horizontal length of liquid column) are shown as a set of curved surfaces in Figures 8–10. For convenience of analysis, three groups of curves that reflect the impact of any two factors on the head loss coefficient are obtained by keeping another factor constant. According to the partial correlation analysis of the regression equation, terms whose *P* values are much higher than 0.05, such as x_1x_3 (interaction of opening rate and Reynolds number) and x_3x_5 (interaction of Reynolds number and horizontal length of liquid column), are not considered in the following analysis.

Figure 8 shows the head loss coefficient as a function of the Kc number, total length of liquid column, and horizontal length of liquid column, with other damper parameters kept constant ($x_2 = 0.5$ and $x_3 = 10191.9$). Figure 8(a) shows a three-dimensional plot of the head loss coefficient as a function of the total length of liquid column and Kc number at $x_5 = 11.67$ –13.67. Figure 8(b) shows the head loss coefficient as a function of Kc number and total length of liquid column at $x_5 = 12.67$. Figure 8(c) shows the influence of Kc number and horizontal length of liquid column on the head loss coefficient at $x_1 = 18.75$. Figure 8(d) shows the head loss coefficient as a function of the total length of liquid column for different horizontal lengths of liquid column at $x_4 = 7.0$. Figure 8(b) shows that the head loss coefficient ranges from 14.55 to 38.7 under the combined effect of both Kc number and total length of liquid column. As shown in Figure 8(c), under the interaction of the Kc number and the horizontal length of liquid column, the head loss coefficient varies from 7.0 to 23.2. In Figure 8(d), the head loss coefficient varies from 7.1 to 29.1 under the combined action of total and horizontal lengths of the liquid column. Therefore, the combined effect of Kc number and total length of the liquid column has the largest influence on the head loss coefficient.

Figure 8(b) shows that the head loss coefficient varies with different Kc numbers and total lengths of liquid column. When the total length of the liquid column is less than 17.5, the curve increases monotonically with the Kc number. Between 17.5 and 19.5, the functions are parabolic curves whose rising limb lengthens and falling limb shortens as Kc increases. Above 19.5, the head loss coefficient decreases monotonically with the Kc number. Among all monotonically decreasing curves, the spacing between curves and the gradient of the curve gradually increase with the total length of liquid column. In contrast, for monotonically decreasing curves, the gradient of the curve gradually decreases with the total length of liquid column.

Figure 8(c) shows that the vertex of the parabola shifts toward lower Kc numbers. As the horizontal length of liquid

TABLE 3: Comparison of head loss coefficients calculated by regression equation and experimental results.

x_1 (mm)	x_2	x_3	x_4	x_5	Experimental head loss coefficient	Numerically calculated head loss coefficient	Error
113	0.3	9615.3	8.3	74	82.61	79.91	3.27%
120	0.5	9846.2	7.0	74	21.33	22.3	4.69%
118	0.4	10384.6	6.5	78	45.72	47.96	4.90%
116	0.6	10000.0	7.9	70	9.50	9.97	4.71%
125	0.3	10538.5	7.5	70	86.59	89.9	3.82%

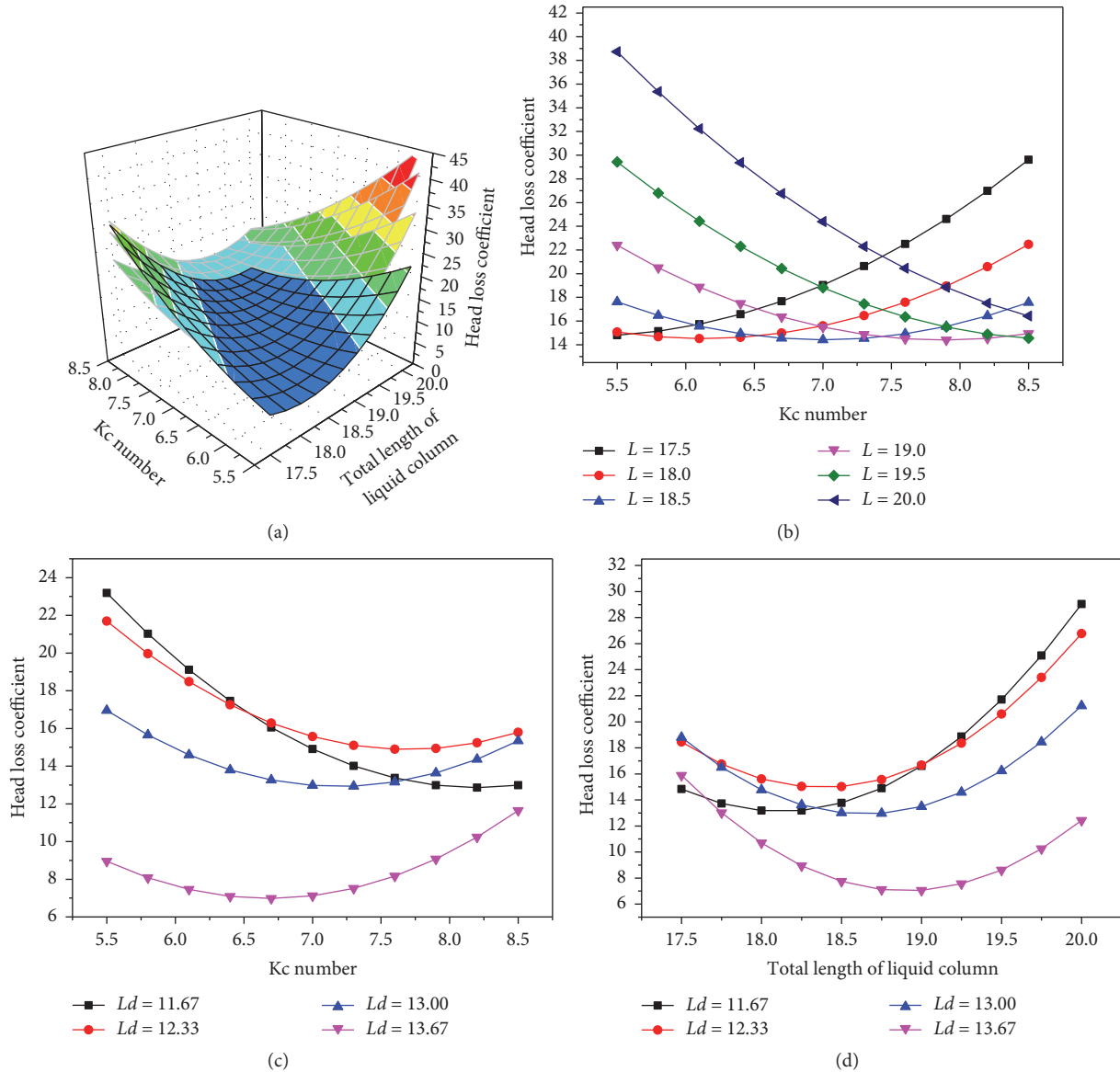


FIGURE 8: Relation schema of Kc number–total length of liquid column–horizontal length of liquid column.

column increases, the falling limb shortens and its gradient decreases, whereas the rising limb lengthens and its gradient increases. When the horizontal liquid column exceeds 13, the change in gradient is not apparent.

In Figure 8(d), the total length of liquid column at the vertex of the head loss coefficient parabola increases with the horizontal liquid column. In addition, the gradient of the descending part of the parabola decreases, whereas that of

ascending part of the parabola increases. A comparison of Figures 8(c) and 8(d) shows that the head loss coefficients are low when the horizontal length of the liquid column reaches 13.67, regardless of the effect of the Kc number or total length of liquid column.

In general, the combined effect of the Kc number and total length of liquid column has large effects on the head loss coefficient. Because the partial correlation analysis described

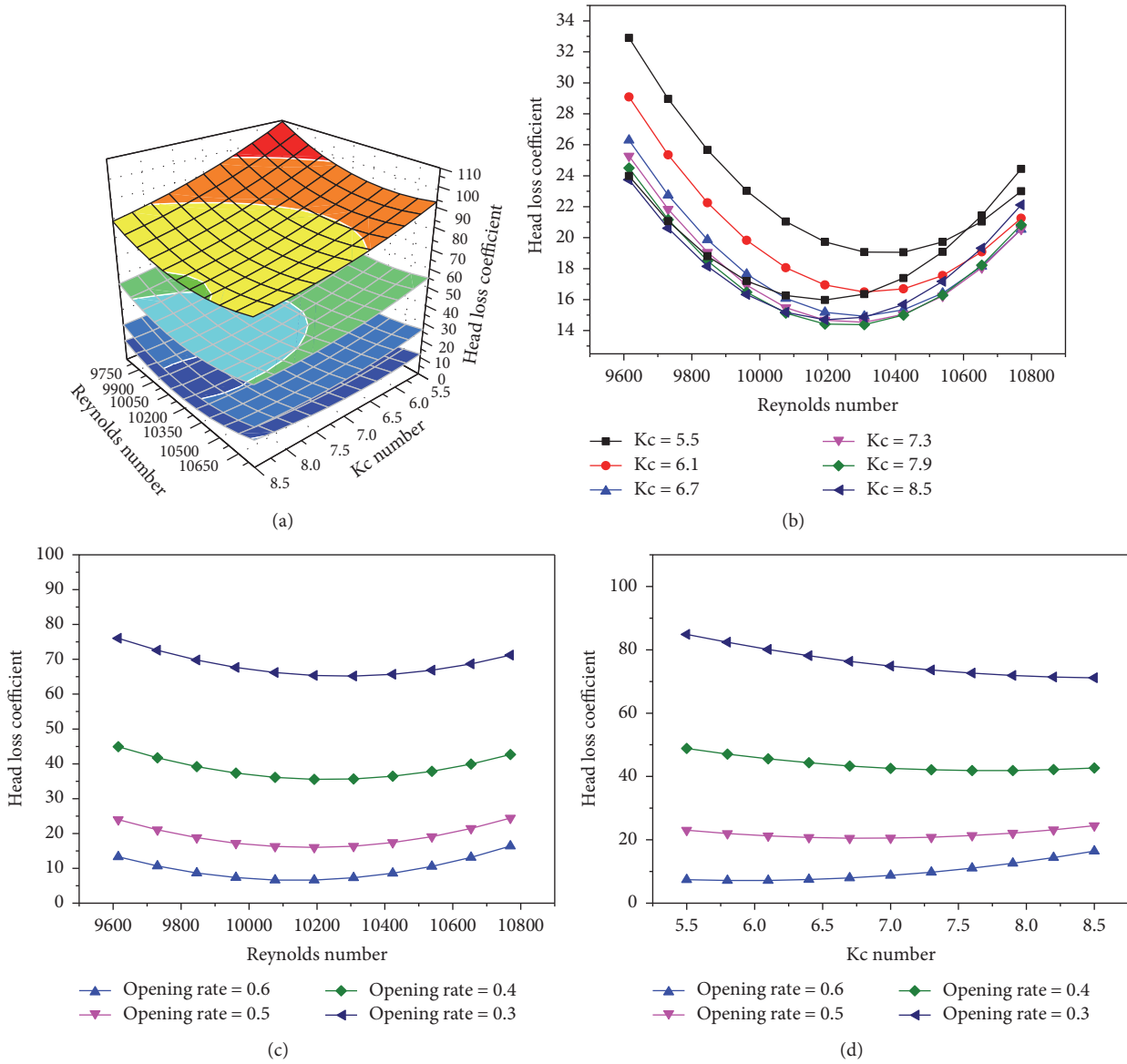


FIGURE 9: Relation schema of opening rate-Reynolds number-Kc number.

above shows that the direct influence of the other two factors is very small, the interaction has large effects on the head loss coefficient.

Figure 9 shows the head loss coefficient as a function of the opening rate, Reynolds number, and Kc number, with other damper parameters kept constant ($x_1 = 18.75$ and $x_5 = 12.67$). Figure 9(a) shows a three-dimensional plot of the head loss coefficient as a function of the Reynolds number and Kc number at $x_2 = 0.3, 0.4, 0.5,$ and 0.6 . Figure 9(b) shows the head loss coefficient for different Reynolds numbers and Kc numbers at $x_2 = 0.6$. Figure 9(c) shows the influence of the opening rate and Reynolds number on the head loss coefficient with $x_4 = 8.5$. Figure 9(d) shows the head loss coefficient as a function of the Kc number for different opening rates at $x_3 = 10191$.

As shown in Figure 9(b), when the Kc number increases, the vertex of the curve approaches low Reynolds numbers. In the range of 5.5 to 6.7, the gradients of the curves are similar. In contrast, when the Kc number exceeds 7.3, the gradient of the rising limb increases whereas that of the falling limb decreases.

As shown in Figure 9(c), the spacing between curves decreases with the opening rate, whereas the curvature and vertex of the curve are almost identical. With regard to the analysis shown in Figure 9(b), the curve for Kc = 8.5 in Figure 9(b) is the same as that for opening rate = 0.5 in Figure 9(c). When the Kc number changes from 8.5 to 5.5 in Figure 9(b), the head loss coefficient increases by 37% from 24.0 to 32.9 at the point of $Re = 9615$. When the opening rate decreases from 0.5 to 0.4 in Figure 9(c), the head loss

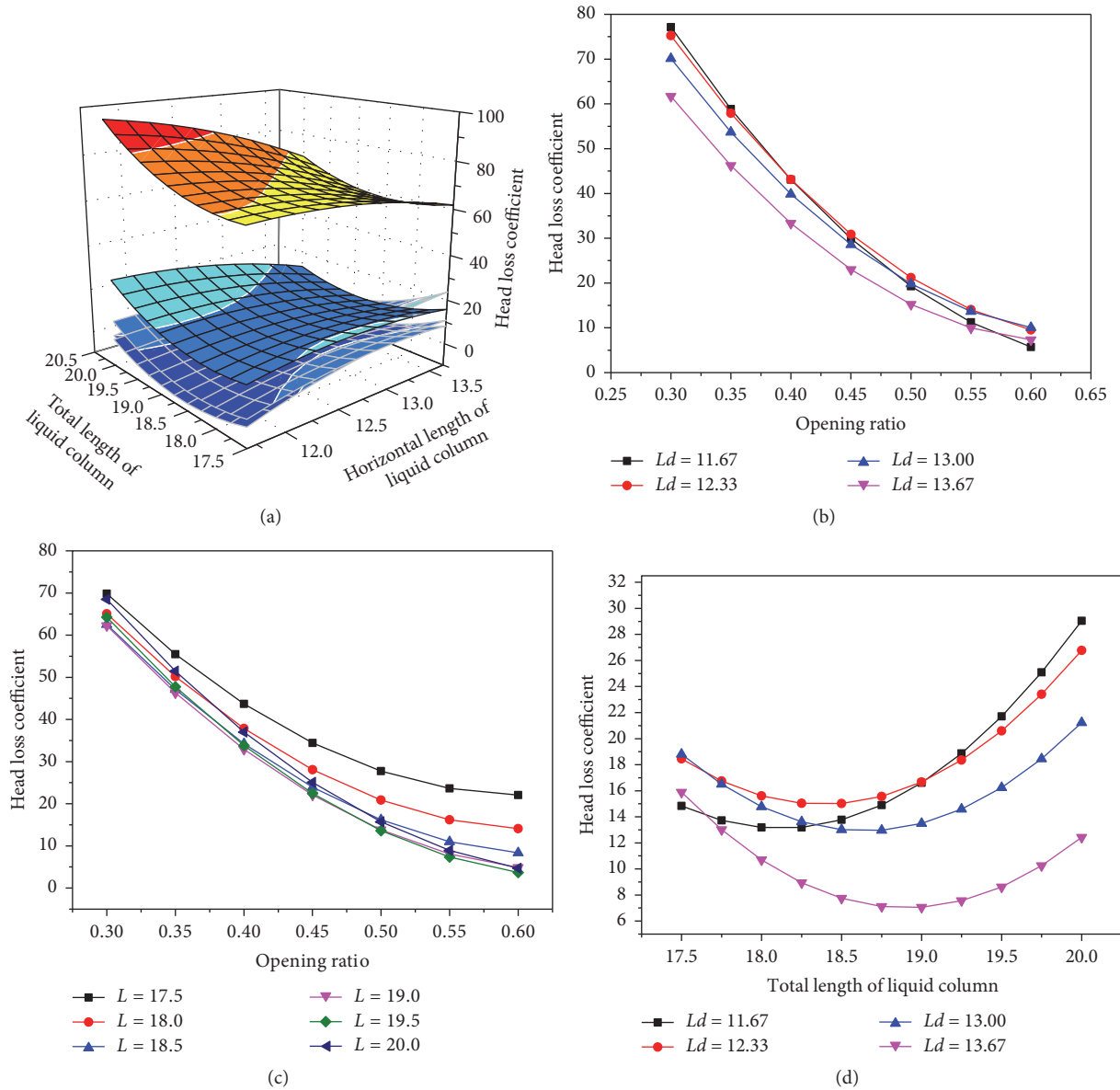


FIGURE 10: Relation schema of total length of liquid column–opening rate–horizontal length of liquid column.

coefficient increases by 87% from 24.0 to 44.9 at the same point. This comparison shows that even when the rate of increase for the Kc number becomes maximal (i.e., $8.5 - 5.5 = 3$), the effect of the Kc number is still less than that of the opening rate (rate of increase = $0.5 - 0.4 = 0.1$) on the head loss coefficient. Therefore, the head loss coefficient is more sensitive to the opening rate.

The curve spacing in Figure 9(d) changes similarly to that in Figure 9(c). In addition, the falling limb of the curve shortens and the rising limb lengthens as the opening rate increases. A comparison of Figures 9(c) and 9(d) shows that, within the experimental range of the Reynolds number, the curve spacing in Figure 9(c) remains almost unchanged, whereas that in Figure 9(d) decreases as the Kc number increases. In other words, the gradient change of the head loss

coefficient as a function of the Reynolds number is greater than that as a function of the Kc number.

Figure 9 therefore shows that the opening rate has a much larger effect than other factors on the head loss coefficient. Among all two-factor combinations shown in Figure 9, the combined effect of the Kc number and the opening ratio is relatively large. However, the simple effect of the opening ratio is such that the combination effect could not alter the monotonically increasing trend of the head loss coefficient as a function of the opening ratio.

Figure 10 shows the relationship of the head loss coefficient plotted against the total length of liquid column, opening ratio, and horizontal length of liquid column, with other damper parameters kept constant ($x_3 = 10537$ and $x_4 = 7.9$). Figure 10(a) shows a three-dimensional plot of the

head loss coefficient as a function of the total length of liquid column and horizontal length of liquid column at $x_2 = 0.3, 0.4, 0.5,$ and 0.6 . Figure 10(b) shows the head loss coefficient as a function of the opening ratio and horizontal length of liquid column at $x_1 = 109.5$ cm. Figure 10(c) shows the influence of the total length of liquid column and opening ratio on the head loss coefficient at $x_5 = 79.6$ cm. Figure 10(d) shows the head loss coefficient as a function of the total length of liquid column for different horizontal lengths of liquid column at $x_4 = 7.0$ (discussed in the preceding paragraph). Figure 10(b) shows that the curves with different lengths of horizontal liquid column all monotonically decrease, with a gradient that continuously decreases as the opening ratio increases. Moreover, at the same opening ratio, the gradient of the curve decreases with the length of the horizontal liquid column. Similar to Figure 10(b), the gradient of the curve shown in Figure 10(c) also decreases as the opening ratio increases, but at a quicker rate. A comparison of Figures 10(b) and 10(c) shows that when the opening ratio is small, the combined effect of the opening ratio and horizontal length of liquid column has a dominant influence on the head loss coefficient. In contrast, when the opening ratio is large, the combined effect of the opening ratio and total length of liquid column dominates. Furthermore, the curve spacing in Figure 10(c) decreases as the opening ratio increases.

Figures 8–10 suggest that the main effect of the opening ratio is larger than that of the remaining two factors. When the opening ratio is large, the combined effect of the opening ratio and total length of liquid column becomes dominant on the head loss coefficient. When the opening ratio is small, the combined effect of the opening ratio and horizontal length of liquid column has a greater influence.

In conclusion, the opening ratio has the largest single impact on the head loss coefficient compared with other factors such as the total length of liquid column, Reynolds number, Kc number, and horizontal length of liquid column. In addition, the main effects of the Reynolds number and horizontal length of liquid column have the next largest impact, whereas the individual effects of the total length of liquid column and Kc number are the weakest. However, the combined effects among all factors also influence the head loss coefficient. The combined effect of the total length of liquid column and Kc number and that of the opening ratio and Kc number greatly influence the head loss coefficient, especially the first combination. During experiments, the head loss coefficient monotonically decreases as the opening ratio increases, regardless of the influence of the other factor.

4. Verification of Mitigation Performance under Seismic Loads and Rapid Design Strategy for TLCD Head Loss Coefficient

The motions of structures under stochastic loads need to be suppressed in practical engineering. The performance of the test system used in previous section, which is equipped with a TLCD with different head loss coefficient, is verified

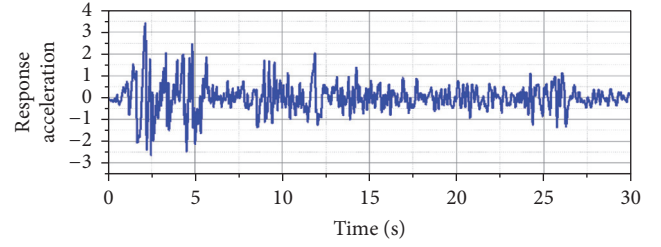


FIGURE 11: EI-Centro earthquake record.

by numerically analyzing the structure-TLCD system under a set of recorded earthquake ground motions. As shown in Figure 11, El-Centro earthquake record (1940) is applied as an input excitation signal with Peak Ground Acceleration (PGA) 0.348 g, the first dominant frequency is 1.1 Hz, and almost three thousand time intervals among the dynamic responses under this specific excitation are employed to train the data. The parameters for testing system are the same as these in Section 3. The mass ratio between the structure and a TLCD is 5%. Figure 12(a) shows the time history responses of the test structure are controlled by the TLCD. The vibration amplitudes obtained from Fast Fourier Transform (FFT) are shown in Figure 12(b). The structural displacements have been largely reduced by the TLCD in Figure 12. A TLCD with smaller value of head loss coefficient has higher mitigation effect than that with the big one. The value of the head loss coefficient has a great influence on the mitigation effect. It is confirmed that the TLCDs used in practical engineering need to choose an optimal head loss coefficient. So the rapid design strategy for the TLCD head loss coefficient must be proposed.

In order to propose the rapid design strategy for the TLCD head loss coefficient also adapting to structures under seismic loads, some key parameters should be further analyzed. Figure 13 shows the relation schema of displacement ratio between controlled structure and uncontrolled structure with different L_N/L_d and B_d/L_d . For these comparative analyses, the head loss coefficient is invariable, 2.5. L_N is the total length of a test TLCD. The displacement ratio is the ratio between the standard deviation of uncontrolled structures and the standard deviation of controlled structures. The displacement ratio reduced with the rising of the L_N/L_d , when the value of L_N is smaller than that of L_d , as shown in Figure 13(a). The rule is on the contrary for the bigger value of L_N . It is unworthy to change the total length of liquid column far from the one corresponding to the main frequency. For the evaluation of the horizontal length of liquid column, it is better to adopt a larger value, as shown in Figure 13(b). The relationship of each key parameter for test structures under seismic loads is also consistent with the relation schema in Section 4.

In real engineering projects, the head loss coefficient should be adjusted frequently to suppress the motion of the main structure more effectively. Because the head loss coefficient is affected by the total length of liquid column, opening ratio, Reynolds number, Kc number, and horizontal length of liquid column, the large number of combinations among

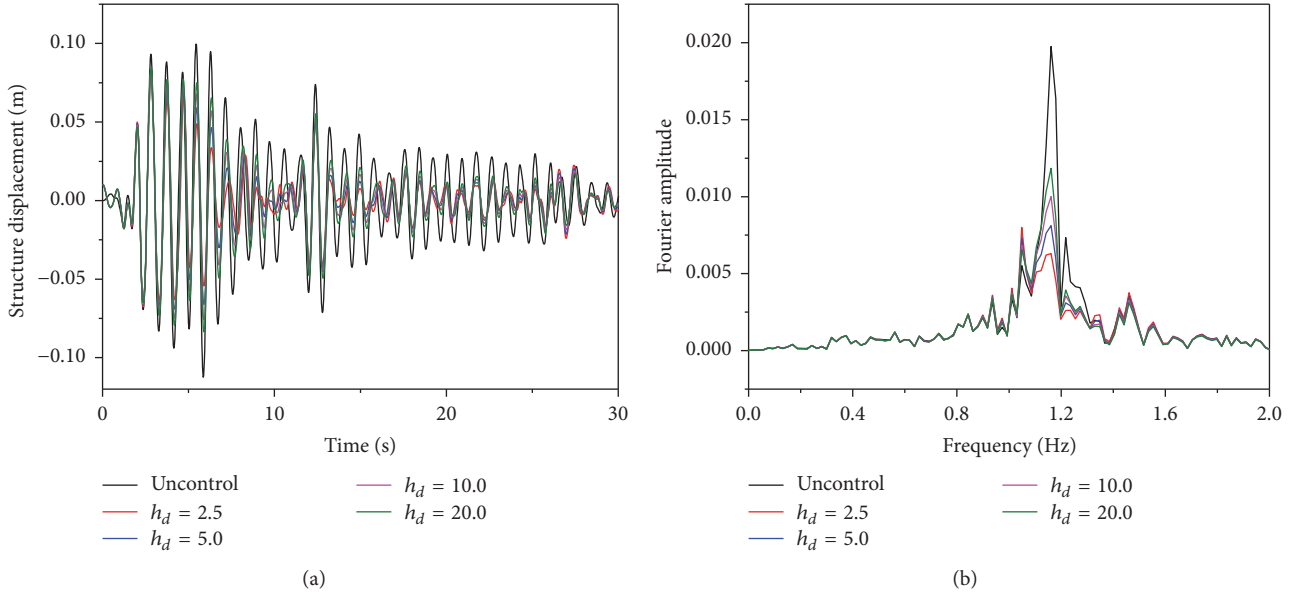


FIGURE 12: Comparison of mitigation effects with different head loss coefficient for (a) time histories of the structure displacement and (b) Fourier amplitude of the structure response.

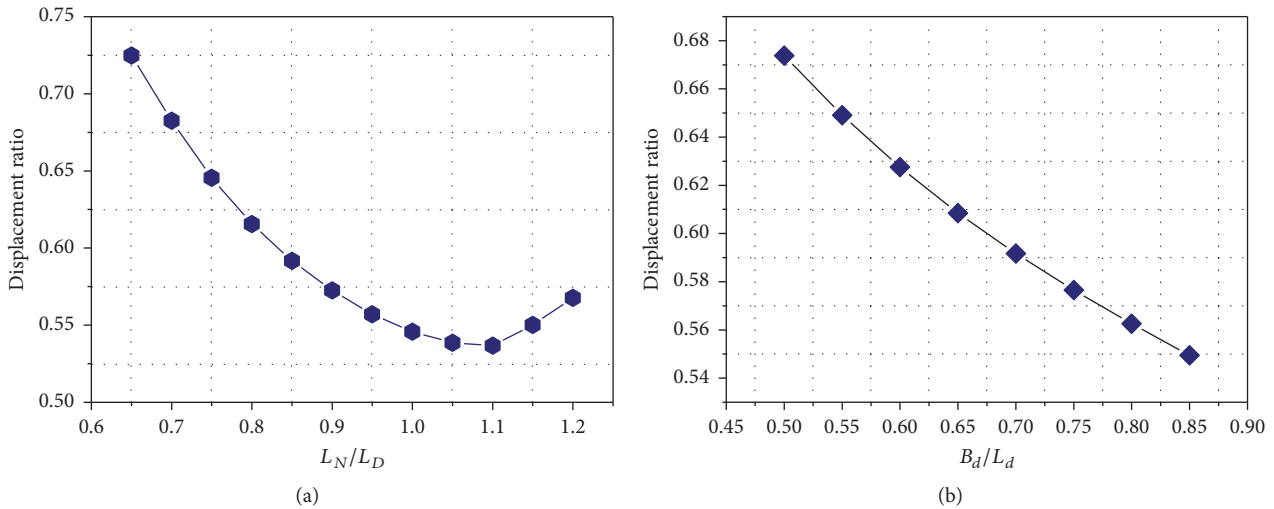


FIGURE 13: Relation schema of displacement ratio between controlled structure and uncontrolled structure.

these factors makes it difficult and inefficient to adjust them one by one. Therefore, guidelines are required for quickly adjusting the head loss coefficient to the specified value under working conditions. Here, we propose a rapid design strategy for the TLCD that is devised based on both prediction equations and variation trends in the head loss coefficient. This strategy is suitable for suppressing structures motions with low frequency and large amplitude.

In order to obtain the required head loss coefficient, every change rate of 0.1 for the opening ratio should be treated as a unit change in the head loss coefficient. Regardless of the value of other factors, the head loss coefficient will fall into the corresponding interval. Therefore, the requirement of the opening ratio should be ensured from the outset. Subsequently, according to the importance of each factor, the

Reynolds number or the horizontal length of liquid column could be adjusted. Because the influence of the total length of liquid column and Kc number is mainly due to their combined effect instead of the action of each alone, adjusting these two factors accurately is extremely difficult. If the head loss coefficient reaches the required value by adjusting the opening ratio, Reynolds number, and horizontal length of liquid column, the adjustment of the total length of liquid column and Kc number is not required.

5. Conclusions

A TLCD shows promise for applications to the motion suppression of floating platforms. In this study, a specific vibration test system on land was developed to satisfy the

requirements of offshore float platforms with low frequency and large amplitude. The damping characteristic of the TLCD governs the ability of vibration suppression. The influence of various factors on the head loss coefficient was investigated for motions of the main structure with low frequency and large amplitude. The following conclusions were drawn:

- (1) A vibration test system with large-amplitude motion simulation, low-frequency performance, and large stroke force (displacement) control was designed and built with simple operations and at low cost. This experimental system provided good waveforms for simple harmonic wave forces. The distortion within the low-frequency range of 0.5–1.5 Hz was less than 0.5%. The computed equivalent harmonic force showed good agreement with that obtained from experiment results with less than 5% error.
- (2) In published studies, the nonlinear damping term, but not the original term, has been analyzed with linearization. In this study, the nonlinear damping term and its head loss coefficient of the TLCD were calculated based on the energy transfer between the TLCD and the main structure. Experimental data on the table displacement, table velocity, table acceleration, equivalent harmonic force, and axis velocity of liquid column along the TLCD were used for calculations.
- (3) Based on the experimental method of uniform design, a reasonable and efficient experimental project was proposed to determine the variation trend in the head loss coefficient of the TLCD as a function of relevant parameters such as the total length of liquid column, opening ratio, Kc number, and Reynolds number. The prediction equation was obtained based on all the factors mentioned, whose reliability was verified from the results of random experimental tests.
- (4) Variation trends in the head loss coefficient as a function of the relevant parameters were obtained in accordance with the analysis of the prediction equation. For single-factor influences on the head loss coefficient, the opening ratio of the orifice dominated, whereas the Reynolds number and horizontal length of liquid column showed the next strongest impacts. Although the total length of liquid column and Kc number showed the weakest single-factor effects on the head loss coefficient, the combined effect of these two factors was apparent. In addition, the combined effect of the opening ratio and Kc number was also prominent.
- (5) A rapid design strategy for the TLCD head loss coefficient was proposed based on the changes in the head loss coefficient along with changes in TLCD-related parameters. This strategy proved highly convenient and effective for quickly adjusting the head loss coefficient to a specified value for effective vibration suppression.

Conflicts of Interest

The authors declare that they have no conflicts of interest.

Acknowledgments

The authors would like to express their gratitude for the financial support of the National Natural Science Foundation of China for Youth (Grant no. 5160916) and the State Key Laboratory Foundation of Shanghai Jiao Tong University (Grant no. 1502).

References

- [1] L.-L. Zhang, J. Li, and Y. Peng, “Dynamic response and reliability analysis of tall buildings subject to wind loading,” *Journal of Wind Engineering & Industrial Aerodynamics*, vol. 96, no. 1, pp. 25–40, 2008.
- [2] X.-H. Zeng, X.-W. Li, Y. Liu, and Y.-X. Wu, “Nonlinear dynamic responses of tension leg platform with slack-taut tether,” *China Ocean Engineering*, vol. 23, no. 1, pp. 37–48, 2009.
- [3] X.-H. Zeng, X.-P. Shen, and Y.-X. Wu, “Governing equations and numerical solutions of tension leg platform with finite amplitude motion,” *Applied Mathematics and Mechanics-English Edition*, vol. 28, no. 1, pp. 37–49, 2007.
- [4] F. Sakai, S. Takaeda, and T. Tamaki, “Tuned liquid column damper—new type device for suppression of building vibration,” in *Proceedings of International Conference on High-rise Buildings*, pp. 926–931, 1989.
- [5] M. J. Hochrainer, “Tuned liquid column damper for structural control,” *Acta Mechanica*, vol. 175, no. 1–4, pp. 57–76, 2005.
- [6] P. A. Hitchcock, K. C. S. Kwok, R. D. Watkins, and B. Samali, “Characteristics of liquid column vibration absorbers (LCVA) - I,” *Engineering Structures*, vol. 19, no. 2, pp. 126–134, 1997.
- [7] P. A. Hitchcock, K. C. S. Kwok, R. D. Watkins, and B. Samali, “Characteristics of liquid column vibration absorbers (LCVA) - I,II,” *Engineering Structures*, vol. 19, no. 2, pp. 135–144, 1997.
- [8] H. Gao, K. S. C. Kwok, and B. Samali, “Characteristics of multiple tuned liquid column dampers in suppressing structural vibration,” *Engineering Structures*, vol. 21, no. 4, pp. 316–331, 1999.
- [9] S.-K. Lee, E. C. Park, K.-W. Min, S.-H. Lee, and J.-H. Park, “Experimental implementation of a building structure with a tuned liquid column damper based on the real-time hybrid testing method,” *Journal of Mechanical Science and Technology*, vol. 21, no. 6, pp. 885–890, 2007.
- [10] S.-K. Lee, K.-W. Min, and H.-R. Lee, “Parameter identification of new bidirectional tuned liquid column and sloshing dampers,” *Journal of Sound and Vibration*, vol. 330, no. 7, pp. 1312–1327, 2011.
- [11] S.-K. Lee, H.-R. Lee, and K.-W. Min, “Experimental verification on nonlinear dynamic characteristic of a tuned liquid column damper subjected to various excitation amplitudes,” *The Structural Design of Tall and Special Buildings*, vol. 21, no. 5, pp. 374–388, 2012.
- [12] P. Chaiviriyawong, W. C. Webster, T. Pinkaew, and P. Lukkunaprasit, “Simulation of characteristics of tuned liquid column damper using a potential-flow method,” *Engineering Structures*, vol. 29, no. 1, pp. 132–144, 2007.

- [13] Y.-H. Chan and Y.-J. Ding, "Passive, semi-active, and active tuned-liquid-column dampers," *Structural Engineering and Mechanics*, vol. 30, no. 1, pp. 1–20, 2008.
- [14] K. A. Al-Saif, K. A. Aldakkan, and M. A. Foda, "Modified liquid column damper for vibration control of structures," *International Journal of Mechanical Sciences*, vol. 53, no. 7, pp. 505–512, 2011.
- [15] L. Huo and H. Li, "Torsionally coupled response control of offshore platform structures using CTLCD," in *Proceedings of the 15th International Offshore and Polar Engineering Conference, ISOPE-2005*, pp. 296–303, June 2005.
- [16] H. H. Lee, S.-H. Wong, and R.-S. Lee, "Response mitigation on the offshore floating platform system with tuned liquid column damper," *Ocean Engineering*, vol. 33, no. 8-9, pp. 1118–1142, 2006.
- [17] H. H. Lee and H. H. Juang, "Experimental study on the vibration mitigation of offshore tension leg platform system with UWTLCD," *Smart Structures and Systems*, vol. 9, no. 1, pp. 71–104, 2012.
- [18] Y.-H. Chen and C.-C. Chao, "Optimal damping ratio of TLCDs," *Structural Engineering and Mechanics*, vol. 9, no. 3, pp. 227–240, 2000.
- [19] K. M. Shum and Y. L. Xu, "Multiple-tuned liquid column dampers for torsional vibration control of structures: Experimental investigation," *Earthquake Engineering & Structural Dynamics*, vol. 31, no. 4, pp. 977–991, 2002.
- [20] K. M. Shum, "Closed form optimal solution of a tuned liquid column damper for suppressing harmonic vibration of structures," *Engineering Structures*, vol. 31, no. 1, pp. 84–92, 2009.
- [21] S. Chakraborty, R. Debbarma, and G. C. Marano, "Performance of tuned liquid column dampers considering maximum liquid motion in seismic vibration control of structures," *Journal of Sound and Vibration*, vol. 331, no. 7, pp. 1519–1531, 2012.
- [22] S. K. Yalla and A. Kareem, "Semiactive tuned liquid column dampers: Experimental study," *Journal of Structural Engineering*, vol. 129, no. 7, pp. 960–971, 2003.
- [23] J.-C. Wu, M.-H. Shih, Y.-Y. Lin, and Y.-C. Shen, "Design guidelines for tuned liquid column damper for structures responding to wind," *Engineering Structures*, vol. 27, no. 13, pp. 1893–1905, 2005.
- [24] J.-C. Wu, Y.-P. Wang, C.-L. Lee, P.-H. Liao, and Y.-H. Chen, "Wind-induced interaction of a non-uniform tuned liquid column damper and a structure in pitching motion," *Engineering Structures*, vol. 30, no. 12, pp. 3555–3565, 2008.
- [25] J.-C. Wu, C.-H. Chang, and Y.-Y. Lin, "Optimal designs for non-uniform tuned liquid column dampers in horizontal motion," *Journal of Sound and Vibration*, vol. 326, no. 1-2, pp. 104–122, 2009.
- [26] J.-C. Wu, Y.-P. Wang, and Y.-H. Chen, "Design tables and charts for uniform and non-uniform tuned liquid column dampers in harmonic pitching motion," *Smart Structures and Systems*, vol. 9, no. 2, pp. 165–188, 2012.
- [27] T. Sarpkaya, In-line and transverse forces on smooth and sand-roughened cylinders in oscillatory flow at high reynolds numbers. Naval Postgraduate School 1976.
- [28] T. Sarpkaya, "Vortex-induced oscillations," *Journal of Applied Mechanics*, vol. 46, no. 2, pp. 241–258, 1979.
- [29] T. Sarpkaya and M. Isaacson, *Mechanics of Wave Forces on Offshore Structures*. Van Nostrand Reinhold. New York 1981.
- [30] T. Sarpkaya, "Hydrodynamic damping, flow-induced oscillations, and biharmonic response," *Journal of Offshore Mechanics and Arctic Engineering*, vol. 117, no. 4, pp. 232–238, 1995.
- [31] J. Carberry, Wake states of a submerged oscillating cylinder and of a cylinder beneath a free-surface. Dissertation. Monash University 2002.
- [32] T. L. Morse and C. H. K. Williamson, "Employing controlled vibrations to predict fluid forces on a cylinder undergoing vortex-induced vibration," *Journal of Fluids and Structures*, vol. 22, no. 6-7, pp. 877–884, 2006.
- [33] J. X. Yu and M. Y. Fu, "Fatigue reliability analysis of vortex-induced vibration of submarine pipeline span," *Journal of Tianjin University*, vol. 41, no. 11, pp. 1321–1325, 2008.
- [34] J.-X. Yu, H.-L. Xu, C.-M. Yuan, and Z.-C. Wang, "Fatigue reliability analysis of vortex induced vibration of TLP tethers in waves and current," *Journal of Ship Mechanics*, vol. 12, no. 4, pp. 592–598, 2008.
- [35] J.-H. Kim, J.-H. Kim, S.-H. Jeong, and B.-W. Han, "Design and experiment of an electromagnetic vibration exciter for the rapping of an electrostatic precipitator," *Journal of Magnetics*, vol. 17, no. 1, pp. 61–67, 2012.
- [36] H. Li, B. Yang, G. Yan, and J. Hu, "Vibration control simulation of an electrodynamic shaker based on an electromagnetic finite element model," *International Journal of Applied Electromagnetics and Mechanics*, vol. 39, no. 1-4, pp. 769–777, 2012.
- [37] D. Zhu, S. Roberts, M. J. Tudor, and S. P. Beeby, "Design and experimental characterization of a tunable vibration-based electromagnetic micro-generator," *Sensors and Actuators A: Physical*, vol. 158, no. 2, pp. 284–293, 2010.
- [38] J. M. Oliver and S. Priya, "Design, fabrication, and modeling of a four-bar electromagnetic vibration power generator," *Journal of Intelligent Material Systems and Structures*, vol. 21, no. 13, pp. 1303–1316, 2010.
- [39] J. P. Conte and T. L. Trombetti, "Linear dynamic modeling of a uni-axial servo-hydraulic shaking table system," *Earthquake Engineering & Structural Dynamics*, vol. 29, no. 9, pp. 1375–1404, 2000.
- [40] M. Stehman and N. Nakata, "Direct acceleration feedback control of shake tables with force stabilization," *Journal of Earthquake Engineering*, vol. 17, no. 5, pp. 736–749, 2013.
- [41] Y. Jianjun, J. Guilin, D. Duotao, and L. Sheng, "Acceleration harmonic identification for an electro-hydraulic servo shaking table based on the normalized least-mean-square adaptive algorithm," *Journal of Vibration and Control*, vol. 19, no. 1, pp. 47–55, 2013.
- [42] Y. Dozono, T. Horiuchi, H. Katsumata, and T. Konno, "Shaking-table control by real-time compensation of the reaction force caused by a nonlinear specimen," *Journal of Pressure Vessel Technology, Transactions of the ASME*, vol. 126, no. 1, pp. 122–127, 2004.
- [43] B. Ye, G. Ye, W. Ye, and F. Zhang, "A pneumatic shaking table and its application to a liquefaction test on saturated sand," *Natural Hazards*, vol. 66, no. 2, pp. 375–388, 2013.
- [44] K.-T. Fang, D. K. Lin, P. Winker, and Y. Zhang, "Uniform design: theory and application," *Technometrics. A Journal of Statistics for the Physical, Chemical and En*, vol. 42, no. 3, pp. 237–248, 2000.
- [45] K.-T. Fang and F. J. Hickernell, "Uniform experimental design," in *Uniform Experimental Design, in Encyclopedia on Statistics in Quality and Reliability*, vol. 4, pp. 2037–2040, Wiley, 2008.

Research Article

Research on Fluid Viscous Damper Parameters of Cable-Stayed Bridge in Northwest China

Xiongjun He, Yongchao Yang, Xiang Xiao, and Yulin Deng

School of Transportation, Wuhan University of Technology, Wuhan, Hubei 430063, China

Correspondence should be addressed to Xiang Xiao; xxdocwhut@163.com

Received 16 June 2017; Accepted 22 August 2017; Published 28 September 2017

Academic Editor: Michele Palermo

Copyright © 2017 Xiongjun He et al. This is an open access article distributed under the Creative Commons Attribution License, which permits unrestricted use, distribution, and reproduction in any medium, provided the original work is properly cited.

To optimize the aseismic performance of nonlinear fluid viscous dampers (FVD) of cable-stayed bridge in the highly seismic zone, Xigu Yellow River Bridge in northwest China is taken as an example. Nonlinear time-history analysis method is used to research on the relation among the internal forces, displacements, and damping parameters of the 650 tonnage FVD. The method of getting the minimum of binary functions is used to obtain the optimal parameters of FVD. Also, the 1:1 full-scale FVD model is made and used in the constitutive relation test. Then the test result of the damping parameters can be got by normal equation method. The optimized method to obtain the damping parameters is further verified. The results indicate that seismic response in key positions of the cable-stayed bridge can be reduced by installing longitudinal nonlinear FVD between the towers and girders if choosing reasonable damping parameters C and ξ . The optimal damping parameters can be calculated accurately by the proposed method of optimizing damping parameters of nonlinear FVD, and the constitutive relation test verifies the correctness of the optimization analysis method. Conclusions concerned can be applied to the design of nonlinear FVD for cable-stayed bridges.

1. Introduction

For cable-stayed bridges, under longitudinal earthquake input, different tower-girder connection forms will have significant influence on the internal force response of main towers and its foundations, also on the displacements of girder end, and on the relative displacements of the girder and the approach bridge [1, 2]. The problem that the bridge tower internal force will be greatly increased in consolidated system and the problem that the longitudinal displacements of the girder end and the tower top will be enlarged in longitudinal floating system can be overcome by the damping system installed between the towers and girders [3, 4]. Therefore, increasing numbers of dampers are favored and used in aseismic system for cable-stayed bridges. However, the aseismic performances of the damper are mainly determined by the designed values of damping parameters C and ξ .

At present, there are few references about the parameter selection of fluid viscous dampers (FVD) in cable-stayed bridges. Researches have shown that choosing the reasonable damping parameters of FVD can reduce the seismic

response of key positions of cable-stayed bridges [5–7]. But the references about the selection of damping parameters mainly rely on subjective experience, which lacks experiment basis for selecting damping parameters [8, 9]. Therefore, the method, based on the constitutive relation test upon the FVD model, which is used to get the optimal value of the damping parameters of nonlinear FVD [10, 11], turns out to be useful for the design of FVD in cable-stayed bridges.

To improve the aseismic performance of the cable-stayed bridge, this paper presents a versatile procedure for the design of nonlinear FVD in cable-stayed bridges. Firstly, the relation among the internal forces, displacements, and damping parameters of the FVD under the action of earthquake is studied. The method of getting the minimum of binary functions is used to obtain the optimal parameters of FVD. Secondly, the results of the methodology adopted to obtain the optimized damping parameters have been confirmed by a constitutive relation test conducted on a full-scale model of the FVD. Seismic response in key positions of the cable-stayed bridge can be reduced by installing longitudinal nonlinear FVD if choosing reasonable damping parameters.



FIGURE 1: Xigu Yellow River Bridge.

2. Project Overview

Xigu Yellow River Bridge in northwest China, a key project in Lianhuo national trunk line of expressway, is a cable-stayed bridge with the longest span and the tallest tower over Yellow River in northwest China. As is shown in Figure 1, the main bridge is a cable-stayed bridge with double tower, double cable plane, and steel-concrete composite beam, of which the span is $(67 + 110 + 360 + 110 + 67)$ m. Four 650 tonnage dampers are installed between the towers and girders. Reinforced concrete rhombus tower is used and the south tower is 151 meters and the north tower is 147 meters. Steel I-beam and concrete composite girders are used in the main beam, and the composite girder is 2.83 meters high in the center of the steel girder and 3.06 meters in the center of the bridge. Low relaxed galvanized parallel steel tendon, with the 7 mm diameter and tensile strength not less than 1,770 MPa, is used in the stay cables and the longest cable is 187.068 meters weighing 17 tons. The seismic peak acceleration is 0.2 g and the predominant period of seismic response spectrum is 0.40 s in the bridge site, which is in eight-degree earthquake zone.

Based on the design and construction data, three-dimension element method is used to establish the finite element analytical model [12, 13] of Xigu Yellow River Bridge (Figure 2), in which the single girder mechanical model is utilized in the girder. Tension-only spatial truss element is used in stay cables and Ernst formula is utilized to rectify the elasticity modulus of the cables to verify the sagging effect [14, 15]. Spatial girder element is utilized to simulate the girders, the towers, and the piers. Damper element is used to simulate FVD [16, 17]. At the same time, the dead load effect on the structural stiffness is taken into consideration. The master-slave relation is used to simulate the girder joints, the lifting points of the stay cables, and the anchorage zone of the stay cables [18, 19]. The 6×6 coupled spring is adopted to simulate the mutual effect between the pile and soil in both pile foundations of the towers and the piers. The acceleration time-history curve with exceeding probability to be 10 percent in the future 50 years, which is provided from seismological bureau of Gansu Province, is taken as the earthquake load for Xigu Yellow River Bridge [20, 21].

3. Parameter Analysis of Nonlinear FVD

FVD consist of (Figure 3) cylinder, piston, hydraulic valve, piston rod, and silicone oil [22]. Under the earthquake load, the movement of the structure pushes the piston and the cylinder to produce relative displacement, and the reciprocating motion of the piston drives the flow of silicone oil. The friction between the molecules and that between the surface of the cylinder and the fluid generates heat so that the seismic energy can be converted into heat energy and the damping effect can be realized [23, 24]. FVD are common shock absorbers in bridge engineering, and the fundamental principle of damping property is [25–28]

$$F = CV^\xi, \quad (1)$$

where F is the damping force, C is the damping coefficient, V is the relative velocity of dampers, and ξ is the velocity index. In particular, when the velocity index is equal to 1, the damping force is proportional to the relative velocity and the damper turns out to be a linear one.

As can be seen from (1), the response of the damper to the structure is different because of the different damping parameters of FVD. However, most of researches mainly rely on subjective experience to select damping parameters and lack a unified method to select the parameters quantitatively [29–32]. Therefore, it is necessary to do sensitivity analysis of damping parameters C and ξ to discuss the variation of the structural response with the change of parameters, which is useful for the parameter design of the FVD.

In bridge engineering, the value of velocity index ξ is usually in the range of 0.2~2.0, and the damping coefficient C is usually in the range of 1000~20000 $\text{kN} \times (\text{s}/\text{m})^\xi$. Considering the FVD of Xigu Yellow River Bridge and the finite element analysis model, the damping coefficient C is set as 5000, 7500, 10000, 15000, and 20000 $\text{kN} \times (\text{s}/\text{m})^\xi$, respectively, and the velocity index ξ is set as 0.2, 0.3, 0.4, 0.5, 0.6, and 0.7, respectively. According to the trend of the calculation results of controlled internal force in the south tower bottom, it is easier to obtain the appropriate damping parameters when C is set as 2500, 5000, 7500, 10000, and 15000 $\text{kN} \times (\text{s}/\text{m})^\xi$, respectively. So there are a total of 30 conditions for parameter analysis.

3.1. Parameter Analysis of Controlled Internal Force. Because the cable-stayed bridge is a symmetrical structure, the south tower is taken as an example. The finite element model shown in Figure 2 is used to do parameter analysis in the 30 working conditions. The actions applied to the bridge include only earthquake acceleration at the bottom of each pier, which are provided from seismological bureau of Gansu Province of China and have 2% of exceeding probability of 50 years. Nonlinear time-history analysis method is used to research on the relation among the internal forces, displacements, and damping parameters.

As is shown in Figure 4, because of different damping coefficient C , the numerical values of longitudinal shear force in the tower bottom will change with velocity index ξ . And it is not hard to figure out that when the damping

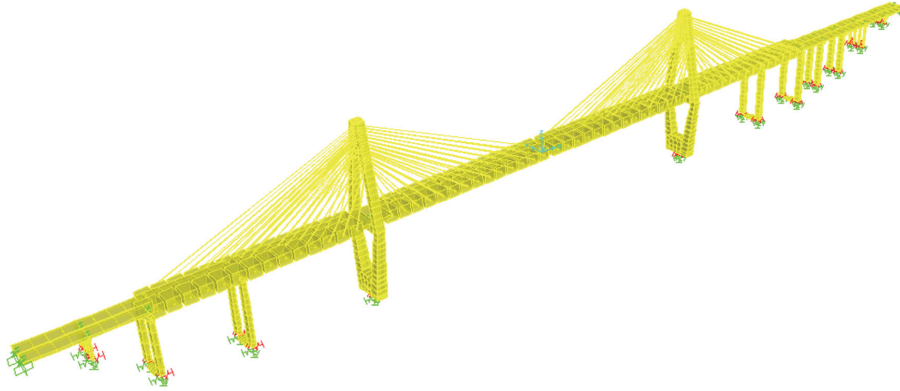


FIGURE 2: Finite element model of Xigu Yellow River Bridge.



FIGURE 3: The fluid viscous damper.

coefficient C is in the range of $5,000\sim 10,000 \text{ kN}\times(\text{s/m})^\xi$ and the velocity index ξ is in the range of $0.4\sim 0.7$, the seismic shear force in tower bottom is at a low level. Similarly, because of different damping coefficient C , the bending moment in tower bottom will change with velocity index ξ . And it is easy to find that when the damping coefficient C is in the range of $7,500\sim 10,000 \text{ kN}\times(\text{s/m})^\xi$ and the velocity index ξ is in the range of $0.4\sim 0.5$ or when damping coefficient C is equal to $15,000 \text{ kN}\times(\text{s/m})^\xi$ and velocity index ξ is equal to 0.7 , the bending moment in tower bottom is at a low level. Therefore, from the perspective of reducing the seismic response in tower bottom, the optimal effect can be achieved when damping coefficient C is in the range of $7,500\sim 10,000 \text{ kN}\times(\text{s/m})^\xi$ and velocity index ξ is in the range of $0.4\sim 0.5$.

As is shown in Figure 5, for the foundation shear force, when damping coefficient C is less than $10,000 \text{ kN}\times(\text{s/m})^\xi$, the foundation shear force response decreases with ξ decreasing, and when damping coefficient C is greater than $10,000$, the foundation shear force response decreases first and then increases with ξ increasing. As for foundation bending moment, with the increase of C and the decrease of ξ , the foundation bending moment response gets smaller and smaller. Therefore, from the perspective of reducing the internal force in tower bottom foundation, the optimal effect can be achieved when damping coefficient C is in the range of $7,500\sim 15,000 \text{ kN}\times(\text{s/m})^\xi$ and damping constant ξ is in the range of $0.3\sim 0.5$.

3.2. Parameter Analysis of Controlled Displacement. As is shown in Figure 6(a), the girder end displacements decrease with the increase of damping coefficient C . When damping coefficient C is greater than $10,000$, the influence of C on the girder end displacement is weakened, and the increase of ξ has little influence on the girder end displacements. Therefore, from the perspective of reducing the girder end displacements, the optimal effect can be reached when damping coefficient C is in the range of $10,000\sim 20,000 \text{ kN}\times(\text{s/m})^\xi$ and velocity index ξ is in the range of $0.3\sim 0.5$.

As is shown in Figure 6(b), when damping coefficient C is less than $10,000 \text{ kN}\times(\text{s/m})^\xi$, the relative displacements between the south main bridge and the approach bridge increase with ξ increasing, but when damping coefficient C is greater than $10,000 \text{ kN}\times(\text{s/m})^\xi$, the relative displacements decrease first and then increase with ξ increasing. However, from the perspective of reducing the displacements, the optimal effect can be achieved when damping coefficient C is in the range of $10,000\sim 20,000 \text{ kN}\times(\text{s/m})^\xi$ and velocity index ξ is in the range of $0.3\sim 0.5$.

Based on the above analysis, the seismic response in the tower bottom, the tower foundation, and the girder can be reduced effectively by installing longitudinal nonlinear FVD between the towers and girders when the velocity index ξ is in the range of $0.4\sim 0.5$ and the damping coefficient C is about $10,000 \text{ kN}\times(\text{s/m})^\xi$.

3.3. Optimization of Damping Parameters. As is shown in Sections 3.1 and 3.2, the damping parameters of the FVD can be preliminarily determined qualitatively by simulating and analyzing the finite element model in multiple conditions. However, when determining the optimal damping parameter in many researches [33–36], the results of multiple situations are simply put to take the common intersection. This method lacks quantitative analysis of multiple conditions. It is obvious that the internal forces or displacements of key positions are binary function of damping parameters C and ξ . Thus, least square method can be used to perform the surface fitting of the relation among the internal forces or the displacements of key positions with damping parameters C and ξ . And then the problem is transformed to solve the extreme values of

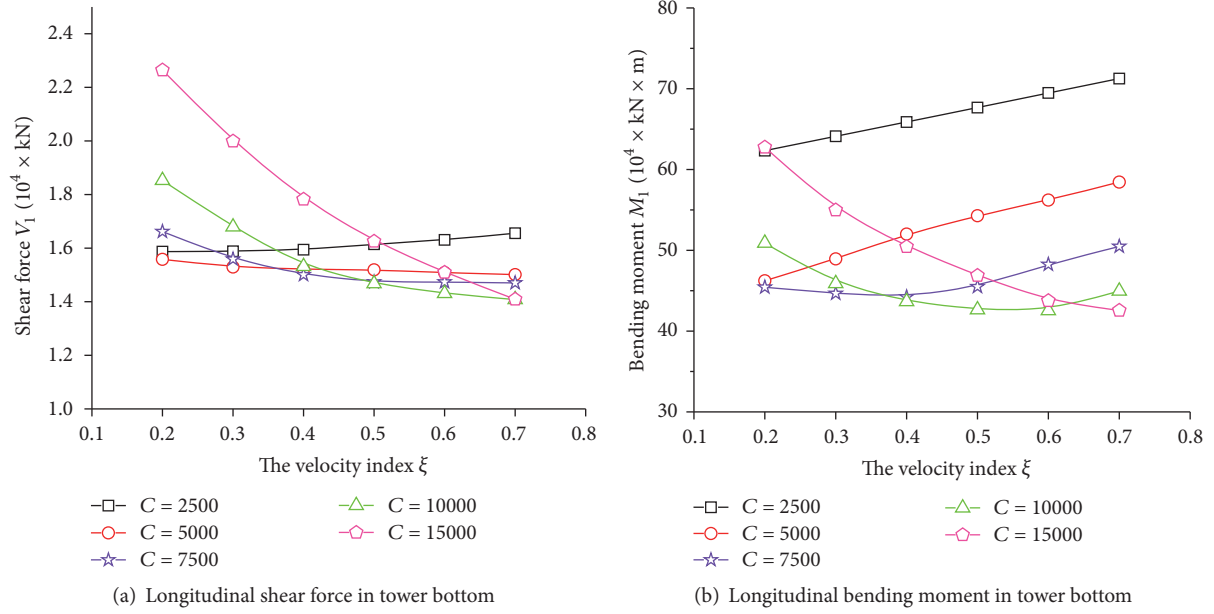


FIGURE 4: Change of controlled internal force in the south tower bottom with damping parameters.

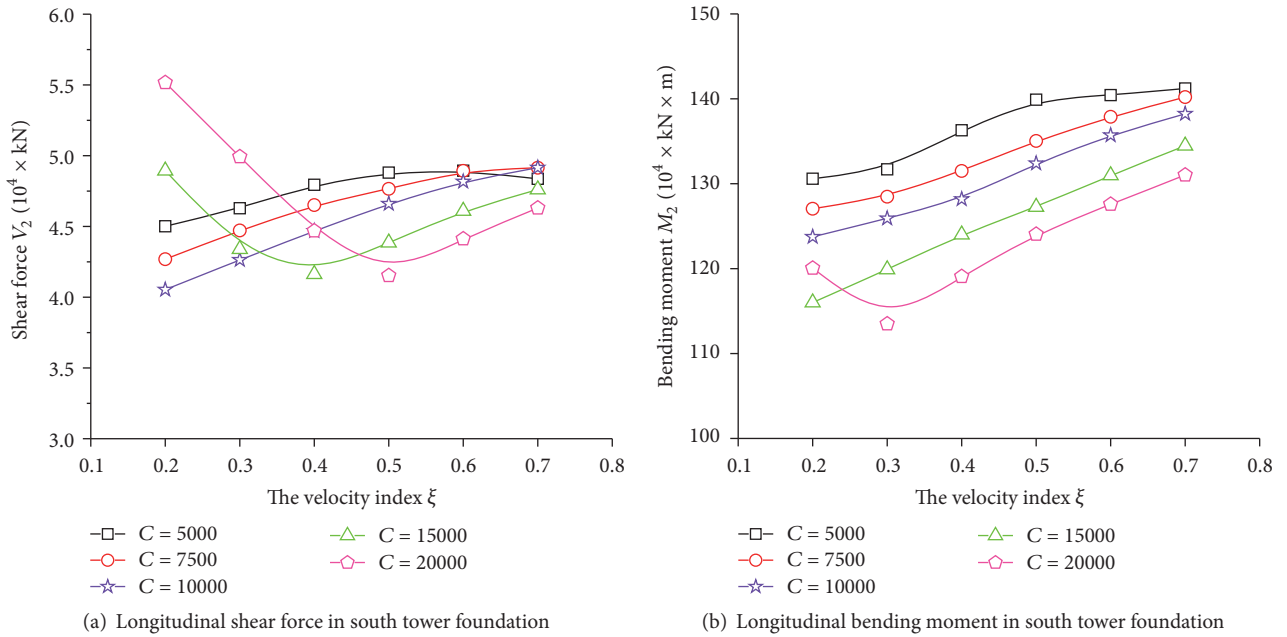


FIGURE 5: Change of controlled internal force in the south tower foundation with damping parameters.

the nonlinear binary function. The least squares fitting is realized by the LSQCURVEFIT command in MATLAB, and the surface fitting results are as Table 1.

The coefficient of determination r^2 is

$$r^2 = \frac{\sum_{i=1}^n (\hat{y}_i - \bar{y})^2}{\sum_{i=1}^n (y_i - \bar{y})^2}, \quad (2)$$

where n is the sample number, \hat{y}_i is the corresponding value of regression equation, \bar{y} is the sample average, and y_i is the sample corresponding value. The coefficient of determination

r^2 reflects the goodness of fitting, and its range is $[0, 1]$. The closer the r^2 is to 1, the better the regression equation is fitted.

To obtain the optimal damping parameters, the results of surface fitting in Table 1 are arranged:

$$V = V_1 + V_2,$$

$$M = M_1 + M_2, \quad (3)$$

$$D = D_1 + D_2.$$

TABLE 1: Parametric regression analysis.

Surface fitting results	Coefficient of determination r^2
Shear force in south tower bottom: $V_1 = (18205 - 0.697C + 80010\xi + 1.373 \times 10^{-4}C + 15187\xi^2 - 7.886C \cdot \xi)/(1 + 5.199\xi - 3.245 \times 10^{-4}C \cdot \xi)$	0.995
Bending moment in south tower bottom: $M_1 = (896827 - 154.105C + 3155531\xi + 1.376 \times 10^{-2}C^2 + 1061168\xi^2 - 239.911C \cdot \xi)/(1 + 4.339\xi)$	0.991
Shear force in south tower foundation: $V_2 = (44375 - 3.07C - 268759\xi - 6.29 \times 10^{-5}C^2 - 25432\xi^2 + 19.88C \cdot \xi)/(1 - 8.06 \times 10^{-5}C - 5.75\xi + 3.87 \times 10^{-4}C \cdot \xi)$	0.962
Bending moment in south tower foundation: $M_2 = 1345037 - 18.064C + 216122\xi + 7.956C \cdot \xi$	0.951
Displacement in girder south end: $D_1 = (0.18 - 2.19 \times 10^{-5}C - 0.19\xi + 1.88 \times 10^{-10}C^2 + 0.36\xi^2 + 5.05 \times 10^{-5}C \cdot \xi)/(1 - 1.27 \times 10^{-4}C - 1.38\xi + 4.25 \times 10^{-4}C \cdot \xi)$	0.991
Relative displacement between the main bridge and the approach bridge: $D_2 = 0.239 - 1.448 \times 10^{-5}C + 0.161\xi + 1.014 \times 10^{-9}C^2 + 0.193\xi^2 - 2.70 \times 10^{-5}C \cdot \xi$	0.956

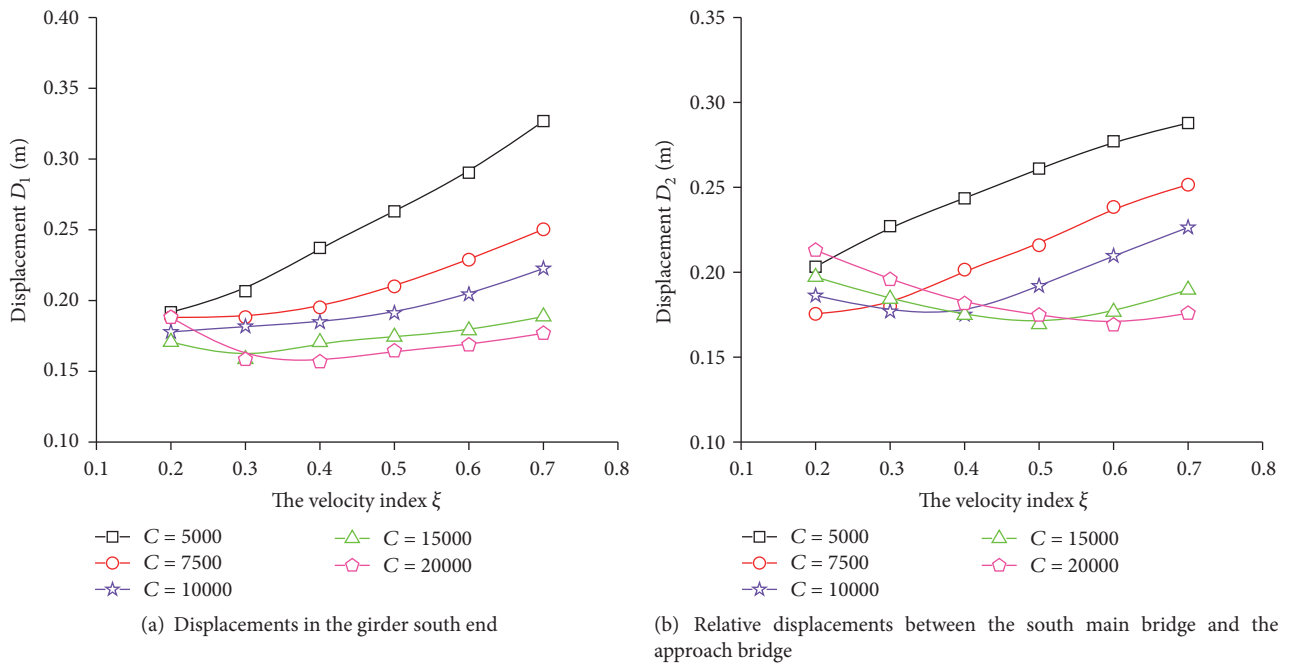


FIGURE 6: Change of controlled displacements with damping parameters.

The constraint condition is as follows: $C \in [2000, 20000]$ and $\xi \in [0.2, 0.7]$. The damping parameters C and ξ can be got as long as the minimal values of (2) with constraint condition are solved. Take the average value of the three sets of damping parameters as the optimal damping parameters: $C = 10871 \text{ kN} \times (\text{s/m})^\xi$ and $\xi = 0.415$. The above-mentioned method can be applied to obtain the optimal damping parameters when to design the nonlinear FVD in bridges.

4. Model Making and Experiment

To further verify the optimization method of damping parameters in Section 3.3, in laboratory for training and research in earthquake engineering and seismology at EUCENTRE (Pavia, Italy), the damper tester showed in Figure 7 is applied to do the constitutive relation test on the 1:1 full-scale damper model of Xigu Yellow River Bridge in

TABLE 2: Main parameters of the FVD model.

Maximum damping force	Length of FVD model	Maximum displacement	Maximum velocity
6500 kN	3457 mm	± 400 mm	340.6 mm/s

Lanzhou. The installation for testing is shown in Figure 8, and the main parameters of the damper model are shown in Table 2.

Make the damper tester control the piston rod to move at the speed of 3 mm/s, 30 mm/s, 60 mm/s, and 80 mm/s successively so that the constitutive relation test can be conducted. Then the relation between the damping force and the relative movement velocity of the piston pod can be tested. Conduct 3 complete axial displacement cyclic loadings in each set. Namely, the displacement is controlled from 0 to the



FIGURE 7: The damper tester.



FIGURE 8: Installation for testing.

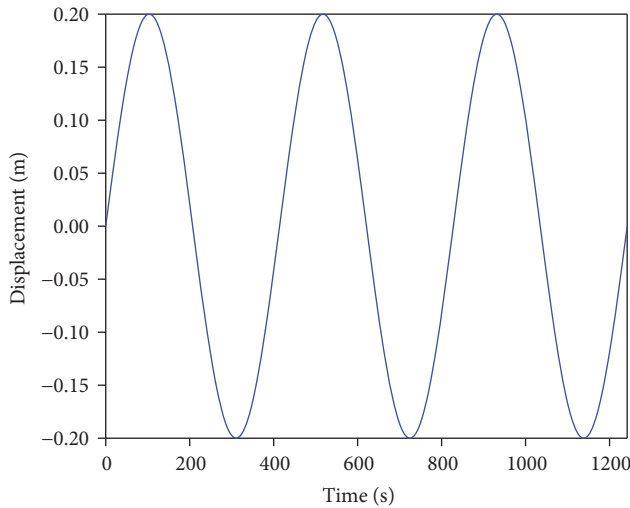


FIGURE 9: Displacement time-history curve of the damper piston pod.

half of the positive maximum range and then to the half of the negative maximum range, and back to 0 at last. In the first set of test, the relative displacement of the controlled piston pod is shown in Figure 9, and the time-history curve of the FVD relative velocity is shown in Figure 10, and the time-history curve of the damping force is shown in Figure 11.

As is shown from the test results in Figures 10 and 11, when the relative displacement of the damper piston pod is

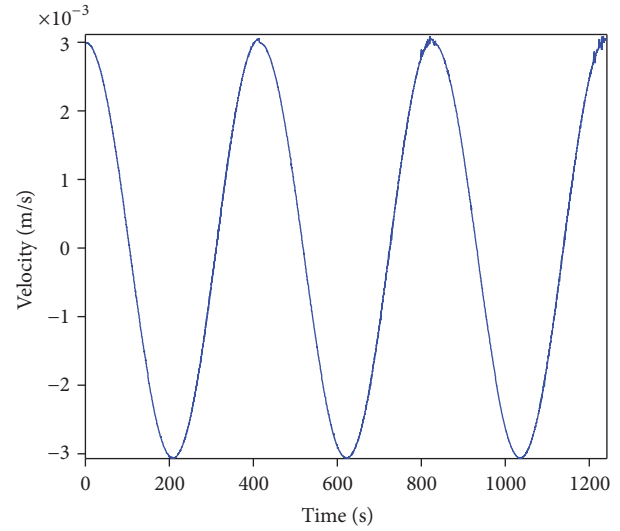


FIGURE 10: Velocity time-history curve of the damper piston pod.

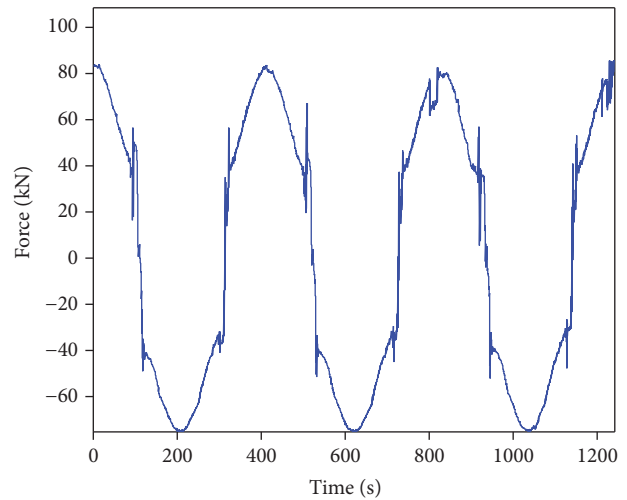


FIGURE 11: Time-history curve of the damping force.

a sine curve, the time-history curve of the velocity and the time-history curve of the damping force can be seen as cosine curve approximately. And the damping force changes greatly when the velocity of the damper is close to 0.

The damping forces of the FVD in four sets tests with the relative velocities are shown in Figure 12. Obviously, the test value curve of the damping force is consistent with the theoretical value curve. Applying a logarithmic law at each member of (1), the following expression is obtained:

$$\log F = \log C + \xi \log V. \quad (4)$$

When the damping force F and velocity V are already known, (4) represents a linear problem in the parameters

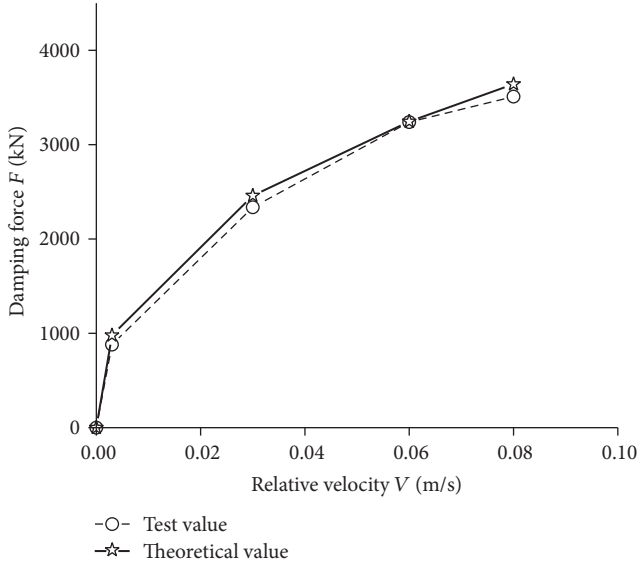


FIGURE 12: Damping force changes with the velocity.

$\log C$ and ξ . To solve the least squares problem, the normal equations method can be used.

$$\begin{bmatrix} \log F_1 \\ \log F_2 \\ \vdots \\ \log F_n \end{bmatrix} = \begin{bmatrix} 1 & \log V_1 \\ 1 & \log V_2 \\ \vdots & \vdots \\ 1 & \log V_n \end{bmatrix} \cdot \begin{bmatrix} \log C \\ \xi \end{bmatrix} \Rightarrow \quad (5)$$

$$\vec{F} = \vec{V} \cdot \begin{bmatrix} \log C \\ \xi \end{bmatrix}.$$

So the value of $\log C$ and ξ can be calculated with

$$\begin{bmatrix} \log C \\ \xi \end{bmatrix} = \left[\vec{V}^T \cdot \vec{V} \right]^{-1} \cdot \vec{V}^T \cdot \vec{F}. \quad (6)$$

Substituting the damping forces and velocities tested in the four sets of tests into (6), the damping parameters $C = 10496 \text{ kN} \times (\text{s/m})^\xi$ and $\xi = 0.427$ can be got. The damping parameters of the test are consistent with that of the optimal method, which further verifies the method of optimizing damping parameters.

5. Conclusion

Taking Xigu Yellow River Bridge in Lanzhou where the seismic intensity is eight degrees as an example, the method of combining finite element simulation and the 1:1 full-scale FVD model test is adopted to discuss the reasonable FVD parameters of a cable-stayed bridge in highly seismic zone. The following conclusions can be reached:

(1) The FVD are longitudinally installed between the towers and girders in cable-stayed bridge, whose damping parameters have great significance on the seismic response.

After the simulation analysis in 30 conditions by using the finite element software, the reasonable damping parameters can be preliminarily determined. For the nonlinear FVD of Xigu Yellow River Bridge, the seismic response in the tower bottom, tower foundation, and the girder can be effectively reduced when the velocity index ξ is in the range of 0.4~0.5 and the damping coefficient C is about $10000 \text{ kN} \times (\text{s/m})^\xi$.

(2) When nonlinear FVD are used in the design of bridges, least square method can be applied to conduct the surface fitting on the relation among the internal forces, displacements, and damping parameters C and ξ . So the problem is transformed to solve the extreme values of the nonlinear constraint binary function. The optimal values of damping parameters can be got explicitly by the method, which is useful for the design of nonlinear FVD installed in cable-stayed bridges.

(3) Through the constitutive relation test in the 1:1 full-scale FVD model of Xigu Yellow River Bridge in Lanzhou, the results show that when the relative displacement of the damper piston pod is a sine curve, the time-history curve of the velocity and the time-history curve of the damping force can be seen as cosine curve approximately. And the damping force changes greatly when the velocity of the damper is close to 0.

(4) Through the comparison between the finite element simulation analysis and the full-scale FVD model test, the test value curve of the damping force keeps consistent with the theoretical value curve. The damping parameters $C = 10496 \text{ kN} \times (\text{s/m})^\xi$ and $\xi = 0.427$ are got, which agrees with the result of the finite element analysis. The method of optimizing damping parameters is further verified.

Conflicts of Interest

The authors declare that there are no conflicts of interest regarding the publication of this paper.

Acknowledgments

Thanks are due to the Laboratory for Training and Research in Earthquake Engineering and Seismology at EUCENTRE (Pavia, Italy) for assistance with the experiments. The authors would like to express appreciation for the financial support by Project of Science and Technology Research Program of Department of Transport, Gansu Province (GJJS [2016] no. 74).

References

- [1] R. L. Teixeira, F. P. L. Neto, and J. F. Ribeiro, "Modelling and experimental investigation of an active damper," *Shock and Vibration*, vol. 13, no. 4-5, pp. 343-354, 2006.
- [2] Z. Guan, H. You, and J.-Z. Li, "Lateral isolation system of a long-span cable-stayed bridge with heavyweight concrete girder in a high seismic region," *Journal of Bridge Engineering*, vol. 22, no. 1, Article ID 04016104, 2017.
- [3] M. H. Alhamaydeh, S. A. Barakat, and F. H. Abed, "Multiple regression modeling of natural rubber seismic-isolation systems with supplemental viscous damping for near-field ground

- motion," *Journal of Civil Engineering and Management*, vol. 19, no. 5, pp. 665–682, 2013.
- [4] P. P. Diotallevi, L. Landi, and A. Dellavalle, "A methodology for the direct assessment of the damping ratio of structures equipped with nonlinear viscous dampers," *Journal of Earthquake Engineering*, vol. 16, no. 3, pp. 350–373, 2012.
 - [5] G. P. Colato, S. Infanti, and M. G. Castellano, "Special fluid viscous dampers for the messina strait bridge," in *Proceedings of the 2008 Seismic Engineering International Conference Commemorating the 1908 Messina and Reggio Calabria Earthquake, MERCEA 2008*, pp. 1374–1380, ita, July 2008.
 - [6] M. C. Constantinou and M. D. Symans, *Experimental and analytical investigation of seismic response of structures with supplemental fluid viscous dampers*, National Center for earthquake engineering research, Buffalo, NY, USA, 1992.
 - [7] L. Liu, X. Zhang, and Q. Yang, "Estimation of the optimum parameters of fluid viscous dampers for seismic response control of highway bridges," in *Proceedings of the 29th Chinese Control Conference, CCC'10*, pp. 5705–5711, chn, July 2010.
 - [8] N. Gluck, A. M. Reinhorn, J. Gluck, and R. Levy, "Design of supplemental dampers for control of structures," *Journal of Structural Engineering*, vol. 122, no. 12, pp. 1394–1399, 1996.
 - [9] R. Greco and G. C. Marano, "Identification of parameters of Maxwell and Kelvin-Voigt generalized models for fluid viscous dampers," *Journal of Vibration and Control*, vol. 21, no. 2, pp. 260–274, 2015.
 - [10] X. He, W. Chen, and B. Zhu, "Theoretical analysis on the damping characteristics of a clearance type viscous damper," *Advanced Science Letters*, vol. 15, no. 1, pp. 422–424, 2012.
 - [11] K. Ikago, K. Saito, and N. Inoue, "Seismic control of single-degree-of-freedom structure using tuned viscous mass damper," *Earthquake Engineering & Structural Dynamics*, vol. 41, no. 3, pp. 453–474, 2012.
 - [12] N. Makris, M. C. Constantinou, and G. F. Dargush, "Analytical model of viscoelastic fluid dampers," *Journal of Structural Engineering*, vol. 119, no. 11, pp. 3310–3325, 1993.
 - [13] T. T. Soong and G. F. Dargush, *Passive Energy Dissipation Systems in Structural Engineering*, John Wiley & Sons, Chichester, UK, 1997.
 - [14] Q. Wu, J. Dai, and H. Zhu, "Optimum design of passive control devices for reducing the seismic response of twin-tower-connected structures," *Journal of Earthquake Engineering*, pp. 1–35, 2017.
 - [15] G.-H. Zhao and Y.-M. Zhang, "Parametric sensitivity study on fluid viscous damper of long span suspension bridge," *Advanced Materials Research*, vol. 255–260, pp. 998–1002, 2011.
 - [16] T. J. Sullivan and A. Lago, "Towards a simplified Direct DBD procedure for the seismic design of moment resisting frames with viscous dampers," *Engineering Structures*, vol. 35, pp. 140–148, 2012.
 - [17] T. S. Vader and C. C. McDaniel, "Influence of dampers on seismic response of cable-supported bridge towers," *Journal of Bridge Engineering*, vol. 12, no. 3, pp. 373–379, 2007.
 - [18] L. Landi, P. P. Diotallevi, and G. Castellari, "On the design of viscous dampers for the rehabilitation of plan-asymmetric buildings," *Journal of Earthquake Engineering*, vol. 17, no. 8, pp. 1141–1161, 2013.
 - [19] B. B. Soneji and R. S. Jangid, "Influence of soil-structure interaction on the response of seismically isolated cable-stayed bridge," *Soil Dynamics and Earthquake Engineering*, vol. 28, no. 4, pp. 245–257, 2008.
 - [20] S. Silvestri and T. Trombetti, "Physical and numerical approaches for the optimal insertion of seismic viscous dampers in shear-type structures," *Journal of Earthquake Engineering*, vol. 11, no. 5, pp. 787–828, 2007.
 - [21] M. S. A. Khan, A. Suresh, and N. S. Ramaiah, "Numerical study of magnetic circuit response in magneto-rheological damper," *Journal of Engineering, Design and Technology*, vol. 14, no. 1, pp. 196–210, 2016.
 - [22] P. P. Diotallevi, L. Landi, and S. Lucchi, "Seismic retrofit of existing buildings with viscous dampers: a direct procedure for the determination of the required supplemental damping," in *Proceedings of the 7th International Structural Engineering and Construction Conference: New Developments in Structural Engineering and Construction, ISEC 2013*, pp. 1761–1766, Honolulu, Hawaii, USA, June 2013.
 - [23] J. J. Aguirre, J. L. Almazán, and C. J. Paul, "Optimal control of linear and nonlinear asymmetric structures by means of passive energy dampers," *Earthquake Engineering and Structural Dynamics*, vol. 42, no. 3, pp. 377–395, 2013.
 - [24] J. Jia and H. Hua, "Test verification of a design method for a fluid viscous damper," *Advanced Materials Research*, vol. 291–294, pp. 2085–2088, 2011.
 - [25] M. D. Martínez-Rodrigo, J. Lavado, and P. Museros, "Dynamic performance of existing high-speed railway bridges under resonant conditions retrofitted with fluid viscous dampers," *Engineering Structures*, vol. 32, no. 3, pp. 808–828, 2010.
 - [26] S. Silvestri, G. Gasparini, and T. Trombetti, "A five-step procedure for the dimensioning of viscous dampers to be inserted in building structures," *Journal of Earthquake Engineering*, vol. 14, no. 3, pp. 417–447, 2010.
 - [27] D. Konstantinidis, J. M. Kelly, and N. Makris, *In-Situ Monitoring of The Force Output of Fluid Dampers: Experimental Investigation*, Pacific Earthquake Engineering Research Center, 2011.
 - [28] L. Landi, P. P. Diotallevi, and G. Castellari, "Design of viscous dampers for the seismic retrofit of plan-asymmetric structures," in *The Seventh International Structural Engineering and Construction Conference (ISEC-7)*, pp. 18–23, Honolulu, Hawaii, USA, 2013.
 - [29] L. Landi and P. P. Diotallevi, "Design procedure for the seismic retrofit of existing RC buildings with viscous dampers: a case study," in *World Congress on Advances in Structural Engineering and Mechanics (ASEM+)*, pp. 3673–3690, Seoul, Korea, 2011.
 - [30] D. I. Narkhede and R. Sinha, "Behavior of nonlinear fluid viscous dampers for control of shock vibrations," *Journal of Sound and Vibration*, vol. 333, no. 1, pp. 80–98, 2014.
 - [31] F. Sadek, B. Mohraz, and M. A. Riley, "Linear procedures for structures with velocity-dependent dampers," *Journal of structural engineering New York, N.Y.*, vol. 126, no. 8, pp. 887–895, 2000.
 - [32] C. J. Black and N. Makris, "Viscous heating of fluid dampers under small and large amplitude motions: experimental studies and parametric modeling," *Journal of Engineering Mechanics*, vol. 133, no. 5, pp. 566–577, 2007.
 - [33] J. Zhu, W. Zhang, K. F. Zheng, and H. G. Li, "Seismic design of a long-span cable-stayed bridge with fluid viscous dampers," *Practice Periodical on Structural Design and Construction*, vol. 21, no. 1, Article ID 04015006, 2016.
 - [34] Z. Fnag, F. Wang, Z. Zhang, C. Wang, and W. Ding, "Effects of viscous damper parameters on anti-seismic performance of long-span bridge," *Journal of Highway and Transportation Research and Development*, vol. 26, no. 2, pp. 73–78, 2009.

- [35] W.-P. Deng, H. Wang, A.-Q. Li, and J.-S. Liu, "Parametric analysis of viscous dampers for earthquake mitigation of continuous bridges in high intensity region," *Zhendong yu Chongji/Journal of Vibration and Shock*, vol. 31, no. 16, pp. 92–97, 2012.
- [36] C. P. Providakis, "Effect of LRB isolators and supplemental viscous dampers on seismic isolated buildings under near-fault excitations," *Engineering Structures*, vol. 30, no. 5, pp. 1187–1198, 2008.